STABILITY AND TRANSIENT EFFECTS IN ULTRAVIOLET FILAMENTS

by

Thomas Andrew Niday

A Dissertation Submitted to the Faculty of the

COMMITTEE ON OPTICAL SCIENCES (GRADUATE)

In Partial Fulfillment of the Requirements
For the Degree of

DOCTOR OF PHILOSOPHY

In the Graduate College

THE UNIVERSITY OF ARIZONA

2 0 0 4

		Form Approved
Report Documentation Page		OMB No. 0704-0188

Public reporting burden for the collection of information is estimated to average 1 hour per response, including the time for reviewing instructions, searching existing data sources, gathering and maintaining the data needed, and completing and reviewing the collection of information. Send comments regarding this burden estimate or any other aspect of this collection of information, including suggestions for reducing this burden, to Washington Headquarters Services, Directorate for Information Operations and Reports, 1215 Jefferson Davis Highway, Suite 1204, Arlington VA 22202-4302. Respondents should be aware that notwithstanding any other provision of law, no person shall be subject to a penalty for failing to comply with a collection of information if it does not display a currently valid OMB control number.

1. REPORT DATE **01 SEP 2004**	2. REPORT TYPE **N/A**	3. DATES COVERED **-**

4. TITLE AND SUBTITLE	5a. CONTRACT NUMBER
Stability And Transient Effects In Ultraviolet Filaments	5b. GRANT NUMBER
	5c. PROGRAM ELEMENT NUMBER
6. AUTHOR(S)	5d. PROJECT NUMBER
	5e. TASK NUMBER
	5f. WORK UNIT NUMBER
7. PERFORMING ORGANIZATION NAME(S) AND ADDRESS(ES) **University Of Arizona**	8. PERFORMING ORGANIZATION REPORT NUMBER
9. SPONSORING/MONITORING AGENCY NAME(S) AND ADDRESS(ES)	10. SPONSOR/MONITOR'S ACRONYM(S)
	11. SPONSOR/MONITOR'S REPORT NUMBER(S)

12. DISTRIBUTION/AVAILABILITY STATEMENT
Approved for public release, distribution unlimited

13. SUPPLEMENTARY NOTES
The original document contains color images.

14. ABSTRACT

15. SUBJECT TERMS

16. SECURITY CLASSIFICATION OF:			17. LIMITATION OF ABSTRACT	18. NUMBER OF PAGES	19a. NAME OF RESPONSIBLE PERSON
a. REPORT **unclassified**	b. ABSTRACT **unclassified**	c. THIS PAGE **unclassified**	**UU**	**134**	

Standard Form 298 (Rev. 8-98)
Prescribed by ANSI Std Z39-18

PLACEHOLDER FOR APPROVAL PAGE

STATEMENT BY AUTHOR

This dissertation has been submitted in partial fulfillment of requirements for an advanced degree at The University of Arizona and is deposited in the University Library to be made available to borrowers under rules of the Library.

Brief quotations from this dissertation are allowable without special permission, provided that accurate acknowledgment of source is made. Requests for permission for extended quotation from or reproduction of this manuscript in whole or in part may be granted by the head of the major department or the Dean of the Graduate College when in his or her judgment the proposed use of the material is in the interests of scholarship. In all other instances, however, permission must be obtained from the author.

SIGNED: _____

ACKNOWLEDGMENTS

TABLE OF CONTENTS

TABLE OF CONTENTS - Continued

LIST OF FIGURES

LIST OF TABLES

ABSTRACT

Short, high intensity laser pulses induce nonlinear optical effects in the atmosphere that have the potential to make them propagate for long distances. Applications for long distance propagation of short pulses include active spectral remote sensing and laser lightning control. Much of the work in this field has been done with infrared pulses; however, it has been proposed that ultraviolet pulses have the advantage that longer pulse lengths can be used, thereby delivering more energy. Long pulse lengths lead to a simplified instantaneous model for the plasma response, which has been shown by Schwarz and Diels to admit steady state or oscillatory solutions corresponding to beam propagation. We have verified this model and have adjusted it to achieve closer agreement with numerical results.

In this work we investigate the effects of transient behavior, and the stability of these solutions. Analysis of the modulational instability is done from the plane wave level to a full three dimensional model of the propagation. It is shown that both the transient behavior arising from the finite pulse length, and the modulational instability cause pulses to fragment over lengths on the scale of meters. We present results showing the growth of unstable modes in various propagation regimes. We discuss the pertinent length scales for ultraviolet pulses, as well as the impact of the instability and transient effects on theory and experiment. The results imply that continuous-wave models are very limited when used to predict dynamical properties of pulse propagation.

CHAPTER 1

INTRODUCTION

1.1 Motivation

The study of short light pulses in the atmosphere is motivated by the variety of nonlinear processes that affect short pulses. Low intensity, spatially wide laser beams diffract, and are adversely affected by scattering and atmospheric turbulence. However, short pulses that are intense enough to induce several nonlinear optical effects in the air may be able to propagate for long distances, by changing the optical properties of the air.

The primary nonlinear effect is self-focusing, which is caused by the intensity dependent refractive index induced by the optical Kerr effect [1]. If the peak power exceeds a certain critical power, this self-focusing overcomes diffraction and causes the beam to focus tighter as it propagates, which in turn intensifies the nonlinear effects. At some point, the field becomes strong enough to ionize the molecules in the air, and higher order effects such as multi-photon absorption, plasma absorption, and plasma defocusing stop the collapse [2, 3]. The propagation of a light pulse depends on the interaction between self-focusing and the various collapse arrest mechanisms. If there is a stable balance between these effects, the beam may become self-trapped and form a filament [2, 4]. If the balance is unstable, the pulse may split into multiple filaments in both space and time [5].

Tightly focused light filaments have the potential to pass through atmospheric tur-

bulence and scattering media such as clouds [6] with less distortion than a continuous-wave (CW) beam encounters. This opens up applications in remote sensing. As an ultrashort pulse compresses temporally, it can generate a broad spectrum, or "white light supercontinuum" [7, 8, 9]. This might be used in future Lidar (LIght Detection And Ranging) remote sensing techniques for spectral analysis of pollutants or malicious compounds in the atmosphere [10, 11]. The plasma channels generated by light filaments may also have the ability to enable laser induced lightning [12, 13]. With the development of high peak power pulsed lasers, experiments are now being done with atmospheric propagation of ultrashort pulses [6, 9, 11, 14]. Propagation distances as long as 2 km vertical in the atmosphere [14] and 200 m horizontal in air [15] have been claimed; however, questions remain as to what conditions are optimal for long distance propagation.

1.2   Ultraviolet Filaments

Much of the theoretical and experimental work on filaments has been done in the infrared, typically with wavelengths near 800 nm and pulse lengths on the order of hundreds of fs. However, some researchers are investigating the possibility of creating self-trapped pulses in the ultraviolet wavelength region, near 248 nm. UV filaments have been studied and contrasted with those in the IR [3]. In the ultraviolet, the critical power for self-focusing in air is smaller than the critical power in the infrared. It has been proposed that one may be able to scale the length of a propagating filament up in time, to longer pulses on the order of hundreds of picoseconds to

nanoseconds, instead of ultrashort pulses on the order of femtoseconds [16, 17]. This was proposed because it was observed that the balance of self-focusing and plasma defocusing appears to depend only on the intensity of the field [16]. Additionally, the reduced contribution from avalanche ionization in the ultraviolet extends the upper limit on the pulse duration up to tens of nanoseconds, four orders of magnitude larger than in the infrared [17]. Scaling up to longer pulses could increase the amount of energy delivered.

This has been investigated by Schwarz and Diels, who have developed an analytical approximation to the problem of propagating longer pulses in the UV [17]. The term "long pulse" depends on reference scale. For UV pulses, a long pulse is one that is approximated by a beam that is independent of time, because the scale of the pulse, on the order of nanoseconds, is much longer than the time scale of the nonlinear response of the air. In their semi-analytical approach, a Gaussian ansatz for the spatial beam profile converts the partial differential equation for beam propagation into an ordinary differential equation for the evolution of the beam waist size. Their steady state approximation forces the nonlinear response due to the plasma to act as an effective $\chi^{(4)}$ nonlinearity. This approximation should be valid for pulses that are long enough for the generated plasma density to reach a steady state value. Their model predicts trapped solutions which oscillate in width, depending on the initial conditions.

In Chapter 3, we numerically verify the Schwarz-Diels semi-analytical results, by using a split-step Fourier method of beam propagation. We have also been able to adjust some of their approximations, to make the model predictions quantitatively

agree better with numerical simulations. We then obtain idealized steady state CW beam solutions to the nonlinear propagation equation. However, this model, which contains no time dependence, cannot represent transient effects, such as how the beam solution is created in time, or whether the beam solution is stable.

1.3   Experimental Status

Many experiments have been done to study infrared filaments, often near 800 nm, and using short pulse lengths [6, 8, 9, 14, 15, 18-25]. Experiments range from laboratory studies of filament formation in various media to atmospheric propagation tests. One project of note is the Teramobile, which is a mobile terawatt-femtosecond class laser operated by a joint French-German team [11, 14]. This laser generates 5 TW peak power pulses with 70 fs duration at 790 nm. It fits in a cargo container, and is being used to demonstrate atmospheric Lidar applications.

Fewer experiments have been done to demonstrate UV filaments. The pulse lengths involved in current UV experiments, while typically longer than those considered ultrashort in the IR, are shorter than those that will be discussed in this dissertation. For example, Schwarz et al. have performed experiments using a frequency tripled Ti:Sapphire laser to obtain filaments at 248 nm. They created pulse widths between 600 fs and several ps, and observed filaments that propagated for 12 m, much longer than the Rayleigh range of 12.5 cm for their pulses [16, 26].

Tzortzakis et al. performed experiments for both 450 fs and 5 ps pulses. They have observed ultraviolet filaments at 248 nm that propagate stably for 4 m. They noted

that their filaments are more stable than corresponding filaments in the infrared [4].

An unanswered question is what experiments will tell us about longer ultraviolet pulses, such as lengths from hundreds of picoseconds to nanoseconds. It has been proposed that the results for ultraviolet filaments should scale with respect to increasing the pulse length [16, 26], resulting in long distance propagation of long duration UV filaments. However, experimental evidence for this is not yet available. The examination of the theory for longer UV filaments, on the order of hundreds of ps, will occupy much of the following chapters.

1.4   Filament Stability

The semi-analytical solution for long pulses, developed by Schwarz and Diels, can be related to variational methods that have been developed for nonlinear optical propagation. These variational methods have been used [27, 28, 29] to provide analytical or semi-analytical solutions to difficult problems, while retaining physical insight into the nature of the solutions. They are often used in conjunction with a model in which the temporal response of the plasma is assumed to be instantaneous. This is accomplished by either using a long pulse approximation [17], or, for shorter pulses, by examining the integrated contribution of the plasma at an arbitrary central time slice of the pulse [15, 30, 31]. However, we will see that the problem of temporal stability is critically important, and may be overlooked by using such approximations. We will investigate the behavior of the UV filament solutions by moving beyond the steady state model.

To investigate this question of stability, we develop a linear perturbation analysis that allows numerical simulation of oscillatory perturbations to a proposed zeroth order solution. We also use a three dimensional numerical code that includes the time domain and two transverse spatial dimensions. By first using periodic boundary conditions for the time domain, we isolate the fundamental instability from effects caused by the edges of the pulse. The results indicate that these pulses do suffer from a modulational instability. In Chapters 4 and 6, further analysis and simulation results detail the nature of the instability: its growth rate, frequency structure, and spatial form.

We will also consider the relationship between the pulse length and the length scales of the various effects. Schwarz and Diels established that the pulse length must satisfy certain conditions in order to use their long pulse approximation [17]. If a pulse is too short, the steady state plasma approximation becomes invalid [17]. If a pulse is too long, avalanche ionization begins to become important and must be added to the plasma model [17]. Since the growth rate of the instability depends on the frequency of the perturbation, in general the pulse length can play a role in stability. If a pulse is long enough to contain the strongest unstable periodic variations, it will be most strongly affected. In Chapter 7, we examine these length scales, and the experimental and theoretical implications of this instability and other effects for long ultraviolet pulses in air. We will also briefly examine the impact of stimulated Raman scattering [1], as it can produce instabilities, based on the time delayed nonlinear response [32, 33].

CHAPTER 2

REVIEW OF THEORY

2.1   Propagation Equation

This section briefly reviews the equations for propagation of a light field under the relevant nonlinear effects and approximations of interest. This will also help establish notational conventions and units. We will use MKS units throughout, unless stated otherwise. Start with the Maxwell wave equation in a nonmagnetic material with no free currents or charges [1]:

$$\nabla \times \nabla \times \mathbf{E} + \frac{1}{c^2}\frac{\partial^2 \mathbf{E}}{\partial t^2} = -\frac{1}{\epsilon_0 c^2}\frac{\partial^2 \mathbf{P}}{\partial t^2}. \tag{2.1.1}$$

Assuming that $\nabla \cdot \mathbf{E} = 0$, use the relation $\nabla \times \nabla \times \mathbf{E} = \nabla(\nabla \cdot \mathbf{E}) - \nabla^2 \mathbf{E}$ to obtain

$$\nabla^2 E - \frac{1}{c^2}\frac{\partial^2 E}{\partial t^2} = \frac{1}{\epsilon_0 c^2}\frac{\partial^2 P}{\partial t^2}, \tag{2.1.2}$$

assuming a scalar field E and scalar polarization P. This reduces to

$$\nabla^2 E - \frac{n_0^2}{c^2}\frac{\partial^2 E}{\partial t^2} = \frac{1}{\epsilon_0 c^2}\frac{\partial^2 P^{NL}}{\partial t^2}, \tag{2.1.3}$$

where n_0 is the background linear index of refraction, if the material is assumed to be isotropic. In the quasi-monochromatic approximation, the real electric field E for

a wave propagating along the z-axis is then represented by a complex amplitude $\mathcal{E}$:

$$E(x, y, z, t) = \frac{1}{2} \, \mathcal{E}(x, y, z, t) e^{i(kz-\omega t)} + c.c. \tag{2.1.4}$$

Note that the exponential term is sometimes defined with the opposite sign, as in Schwarz and Diels [17]. With this particular complex representation, in the SI system of units, the field intensity is

$$I = \frac{n_0}{2} \left(\frac{\epsilon_0}{\mu_0}\right)^{1/2} |\mathcal{E}|^2 = \frac{n_0 \epsilon_0 c}{2} |\mathcal{E}|^2, \tag{2.1.5}$$

where n_0 is the linear refractive index, $\epsilon_0 = 8.85 \times 10^{-12}$ F/m is the permittivity of free space, $\mu_0 = 4\pi \times 10^{-7}$ H/m is the permeability of free space [1], and $c^2 = (\epsilon_0 \mu_0)^{-1}$. Some authors omit the factor of 1/2 from Equation (2.1.4). This alternate convention changes Equation (2.1.5) by a factor of four.

Since we use scalar fields, we treat the nonlinear susceptibilities as scalars. A complete treatment for the general case of tensor susceptibilities and how they contribute to the nonlinear refractive indices can be found in the literature [1, 34]. The nonlinear polarization may be expressed as

$$P^{NL} = f(|\mathcal{E}|^2)E = \epsilon_0 \Delta \chi E. \tag{2.1.6}$$

If the nonlinear response is instantaneous, $\Delta \chi$ will be a simple function of $|\mathcal{E}|^2$. The quantity $\Delta \chi$ may depend on time through the plasma density, which gives it a memory based on the previous field history, which makes it non-instantaneous. The self-

focusing term $\chi^{(3)}$ (or n_2) will also be non-instantaneous if the Raman effect is considered; for now, let it be instantaneous. In this case, the simple nonlinear polarization term P^{NL} for self-focusing can be written as

$$P^{NL} = \epsilon_0 \chi^{(3)} |\mathcal{E}|^2 E. \qquad (2.1.7)$$

The full nonlinear polarization will contain terms from self-focusing, plasma defocusing and absorption, and multi-photon ionization losses.

Following Schwarz and Diels [17], insert Equation (2.1.4) for the electric field into the wave equation in Equation (2.1.3), to obtain

$$\left(\nabla_\perp^2 + \frac{\partial^2}{\partial z^2} - \frac{n_0^2}{c^2} \frac{\partial^2}{\partial t^2} \right) \mathcal{E} e^{i(kz - \omega t)} = \frac{1}{c^2} \frac{\partial^2}{\partial t^2} \left[\Delta\chi \mathcal{E} e^{i(kz - \omega t)} \right], \qquad (2.1.8)$$

where $\nabla_\perp^2$ is the transverse Laplacian. Next perform the z and t derivatives above. Assume that $\mathcal{E}(x, y, z, t)$ and $\Delta\chi(x, y, z, t)$ are slowly varying in z and t compared to $\exp[i(kz - \omega t)]$; neglect the second derivatives in z and t. This gives

$$\left[\nabla_\perp^2 \mathcal{E} + 2ik \left(\frac{\partial \mathcal{E}}{\partial z} + \frac{n_0}{c} \frac{\partial \mathcal{E}}{\partial t} \right) + \left(\frac{\omega^2 n_0^2}{c^2} - k^2 \right) \mathcal{E} \right] e^{i(kz - \omega t)} =$$
$$\frac{1}{c^2} \left[-2i\omega \frac{\partial(\Delta\chi\mathcal{E})}{\partial t} - \omega^2 \Delta\chi\mathcal{E} \right] e^{i(kz - \omega t)}. \qquad (2.1.9)$$

Here we have used $k = n_0\omega/c$ and are neglecting any dispersion effects, such as group velocity dispersion (GVD). This allows cancellation of the last term in brackets in the above equation, and we group the $\partial\mathcal{E}/\partial z$ and $\partial\mathcal{E}/\partial t$ terms together. GVD and other

correction terms, which account for chromatic dispersion, are introduced through a series expansion [35] in studies of ultrashort pulses. However, we will either study the case of CW beams, in which there is no time dependence, or long pulses on the order of hundreds of picoseconds, for which neglecting dispersion is a very appropriate approximation due to their small spectral width. We will also neglect the $\partial(\Delta\chi\mathcal{E})/\partial t$ term on the right hand side. This correction to the nonlinear response is small for fields that are slowly varying compared to the optical frequency. Cancelling the exponential dependence gives

$$\nabla_\perp^2 \mathcal{E} + 2ik\left(\frac{\partial\mathcal{E}}{\partial z} + \frac{n_0}{c}\frac{\partial\mathcal{E}}{\partial t}\right) = -\frac{\omega^2}{c^2}\Delta\chi\mathcal{E}. \tag{2.1.10}$$

For a CW beam, the time derivative of the field envelope is zero. However, if the field envelope is a pulse, we can use the transformation $t' = t - (n_0/c)z$, keeping the same z, to eliminate the time derivative. In both cases, rearranging terms gives

$$\frac{\partial\mathcal{E}}{\partial z} = \frac{i}{2k}\nabla_\perp^2 \mathcal{E} + \frac{ik}{2n_0^2}\Delta\chi\mathcal{E}. \tag{2.1.11}$$

For simple self-focusing, $\Delta\chi = \chi^{(3)}|\mathcal{E}|^2$. Using the relationship $\chi^{(3)} = 2n_0 n_2$ [17], this gives the self-focusing nonlinear Schrödinger equation

$$\frac{\partial\mathcal{E}}{\partial z} = \frac{i}{2k}\nabla_\perp^2 \mathcal{E} + ik_0 n_2|\mathcal{E}|^2\mathcal{E}, \tag{2.1.12}$$

where n_2 is the self-focusing index. Here $\chi^{(3)}$, n_2, and $|\mathcal{E}|^2$ can all be in intensity or amplitude units, as long as one is consistent; see Appendix A for details.

If the nonlinear polarization includes the effect of the generated plasma, the propagation equation that we use is [16]

$$\frac{\partial \mathcal{E}}{\partial z} = \frac{i}{2k}\nabla_\perp^2 \mathcal{E} + ik_0 n_2 |\mathcal{E}|^2 \mathcal{E} - \frac{\beta^{(K)}}{2}|\mathcal{E}|^{2K-2}\mathcal{E} - \frac{\sigma}{2}(1+i\omega\tau)\rho\mathcal{E}. \qquad (2.1.13)$$

Here, the third term on the right hand side is a loss term corresponding to multiphoton ionization (MPI) generation, where $\beta^{(K)}$ is the coefficient for MPI at order K. The plasma term is derived from the Drude model [36]. In this term, σ is the cross section for inverse bremsstrahlung, ω is the optical reference frequency of the light, τ is the characteristic electron collision time, and ρ is the electron plasma density.

Note: In the paper by Schwarz and Diels [17], to which we often refer, there are some minor errors in units, discussed in Appendix A, that do not affect their conclusions, but can cause confusion when comparing results. For simplicity, we use intensity units for all quantities such as $\mathcal{E}$, $\chi^{(3)}$, and n_2. Thus $n_2 I$ or $n_2|\mathcal{E}|^2$ is the unitless quantity representing the refractive index change induced by the optical Kerr effect.

2.2   Self-Focusing and Other Nonlinear Effects

Some of the earliest work on self-focusing was motivated by the observation of thin damage streaks in materials in which an intense laser beam had been focused [37]. The diameter of these damage tracks was smaller, by up to two orders of magnitude, than the corresponding diameter of a linearly focused Gaussian beam; the length of the tracks extended over several centimeters, indicating the presence of an intense

filament in which the light is tightly guided over many Rayleigh ranges [37, 38].

The self-focusing is accounted for by the n_2 term in the polarization, which describes the optical Kerr effect [38]. This term is an intensity-dependent refractive index [1]. If n_2 is positive, a sufficiently strong field generates a region of higher index of refraction in the center of the beam, which acts as a focusing lens. The focusing further intensifies the field, which in turn increases the self-focusing effect [39]. For most of this dissertation, the n_2 term will be assumed to describe an instantaneous response; in Section 7.4, we will discuss how including the Raman effect introduces a memory into this response, and the implications of this for filaments.

When a beam contains more power than a certain critical power, it will undergo self-focusing collapse. As the beam intensifies, it begins to ionize the molecules in the air through multi-photon ionization (MPI). Collapse will continue until some physical effect, such as defocusing or losses from the plasma, acts to stop the collapse. The critical power for self-focusing of a Gaussian beam with wavelength λ is

$$P_{cr} \approx \frac{\lambda^2}{2\pi n_0 n_2}, \tag{2.2.1}$$

where n_0 is the background index and n_2 is in intensity units [27, 40]. In the ultraviolet at $\lambda = 248$ nm, n_2 is 7.8×10^{-23} m^2/W, and the critical power in air is approximately 125 MW. In the near-infrared, the critical power is somewhat larger, due to smaller n_2 and larger λ. At 775 nm, for example, the critical power in air is 1.7 GW [40]. For pure self-focusing of a beam, the behavior only depends on the power in the beam, not its size or intensity. Beams with multiple critical powers present can break up

into multiple filaments due to modulational instability [5, 34, 2, 41].

Other relevant nonlinear effects appear as higher order terms, such as $n_3|\mathcal{E}|^3$, $n_4|\mathcal{E}|^4$, ..., which can act as defocusing terms if their sign is negative. However, terms that are odd in the electric field, such as the n_3 term, only generally have nonzero coefficients in non-centrosymmetric media [1, page 41].

Intense light pulses generate plasma through multi-photon ionization of the molecules in the air. This adds a nonlinear loss for the electric field. The plasma also induces nonlinear effects; this nonlinear response from the plasma, in Equation (2.1.13), includes both a plasma defocusing term and a plasma absorption term [17, 36]. For the special case of the long UV pulses discussed by Schwarz and Diels [17], the plasma defocusing was shown to act as an effective n_3 term, even though air does not have an n_3 response. They also assume that the plasma response is instantaneous, compared to the time scales of long pulses.

The balance between self-focusing, diffraction, and the other nonlinear effects has been the subject of many theoretical studies. One debate was whether the observation of light filaments, which are extended in space, was due to the creation of an effective waveguide (self-guiding) or a the self-focusing of the various parts of a pulse (moving focus model). In the self-guiding model, a pulse is assumed to propagate stably under the influence of a wave guide created by the balance between the ionized plasma and the Kerr effect [20, 42]. The moving focus model applies to finite duration pulses: it assumes that different time slices of a pulse will contain different peak powers, and thus focus at different distances, explaining the observation of an extended filament [24, 43]. In a third approach, the propagation of a short pulse

is described by a dynamic spatial replenishment model, where the pulse undergoes multiple collapses in time as it decays and is replenished by a new pulse [5, 40, 2].

When we consider long ultraviolet filaments, we will first assume that they can be treated as sections of CW beams, and apply the long pulse model that will be described in Section 2.4. In this context self-guiding is the applicable model.

More detailed discussions on the theory of self-focusing can be found in Boyd [1] and Marburger [34]. Another, recent review of self-focusing in the context of wave collapse is provided by Bergé [44].

2.3   Variational Techniques

The equations for nonlinear beam or pulse propagation must in general be solved numerically, even when the approximations in Section 2.1 are made. An alternative approach is to use a variational method. One first casts the propagation equation in a Lagrangian form, and makes an ansatz for the form of a solution to the propagation equation. Then the Rayleigh-Ritz method or Kantorovich method [44, 45, 46], is used to determine the evolution of the parameters present in the ansatz. If the ansatz captures the physics of the solution well, it provides a simplified analytical or semi-analytical approach to solving a complicated problem.

For example, Anderson and Bonnedal developed a variational treatment for nonlinear self-focusing of Gaussian beams with a general nonlinear refractive index [28]. Their treatment includes a discussion of non-steady propagation, such as the oscillatory solutions that Schwarz and Diels find. Wright et al. used their method to

study propagation of a CW beam in a medium with a cubic-quintic nonlinearity [27].

Anderson and Bonnedal start with the equation

$$2ik\frac{\partial \mathcal{E}}{\partial z} + \nabla_\perp^2 \mathcal{E} + Q(|\mathcal{E}|^2)\mathcal{E} = 0, \tag{2.3.1}$$

where Q represents a general nonlinearity. They present variational results for three

forms of Q, the most applicable here being the series

$$Q(|\mathcal{E}|^2) = \sum_{n=1}^{\infty} C_{2n}|\mathcal{E}|^{2n}. \tag{2.3.2}$$

By using the trial function

$$\mathcal{E}(r, z) = \mathcal{E}_0(z)\exp[-r^2/2a^2(z) + ir^2 b(z)], \tag{2.3.3}$$

they obtain the variational result for the functional evolution of the beam radius [28]:

$$\frac{d^2 a}{dz^2} = \frac{1}{k^2 a^3}\left[1 - H(a^2)\right], \tag{2.3.4}$$

where for the above form of Q,

$$H(a^2) = \sum_{n=1}^{\infty} \frac{nC_{2n}}{(n+1)^2}\frac{(|\mathcal{E}_0|a_0)^{2n}}{a^{2n-2}}. \tag{2.3.5}$$

In this fashion, the partial differential equation for the evolution of the field $\mathcal{E}$ is

reduced to an ordinary differential equation for the evolution of the variational pa-

rameter a. We will use their result later in Section 3.2, and compare it with the results

of Schwarz and Diels [17]. Their method is not formally presented as a variational approach, but its results are nearly equivalent to other Gaussian beam variational approaches [27, 28, 29].

We show in Section 3.2 that using the variational method for UV filaments indicates that the characteristics of the balance depend on the peak intensity, which agrees with existing treatments [16, 17]. With just n_2 self-focusing present, the focusing characteristics depend only on the power, for a Gaussian beam [34]. However, when the balance between n_2 and n_3 is analyzed, we find that the peak intensity of the beam is a more suitable indicator of its characteristics. For trapped solutions, the peak intensity, once chosen, determines the width and thus the peak power of the steady state solution, as well as its stability characteristics. This intensity dependence motivated the proposition that scaling to higher pulse energies and longer pulses in the UV might be possible [16, 17].

Other authors have applied variational methods to pulse propagation, with increasing levels of detail. Aközbek et al. have studied femtosecond pulse propagation using a variational method similar to that discussed above [29]. They include the nonlinear loss terms through a dissipative modification of the standard variational treatment [45, 47].

2.4   Long Pulse Model

In the long pulse model, or near steady state approximation, used by Schwarz and Diels, the action of the plasma on the light field is reduced to a simple instantaneous

nonlinearity. During the middle section of the pulse, the time dependence of the plasma is removed, by assuming it has had enough time to reach a steady state value. This will be a good approximation if the plasma generation rise time is much shorter than the time scales of the pulses of interest. The plasma term in the propagation equation is then replaced by an effective nonlinear index term. In the case of UV filaments at 248 nm, the plasma acts as an effective n_3 term. The advantage of such a model is that if it is accurate, one no longer needs to consider the time dimension when doing a simulation, which becomes difficult for long pulses.

However, as applied to the UV problem, the long pulse model also places an upper limit on the length of the pulse. The upper limit is set by inverse bremsstrahlung, which causes avalanche ionization, and in the Schwarz-Diels analysis comes out to 4-60 ns. The lower limit, as mentioned, is set by the time it takes for the plasma to build up to its steady state value, and is is roughly 30-200 ps [17, 26]. These limits depend on the strength of the multi-photon absorption rate, which is a value that is known with very poor accuracy, within only two or three orders of magnitude. As the MPI rate decreases, the upper limit decreases and the lower limit increases, narrowing the width of the region of pulse lengths that satisfy the model.

Schwarz and Diels derive their semi-analytical solution for propagation of pulses with lengths that satisfy these limits. In the introduction to their paper, however, they mention that their results do not address the stability of the solution nor the transient evolution to steady state [17]. In the following chapters, these issues will be shown to present a critical weakness of using a long pulse model for UV filaments.

CHAPTER 3

STEADY STATE SOLUTIONS

3.1 Application of the Long Pulse Model

In this chapter, we review and extend the method of Schwarz and Diels [17], and cite their primary results to provide a foundation for the investigation into the stability and transient effects. Start with the following equation for propagation [16] of the electric field envelope $\mathcal{E}(x, y, z, t)$:

$$\frac{\partial \mathcal{E}}{\partial z} = \frac{i}{2k}\nabla_\perp^2 \mathcal{E} + ik_0 n_2 |\mathcal{E}|^2 \mathcal{E} - \frac{\beta^{(K)}}{2}|\mathcal{E}|^{2K-2}\mathcal{E} - \frac{\sigma}{2}(1 + i\omega\tau)\rho\mathcal{E}. \tag{3.1.1}$$

The electron density ρ of the plasma is described by

$$\frac{\partial \rho}{\partial t} = C\rho|\mathcal{E}|^2 + \frac{\beta^{(K)}|\mathcal{E}|^{2K}}{K\hbar\omega} - \alpha\rho^2 + D\nabla_\perp^2\rho, \tag{3.1.2}$$

where C is a coefficient for avalanche ionization, α is an electron-positive ion recombination coefficient [17], and D is a diffusion strength. In steady state, the left hand side of Equation (3.1.2) is zero. If there is no diffusion ($D = 0$), the steady state plasma density is the solution of a quadratic equation at each point in space.

Note that Schwarz and Diels [17] use a different form for the multi-photon ionization source term in their equation for the plasma. Their MPI source term is $\sigma^{(3)}I^3 N_0$, where $\sigma^{(3)}$ is the three-photon MPI cross section, I is the intensity, and N_0 is the

density of oxygen in the air. Using the values in Table 3.1, note that

$$\frac{\beta^{(3)}}{3\hbar\omega} = \sigma^{(3)} N_0 \equiv b = 1.6 \times 10^{-16} \; \frac{\text{m}^3}{\text{W}^3 \; \text{s}} \; . \tag{3.1.3}$$

This consistency is achieved by using the values in Ref. [17] for $\sigma^{(3)}$ and N_0 to derive the value of $\beta^{(3)}$, rather than using the value from Ref. [16]. We will use the shorthand notation that b represents the overall MPI coefficient for the plasma.

In the model used by Schwarz and Diels, the steady state ansatz allows one to express the plasma density ρ as a power of the field strength or intensity. This is only true for certain pulse lengths [17]. First, if the pulses are short enough, less than tens of nanoseconds, the avalanche term in Equation (3.1.2) can be neglected. If the pulses are long enough so that the plasma has time to reach steady state, they set $\partial\rho/\partial t = 0$. This rise time is on the order of 30-200 ps, depending on the publication [17, 26]. They also neglect the diffusion term. Thus, solving for ρ,

$$\rho = \sqrt{b/\alpha}|\mathcal{E}|^K, \tag{3.1.4}$$

where $b \equiv \beta^{(K)}/K\hbar\omega$. Given the light frequency of interest, which tells us the MPI order K, under this approximation the plasma density is proportional to $|\mathcal{E}|^K$. Thus the plasma response term can be replaced by an effective $n_K|\mathcal{E}|^K\mathcal{E}$ nonlinear index term. For UV pulses at 248 nm, $K = 3$, and $\rho \propto |\mathcal{E}|^3$, so Schwarz and Diels replace

the plasma term by an effective n_3 term. They derive the value of this term as

$$n_3 = -\sqrt{\frac{\sigma^{(3)} N_0}{\alpha}} \frac{e^2}{2n_0 \omega^2 m_e \epsilon_0}, \tag{3.1.5}$$

where e and m_e are the charge and mass of the electron, using a model for the electron plasma [17]. To reach the simplest case, neglect losses in the propagation equation, and consider them later once the solution is understood. Equation (3.1.1) reduces to

$$\frac{\partial \mathcal{E}}{\partial z} = \frac{i}{2k} \nabla_\perp^2 \mathcal{E} + ik_0 n_2 |\mathcal{E}|^2 \mathcal{E} + ik_0 n_3 |\mathcal{E}|^3 \mathcal{E}. \tag{3.1.6}$$

Note that the plasma defocusing coefficient $\sigma \omega \tau \rho / 2$ from Equation (3.1.1) is equal to $k_0 n_3 |\mathcal{E}|^3$, given the steady state dependence of ρ on $|\mathcal{E}|^3$, for the parameters in Table 3.1.

Schwarz and Diels use a semi-analytical approach with a Gaussian beam ansatz to convert this equation to one for an imaginary particle representing the beam width, moving on a potential surface. Their result is an ordinary differential equation that can be solved with a straightforward integration. If the particle is trapped in a potential well, the beam will oscillate in width as it propagates. They illustrate these oscillatory solutions in their paper [17]; the size of the oscillations depends on how steep or shallow the well in the effective potential is.

There is a question as to how the beam width oscillations are to be interpreted. Schwarz and Diels suggest [17] that they correspond to a steady state analog of the dynamic replenishment phenomenon [40]. However, this model explains the propagation of short pulses in air by time-dependent interactions between the leading and

Table 3.1: Parameters used in propagation

Parameter	Name	Value	Units
Background index	n_0	1	—
Self focusing index	n_2	7.8×10^{-23}	m^2/W
Plasma nonlinear index	n_3	-3.3×10^{-31}	$\mathrm{m}^3/\mathrm{W}^{3/2}$
MPI order	K	3	—
Wavelength	λ	248	nm
MPI coefficient	$\beta^{(3)}$	3.9×10^{-34}	$\mathrm{m}^3/\mathrm{W}^2$
Recombination loss	α	1.1×10^{-12}	m^3/s
Inverse bremsstrahlung cross section	σ	5.2×10^{-25}	m^2
Electron collision time	τ	3.5×10^{-13}	s
Density of oxygen	N_0	5.4×10^{24}	m^{-3}
3-photon absorption cross section	$\sigma^{(3)}$	3×10^{-41}	$\mathrm{m}^6\mathrm{s}^2/\mathrm{J}^3$
Linear absorption loss	α_L	2.5×10^{-4}	m^{-1}

trailing edges of the pulse and the generated plasma; the pulse splits in time, and power from the trailing edge replenishes the pulse. The oscillations that we consider are for a time independent beam that can be characterized by a single width as a function of time. Additionally, any spatial pulse shaping, such as ring formation, cannot be described by the Gaussian beam ansatz.

The parameters that we use in simulations are presented in Table 3.1. Many of these are from Schwarz and Diels [17], so that we can compare and verify the results. Additional parameters are taken from Ref. [16]. Some of the values in the table are not well known, in particular the MPI coefficient which determines the MPI rate. This MPI coefficient is difficult to measure [48], and may change by two orders of magnitude up or down, depending on the publication [16, 17, 26, 48]. The numbers from Schwarz and Diels [17], are values that will allow comparison to previous work, as well as give physically interesting insights into the application of the steady state

model. The following sections discuss details of the oscillatory solutions, and how the approximation in the Schwarz-Diels approach can be modified to give better agreement with numerical simulation.

3.2 Improving the Aberrationless Approximation

In Schwarz and Diels [17], the electric field amplitude $\mathcal{E}(r, z)$ is assumed to be a Gaussian. Then, they make the following parabolic "aberrationless" approximation for powers of the electric field [17, Equation 30],

$$|\mathcal{E}(z,r)|^a = \left(\frac{w_0}{w}\mathcal{E}_0 e^{-r^2/w^2}\right)^a \approx \left(\frac{w_0}{w}\mathcal{E}_0\right)^a \left(1 - a\frac{r^2}{w^2}\right). \qquad (3.2.1)$$

This approximation is substituted into the $|\mathcal{E}|^2$ and $|\mathcal{E}|^3$ terms in the nonlinear polarization, and terms are matched based on their order in r^2/w^2. One consequence of this Taylor series approximation is that the critical power obtained using their analysis is one-fourth the critical power that is normally obtained in theories of self-focusing [27, 40]. The factor of four comes from the difference between the true Gaussian beam and the parabolic approximation.

However, other authors make a different aberrationless approximation, based on minimizing the mean square error

$$\int_0^\infty (c_1 + c_2 r^2 - |\mathcal{E}|^2)^2 |\mathcal{E}|^2 \, 2\pi r \, dr \qquad (3.2.2)$$

in the polynomial approximation $c_1 + c_2 r^2$ of the exponential [49]. With their method,

the aberrationless approximation for $|\mathcal{E}|^2$ becomes [49]

$$e^{-2r^2/w^2} \approx \left(\frac{3}{4} - \frac{1}{2}\frac{r^2}{w^2} \right).$$ (3.2.3)

This approximation will change the critical power to the accepted value. This form of the aberrationless approximation was used by Cerullo et al. to study space-time coupling effects in the collapse of femtosecond pulses [50]. The weighting function for the mean square error should remain $|\mathcal{E}|^2$, independent of which power of $|\mathcal{E}|$ is being approximated. When this is done for the plasma term, which depends on $|\mathcal{E}|^3$, the approximation becomes

$$e^{-3r^2/w^2} \approx \left(\frac{16}{25} - \frac{12}{25}\frac{r^2}{w^2} \right).$$ (3.2.4)

The main results of the Schwarz-Diels analysis are the equations for the evolution of the beam width. We present these results here, with the above modification to their approximation. If we apply the new approximations to their analysis, beginning with Equation 32 of their paper [17], their Equation 37, which we will show describes the potential surface, becomes

$$\left(\frac{dw}{dz} \right)^2 = \frac{4}{k^2} \left[\frac{P}{P'_{cr}} - 1 \right] \left[\frac{1}{w^2} - \frac{1}{w_0^2} \right] - \frac{16}{25}\frac{l}{n_0}\beta_4 \left[\frac{1}{w^3} - \frac{1}{w_0^3} \right] P^{3/2} + \frac{w_0^2}{R_0^2},$$ (3.2.5)

and their Equation 38, which is the differential equation for the evolution of the field

width, becomes

$$\frac{d^2w}{dz^2} = -\frac{4}{k^2}\left(\frac{P}{P'_{cr}} - 1\right)\frac{1}{w^3} + \frac{24}{25}\frac{l}{n_0}\beta_4\frac{1}{w^4}P^{3/2}. \tag{3.2.6}$$

where $P'_{cr} = \lambda^2/(2\pi n_0 n_2)$ is four times the P_{cr} in Schwarz and Diels [17]. This gives a more accurate estimate of the true critical power for a Gaussian beam, which is very close to P'_{cr} but not exactly equal [27, 34, 40]. The quantity β_4 is defined in Schwarz and Diels as

$$l\beta_4 = -\left(\frac{2}{\pi}\right)^{3/2} n_3, \tag{3.2.7}$$

where $n_3 = -3.3\times 10^{-31}$ m^2/W$^{3/2}$ is the nonlinear index contribution from the plasma, in intensity units, and $l = 8.9$ mm is the mean free path length of the electrons in the plasma [17].

This ordinary differential equation can be solved numerically, given the input beam width and curvature. Schwarz and Diels present results detailing the oscillatory solutions to this equation [17]. In Section 3.3, we will compare the solutions of this modified equation to results obtained in a numerical propagation of the beam.

However, we can arrive at this same result with a different approach. Wright et al. [27] applied the general variational result of Anderson and Bonnedal [28], discussed in Section 2.3, to the problem of beam propagation under cubic-quintic (n_2 and n_4) nonlinearity. This variational model assumes that the beam is described by the trial function in Equation (2.3.3). Following their notation, we can apply the same result to the Schwarz-Diels case of a cubic-quartic nonlinearity. In Anderson and Bonnedal [28], the nonlinear index terms only contain even powers of $|\mathcal{E}|^2$. However,

their variational analysis is still valid for odd powers, by letting their series index take half-integer values. By considering the $n_3|\mathcal{E}|^3$ term, we find that the equation of motion for the beam width in the case of the UV filaments is

$$\frac{d^2a}{dz^2} = \frac{1}{k^2a^3}\left(1 - \frac{P_{in}}{P_{cr}} + \frac{24}{25}\sqrt{\frac{I_p}{I_0}}\frac{P_{in}}{P_{cr}}\frac{a_0}{a}\right). \tag{3.2.8}$$

Here a is the beam width, and a_0 the initial beam width. Note that there are two different definitions of the beam width; $w = \sqrt{2}a$, where w is the width that Schwarz and Diels use. P_{in} is the input beam power; P_{cr} is the critical power as defined in Equation (2.2.1). I_p is the peak input intensity, and I_0 is a reference intensity defined by $I_0 = (n_2/n_3)^2$. At $I = I_0$, the total nonlinear refractive index change for a plane wave is zero.

For the numbers in Schwarz and Diels, $I_0 = 5.5 \times 10^{16}$ W/m^2. Following Ref. [27], we obtain a self-trapping power for a collimated Gaussian input beam

$$P_{ST} = P_{cr}\left(1 - \frac{24}{25}\sqrt{\frac{I_p}{I_0}}\right)^{-1} \tag{3.2.9}$$

This self-trapping power depends on the input intensity. If $I_p > (25/24)^2\, I_0$, then there will be no self-trapped solution, since power cannot be negative. For UV propagation, this predicts that there will be no self-trapped solution for $I_p > 6.0 \times 10^{16}$ W/m^2. The self-trapped power, however, can be arbitrarily large, as the beam width may increase as intensity approaches the cutoff.

If we convert the equation of motion from a to w and to the notation that Schwarz

and Diels use, we find

$$\frac{d^2w}{dz^2} = -\frac{4}{k^2}\left(\frac{P_{in}}{P_{cr}} - 1\right)\frac{1}{w^3} + \frac{24}{25}\frac{l\beta_4}{n_0}\frac{P_{in}^{3/2}}{w^4} \tag{3.2.10}$$

Here we must note that P_{cr} is the more accurate critical power, which is four times larger than that referenced in Schwarz and Diels. This result is exactly identical to that in Equation (3.2.6), which was obtained by modifying the aberrationless approximation, although it was obtained from a Gaussian beam variational ansatz.

3.3   Verification of Oscillatory Solutions

Schwarz and Diels used an analytical approximate approach to convert the partial differential equation for field propagation into an ordinary differential equation for an effective particle in a potential. They then numerically integrated the ordinary differential equation. We directly solve the numerical partial differential equation for propagation, using a split-step Fourier method, which is detailed in Appendix B.

In Ref. [17], the field is described by its Gaussian beam width, which oscillates in an effective potential well. The potential well model for nonlinear beam propagation is often used and is a direct consequence of using a variational technique [27, 34, 45, 46]. To understand the analogy of the potential well, recognize that

$$\frac{1}{2}\left(\frac{dw}{dz}\right)^2 + U(w) = E \tag{3.3.1}$$

is the equation for the position w of the particle with total energy E as a function of

the coordinate z, which acts as a classical time, as it evolves in the potential $U(w)$.

Equation (3.2.5) can then be written in the form

$$\left(\frac{dw}{dz}\right)^2 = 2\left[E - U(w)\right], \qquad (3.3.2)$$

where

$$U(w) = -\frac{2}{k^2}\left(\frac{P}{P_{cr}} - 1\right)\frac{1}{w^2} + \frac{8}{25}\frac{l\beta_4}{n_0}\frac{P^{3/2}}{w^3} \qquad (3.3.3)$$

is the effective potential and

$$E = U(w_0) + \frac{w_0^2}{2R_0^2} \qquad (3.3.4)$$

is the total energy, which is conserved. The initial width w_0 of the beam gives the particle's initial location; the initial width of the beam divided by its initial radius of curvature gives its initial velocity. This can also be seen from Equation 37 of Schwarz and Diels [17], or Equation (3.2.5) of this dissertation, by setting $w = w_0$. Thus the initial velocity corresponds to any initial linear focusing or defocusing with which the beam is prepared.

If the initial conditions are near the bottom of the well, the oscillations in the width are small. However, if the initial conditions displace the particle far from the well minimum, there are larger oscillations. The potential $U(w)$ approaches zero as $w \to \infty$. If the particle has total energy E greater than zero, it is not bound and the beam will diffract. This can be caused by the initial beam being too narrow, or having too much initial curvature.

We use the Schwarz-Diels semi-analytical solution with improved aberrationless approximation described earlier, to achieve closer agreement between the direct numerical simulation and their predictions. As an example, Figure 3.1 shows the potential surfaces corresponding to beam powers of 100 MW, 200 MW, and 500 MW. The
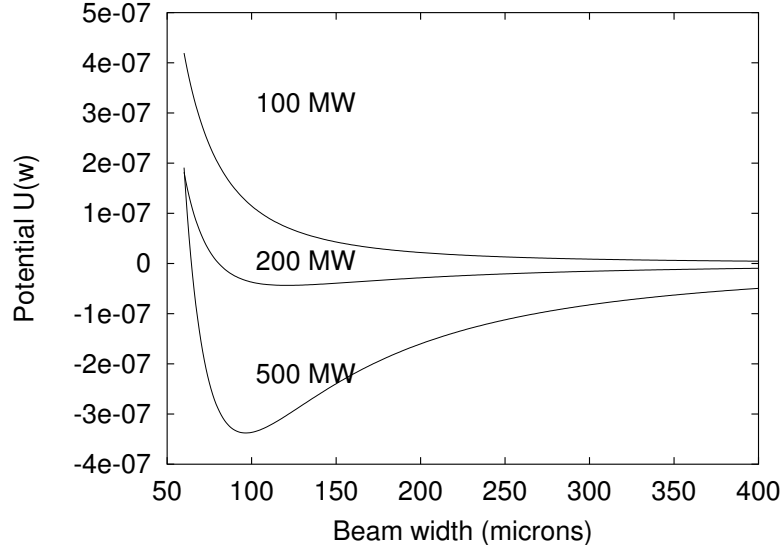

Figure 3.1: Potential wells for beam powers at 100, 200, and 500 MW.

surface for 200 MW is shallower than the surface for 500 MW. The 200 MW surface represents states which are more weakly bound. The 100 MW surface is for a power below the critical power of 125 MW, so the potential surface no longer supports a bound state. The location of the bound state minimum depends on the power as well, according to Equation (3.3.5). Since the binding strength of the potential depends on the power in the beam, absorption losses will cause the potential to change, and we will observe this in the oscillatory solution.

To solve the modified evolution described in Equation (3.2.5), we use the ODE

solver in *Mathematica*. The initial condition for the radius of curvature of the beam is $dw/dz|_{z=0} = w_0/R_0$. For simplicity, start with a flat beam ($R_0 = \infty$), so the initial width is also the waist. The location of the equilibrium, or steady state, beam waist in Equation (3.2.5), which is the modified version of Equation 37 of Schwarz and Diels, depends on power as

$$w_{eq}(P) = \frac{0.24k^2 l \beta_4}{n_0} \frac{P^{3/2}}{P/P_{cr} - 1}. \qquad (3.3.5)$$

In the case that we wish to model absorption, the evolution of the beam power, in Equation 18 of Schwarz and Diels, is unchanged by the modification, so we reproduce it here: [17]

$$\frac{1}{P}\frac{dP}{dz} = -\beta_3 \frac{P^2}{w^4} - \beta_4 \frac{P^{3/2}}{w^3}. \qquad (3.3.6)$$

During the split-step numerical simulation, we characterize the beam width by a second moment computation, described in Equation (5.5.1). An example of the case where the initial conditions are near the bottom of the well is shown in Figure 3.2. Here the power was 500 MW and the initial width 100 μm, with no absorption. The frequency of the simulated oscillations roughly matches that of the predicted oscillations, but the prediction does not account for the observed decay in amplitude. For other values, such as those shown in Figure 3.3, the initial conditions lead to larger oscillations. In the second case the initial width was chosen to be 200 μm. In the field history plot, Figure 3.3(b), the beam grows in intensity and decreases its width, while shedding rings during the oscillations. Figure 3.4 shows the evolution of a beam where the power is 200 MW and initial width is 100 μm. Here there are fairly

consistent, larger amplitude oscillations, but again they are not constant. For starting powers larger than 1 GW, the beam quickly sheds much of its power into rings, so that the peak intensity is reduced. This is consistent with the existence of a maximum trapping intensity, although the observed value for this maximum trapping intensity is roughly 4×10^{16} W/m^2, instead of 6×10^{16} W/m^2 as predicted in Section 3.2. The variational approach provides an estimate for the order of magnitude of such a quantity, but cannot capture the details of features such as rings.

The oscillations appear to either dampen in amplitude or change chaotically for these cases. The predictions, however, are based on a potential model with no loss terms, in which the particle should oscillate with a constant amplitude between two extremes. The apparent loss in the potential model should not be confused with nonlinear propagation losses, which we have not yet considered. The damping is caused by the fact that the evolving solution has to adjust itself, possibly by shedding power into rings, to fit the nonlinear response and match a solution of the propagation equation. If the initial condition is far from the equilibrium solution, the Gaussian beam approximation will be temporarily violated as the beam changes form. Any power that is diffracted in a ring will be absorbed by absorbing boundary conditions at the edges of the grid. After some propagation, the damping reduces, as the evolving solution changes from an initial Gaussian to a solution that oscillates in an stable fashion. The oscillatory propagation in these results is similar to that observed in studies of a medium with cubic-quintic nonlinearity [27, 45].

If propagation losses are present, the power in the beam is reduced, which leads to a shallower potential. If the power loss is not extreme, it should act as an adiabatic
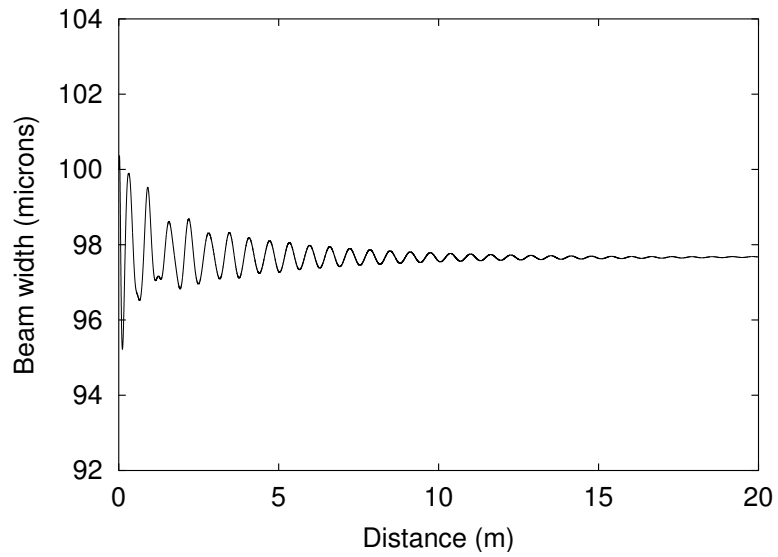
(a) Beam width using split-step evolution
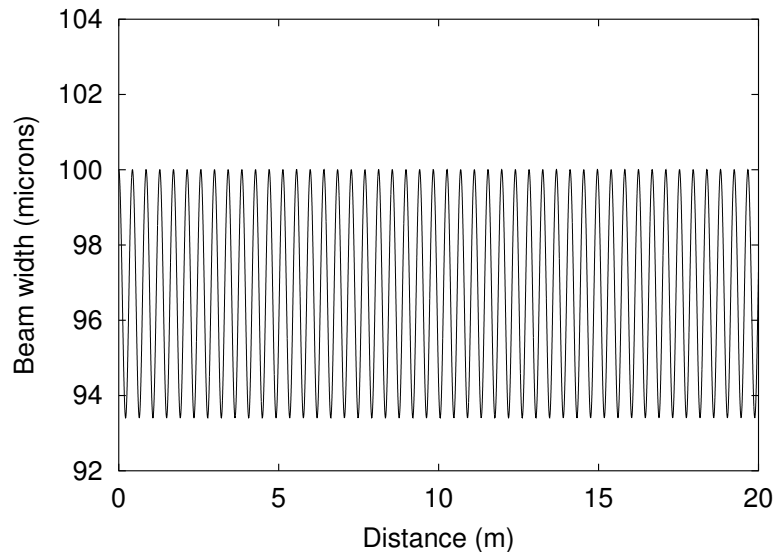
(b) Predicted beam oscillations using modified Schwarz-Diels model

Figure 3.2: Beam evolution for power of 500 MW, initial width of 100 μm, and no absorption. This set of initial conditions corresponds to a near steady state solution.

(a) Beam width using split-step evolution, together with regular oscillations predicted by Schwarz-Diels model

(b) Early portion of field history using split-step evolution. The plot shows a cross section of the field amplitude, as a function of propagation distance.

Figure 3.3: Beam evolution for power of 500 MW, initial width of 200 μm, and no absorption. In this case the initial width is far from steady state, leading to nonlinear oscillations.
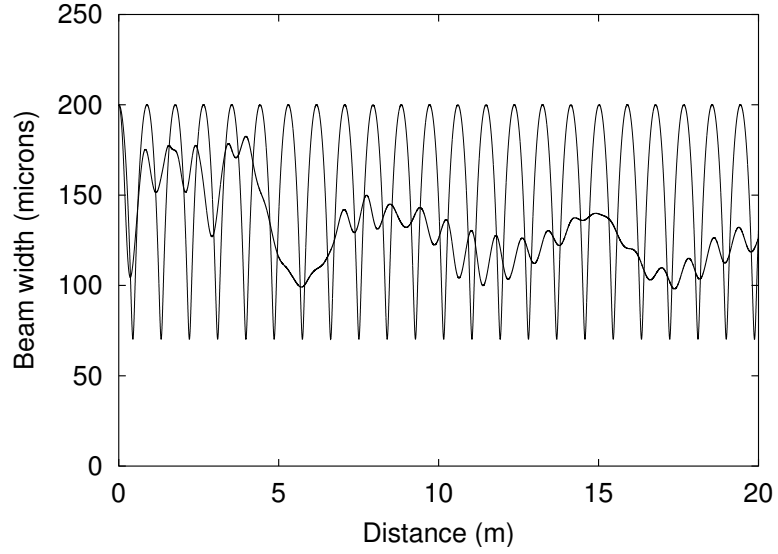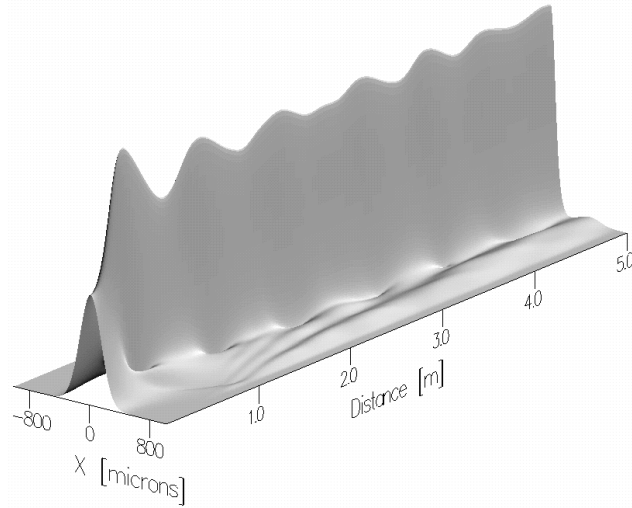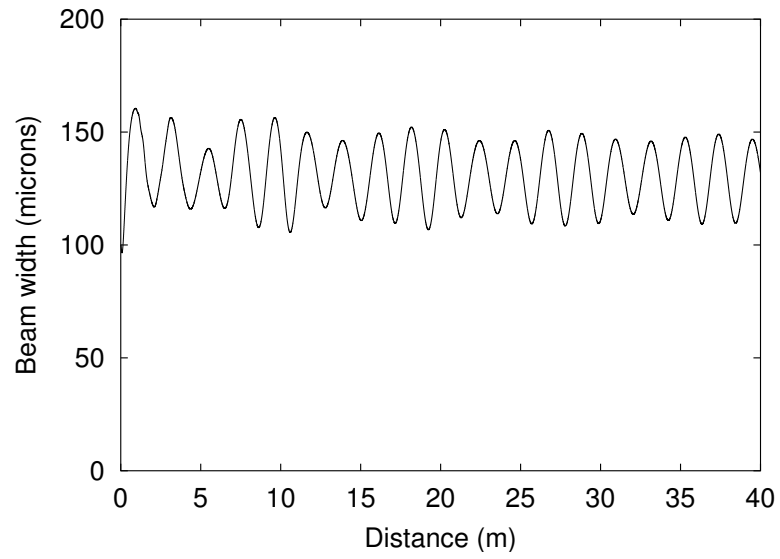
(a) Beam width using split-step evolution
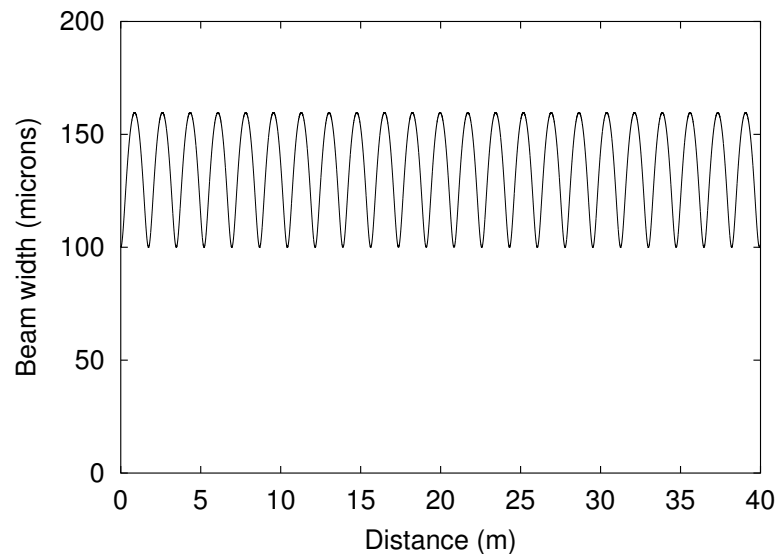
(b) Predicted beam oscillations using modified Schwarz-Diels model
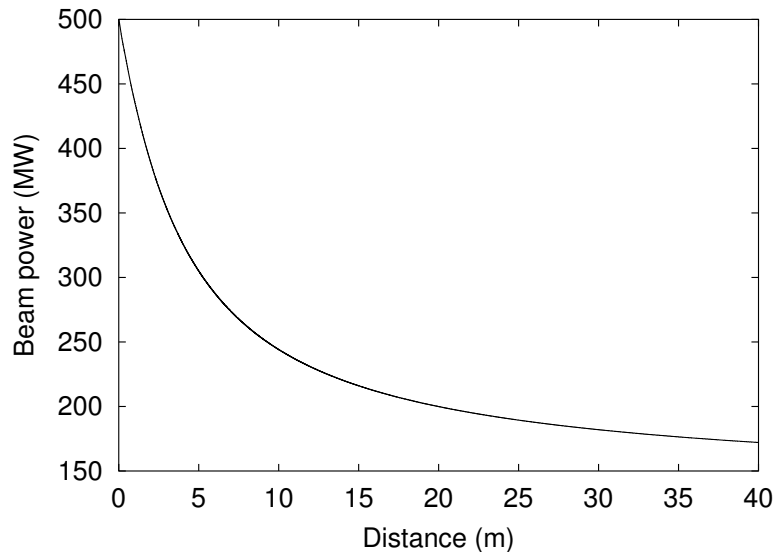
Figure 3.4: Beam evolution for power of 200 MW, initial width of 100 μm, and no absorption.

change in the potential surface. The oscillations should become larger in amplitude, but lower in frequency, as power is lost. This is shown for one case in Figure 3.5. For this simulation, we included MPI losses and plasma absorption using the values from Table 3.1. The beam power appears to decay roughly exponentially, but since the loss is nonlinear, the loss rate decreases as less power remains. As power is lost, the effective potential becomes shallower; one might expect the oscillations to thus increase in amplitude. However, they do not do this; they are instead somewhat chaotic. They will disappear once the beam power drops below the critical power; then the potential is unbound, and the beam width continues to increase as it diffracts. The particular nature of the oscillations in this figure may be influenced by numerical effects such as reflections from the absorbing boundary conditions. However, the important point is that the beam width follows a general trend dictated by the slowly decreasing power in the beam.

Recall that starting with a 500 MW Gaussian beam that is 100 μm wide, for the n_2 and n_3 parameters in Schwarz and Diels [17], we find that the beam is close to an exact steady state solution. The location of this initial condition is near the bottom of the well on the potential surface for 500 MW shown in Figure 3.1. However, even choosing an initial condition with the beam width at the precise bottom of the potential well will not yield us an exact steady solution, because the potential picture is approximate, based on a Gaussian ansatz; the exact solution is not a Gaussian.
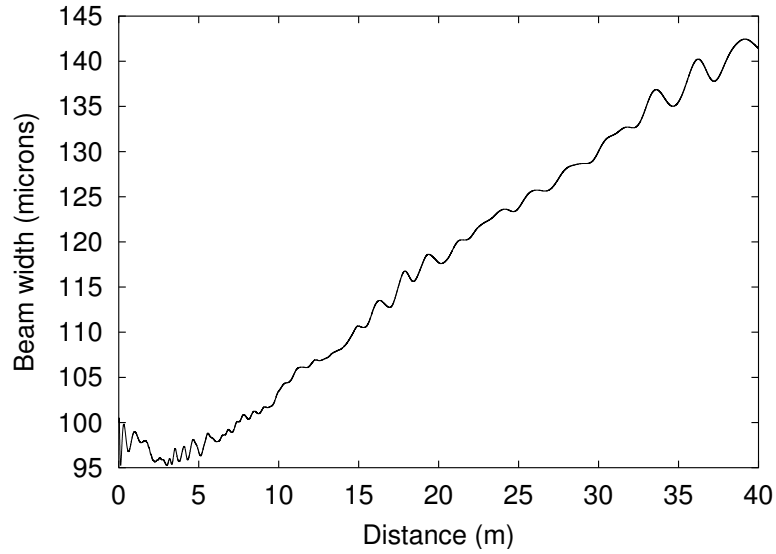
(a) Beam width using split-step evolution

(b) Beam power

Figure 3.5: Beam evolution for 500 MW initial power, initial width of 100 μm, and absorption losses. The beam width oscillates around a changing equilibrium position. The loss rate decreases for longer distances, due to the nonlinear nature of the absorption.

3.4 Construction of Exact Steady State Solution

For completeness, and for diagnostics that will be a part of the stability analysis discussed later, we wish to construct exact steady state trapped beam solutions to the propagation equation, within numerical precision limitations. Let a steady state solution be denoted by $\mathcal{E}_0(r, z)$.

To accurately find $\mathcal{E}_0$, we investigate the solution of the eigenvalue equation that corresponds to the steady state solution. The exact solutions will be characterized by their peak intensity. By solving this boundary value problem with the shooting method, we obtain a radial profile of $\mathcal{E}_0$. This radial profile is then extended to a full x-y grid using interpolation. We look for a steady state solution to the simplified propagation equation

$$\frac{\partial \mathcal{E}}{\partial z} = \frac{i}{2k}\nabla_\perp^2 \mathcal{E} + ik_0(n_2|\mathcal{E}|^2 + n_3|\mathcal{E}|^3)\mathcal{E}. \tag{3.4.1}$$

Let

$$\mathcal{E}(r, z) = \mathcal{E}(r)e^{i\beta z}. \tag{3.4.2}$$

with $\mathcal{E}(r)$ real. Then,

$$i\beta\mathcal{E}(r)e^{i\beta z} = \frac{i}{2k}\nabla_\perp^2 \mathcal{E}(r)e^{i\beta z} + ik_0 \left[n_2\mathcal{E}(r)^2 + n_3\mathcal{E}(r)^3\right]\mathcal{E}(r)e^{i\beta z}, \tag{3.4.3}$$

and

$$\nabla_\perp^2 \mathcal{E}(r) = 2k\beta\mathcal{E}(r) - ik_0 \left[n_2\mathcal{E}(r)^2 + n_3\mathcal{E}(r)^3\right]\mathcal{E}(r) \equiv f(\mathcal{E}). \tag{3.4.4}$$

Recall that we are using intensity units for $\mathcal{E}$, so $\mathcal{E}^2$ is an intensity. In polar coordinates

$$\frac{\partial^2 \mathcal{E}}{\partial r^2} + \frac{1}{r}\frac{\partial \mathcal{E}}{\partial r} = f(\mathcal{E}). \tag{3.4.5}$$

For a given peak amplitude A_0, the solution will have the initial conditions that $\mathcal{E}(r = 0) = A_0$, and that $\partial \mathcal{E}/\partial r|_{r=0} = 0$. Then, given a guess is for β, we solve the ordinary differential equation, starting at $r = 0$ and running until r is several times larger than the extent of the expected solution.

This equation caused difficulty for the numerical integration routine in *Mathematica*, due to the singularity in the equation at $r = 0$. However, a finite difference approach can be used to handle the singularity. We represent the value of $\mathcal{E}(r)$ by values on a discrete uniform grid $a_0, a_1, \ldots, a_N$. The a_m are values of $\mathcal{E}(r)$ at the points $r = m\Delta$, where Δ is the grid spacing in r.

The $\nabla_\perp^2$ operator is approximated by the following difference formula:

$$\nabla_\perp^2 \mathcal{E}\Big|_n = \frac{\partial^2 \mathcal{E}}{\partial r^2} + \frac{1}{r}\frac{\partial \mathcal{E}}{\partial r}\Big|_n = \frac{a_{n+1} - 2a_n + a_{n-1}}{\Delta^2} + \frac{1}{n\Delta}\frac{a_{n+1} - a_{n-1}}{2\Delta} \tag{3.4.6}$$

$$= \frac{(2n+1)a_{n+1} - 4na_n + (2n-1)a_{n-1}}{2n\Delta^2}. \tag{3.4.7}$$

Thus, at point n,

$$\frac{(2n+1)a_{n+1} - 4na_n + (2n-1)a_{n-1}}{2n\Delta^2} = f(a_n), \tag{3.4.8}$$

and we then derive an relation which can be iterated:

$$a_{n+1} = \frac{4n}{2n+1}a_n - \frac{2n-1}{2n+1}a_{n-1} + \frac{2n}{2n+1}\Delta^2 f(a_n). \tag{3.4.9}$$

This iteration equation is valid for $n \geq 1$. The initial conditions present a slight difficulty. We know that $a_0 = A_0$, but we need to know a value for a_1. The second derivative at $n = 0$ must be handled with care. To represent $\nabla_\perp^2$, which is a 2D operator, on a 2D spatial (XY) grid using a finite difference technique, the value for $\nabla_\perp^2$ is approximated by

$$\nabla_\perp^2 \mathcal{E}\big|_{0,0} = \frac{a_{1,0} - 2a_{0,0} + a_{-1,0}}{\Delta^2} + \frac{a_{0,1} - 2a_{0,0} + a_{0,-1}}{\Delta^2}, \tag{3.4.10}$$

where now the two indices for a represent the X and Y directions on the grid. We do not define this function on a full XY grid, but we can approximate this difference as

$$\nabla_\perp^2 \mathcal{E}\big|_0 = \frac{4a_1 - 4a_0}{\Delta^2}, \tag{3.4.11}$$

since, due to the azimuthal symmetry, the four nearest neighbors all have the value a_1. Then we can get the condition for a_1:

$$\nabla_\perp^2 \mathcal{E}\big|_0 = \frac{4a_1 - 4a_0}{\Delta^2} = f(A_0), \tag{3.4.12}$$

$$a_1 = a_0 + \frac{\Delta^2}{4}f(A_0). \tag{3.4.13}$$

With the initial values for a_0 and a_1 now set, we guess an initial value for β and then use the "shooting" method to adjust β until the value of the solution $\mathcal{E}(r)$ for large r approaches zero. In practice, once the guess for β is good, the solution will decay to zero at some distance, but for sufficiently large r, the solution then diverges from zero due to lack of precision. However, if the distance for which the solution diverges is larger than the grid we need in propagation, we can truncate the solution earlier. This approach gives the solution for $\mathcal{E}(r)$ on a uniform grid in r. Then the solution is interpolated from the radial grid to a 2D grid to generate $\mathcal{E}(x,y)$. This solution is saved, and will be used as the steady state field $\mathcal{E}_0$ in the stability analysis and three dimensional propagation in later chapters. This exact steady state beam solution for a peak intensity of 3.2×10^{16} W/m^2 is shown in Figure 3.6. We chose this value for the intensity because 3.2×10^{16} W/m^2 is also the approximate peak intensity for a Gaussian beam with power 500 MW. The value of β for this solution is approximately 8.11 m^{-1}.

We first test the generated $\mathcal{E}_0$ solution by propagating it in the 2D propagation code with the correct conditions for n_2 and n_3. The code has two ways of handling the plasma term, either by using an effective n_3, or the term $-\sigma\omega\tau\rho/2$. Recall that we chose the values for the the effective n_3 and the rates used to generate ρ (the $\beta^{(3)}$ value) to be consistent. When the correct solution for $\mathcal{E}_0$ is loaded, the field stays constant in the propagation code, up to one part in 10^5 over a distance scale of several meters, if no losses are present. Thus the steady state solution also provides a verification of the propagation code, as well as the two different approaches to handling the plasma term in the code.
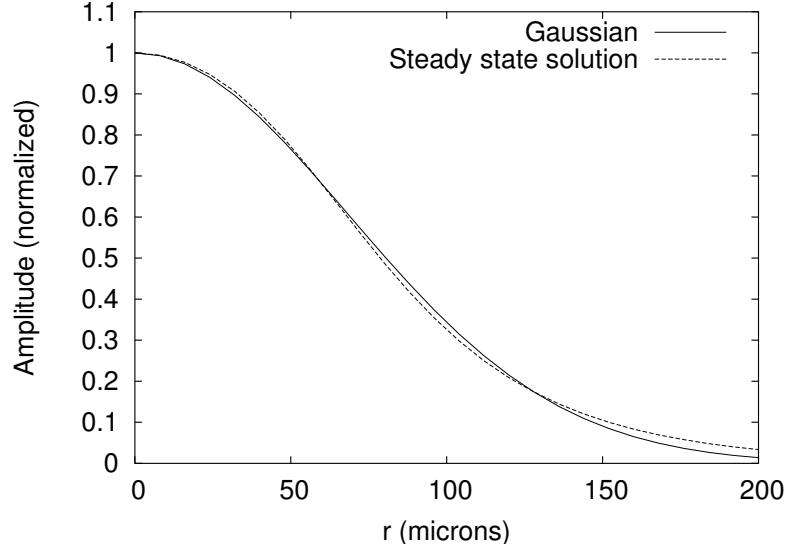
Figure 3.6: Example of numerically constructed steady state solution. This solution contains a power of roughly 470 MW, and the beam width is roughly 97 μm. The peak intensity, which defines this solution, is 3.2×10^{16} W/m^2 in this example. Also shown is a Gaussian profile, with the same peak intensity and width.

The steady state solution for this power is visually close to a Gaussian, but not an exact match. For pure self-focusing, the self-similar collapse solution is the Townes profile [34, 51, 52]; in that case the difference between the Gaussian and Townes profiles is important, due to the unstable nature of the solution. For the UV problem under the Schwarz-Diels model, an initial Gaussian may be nearly steady state if chosen correctly. This indicates that the Gaussian ansatz in the Schwarz-Diels model can be a good guess, when describing steady state or near steady state solutions. As we saw, it is not as appropriate when describing non-equilibrium solutions.

The results from this section confirm the oscillatory solutions predicted by Schwarz and Diels, and demonstrate that the simplified propagation equation has exact steady

state solutions for CW beams, up to a phase change as the beam propagates.

The next question is whether long ultraviolet pulses can be sent through air, maintaining their shape over long propagation distances, and whether the current long pulse model can describe this. To answer this question, we must further scrutinize the steady state model representation of long laser pulses. As mentioned earlier, Schwarz and Diels impose upper and lower limits on the pulse length to make the approximation valid, so first the pulse must satisfy these constraints. The steady state model also assumes that the plasma responds instantaneously to changes in the electric field. Thus it has no way to incorporate any temporal transient effects or instabilities that may arise from the finite response time of the plasma to the electric field, and this is mentioned in the analysis [17]. In the following chapters, we develop a stability model, and simulate the propagation of long pulses to investigate these effects.

CHAPTER 4

STABILITY

4.1 Introduction

The stability of solutions to nonlinear optical propagation equations has been studied for many cases. The question of stability has been considered for the mathematical balance in a beam solution between self-focusing and diffraction, and this is known to be an unstable situation [1, 35, 34, 2, 53]. Only the mathematically exact solution with precisely one critical power will propagate unchanged; any deviation of the beam power from the critical power results in the beam solution collapsing or diffracting indefinitely.

More detailed models consider the spatiotemporal instability of the solutions to the nonlinear Schrödinger equation (NLSE) [5, 54, 55]. Liou et al. studied the spatiotemporal instability of an NLSE that only contained GVD and self-focusing terms [53]. They found that under self-focusing conditions, the interaction of spatial and temporal modulations led to an instability for either normal or anomalous GVD, which led to spatiotemporal chaos developing in the solution.

The addition of some form of saturation, such as the generation of plasma, stops filaments from collapsing indefinitely. The balance between the self-focusing collapse and saturation has been thought to explain the long life of the observed light filaments, or "bullets" that are created in beams with power equal to several critical powers [56].

However, the delayed responses of the Kerr effect and the plasma defocusing have

been shown to create instabilities in short (single picosecond scale) pulses [32]. Kandidov et al. attributed the filamentation or breakup of short pulses to these instabilities [32].

Bian et al. studied the instability of plasmas generated by laser pulses [57], which they denote the ionization scattering instability. They identified a dispersion relation for the growth of unstable modes. Our analysis in Sections 4.3 and 4.4 is similar to their approach; however, they consider the impact of this instability for short (less than a picosecond) pulses.

Since many of these investigations are done for short time scales, the instabilities are identified as the breakup mechanism for a short pulse into filaments [21, 32, 34, 58]. However, this raises the question of the stability of the UV long pulse solutions, which are based on an instantaneous Kerr and instantaneous plasma defocusing response. Additionally, the Schwarz-Diels model assumes that the leading edge of the pulse can develop into the steady state middle region. This requires that the steady state solution be stable, since the leading edge, which deviates from steady state, has to eventually adjust itself into a steady state solution for the model to be valid. Our analysis will first use a linear perturbation model to investigate this question of stability.

4.2 Purely Spatial Perturbations

In general, we would like to understand the growth of unstable modes as a function of both spatial frequency $k_\perp$ and temporal frequency, which we denote by Ω.

First, examine the instability for zero temporal frequency, that is, a purely spatial modulational instability for a CW solution. We use an approach similar to that of Cerda [45]. Consider the propagation equation

$$\frac{\partial \mathcal{E}}{\partial z} = \frac{i}{2k}\nabla_\perp^2 \mathcal{E} + ik_0 \Delta n(|\mathcal{E}|^2)\mathcal{E}, \tag{4.2.1}$$

where $\Delta n(|\mathcal{E}|^2)$ is a general instantaneous nonlinear index change. For the long pulse UV problem

$$\Delta n(|\mathcal{E}|^2) = n_2|\mathcal{E}|^2 + n_3(|\mathcal{E}|^2)^{3/2}. \tag{4.2.2}$$

An exact plane wave solution is

$$\mathcal{E}_0(x, y, z) = \mathcal{E}_0 e^{ik_0\overline{\Delta n}z}, \tag{4.2.3}$$

where $\overline{\Delta n} = \Delta n(|\mathcal{E}_0|^2)$. For the cubic-quartic nonlinearity in the UV problem, the propagation constant, denoted $\bar{k}$, for the exact plane wave solution is then

$$\bar{k} = k_0\overline{\Delta n} = k_0 n_2|\mathcal{E}_0|^2 + k_0 n_3|\mathcal{E}_0|^3. \tag{4.2.4}$$

For a beam solution, this plane wave value provides a magnitude estimate, but not an exact prediction, for the value of the propagation constant $\bar{k}$.

Consider a perturbed solution

$$\mathcal{E}(x, y, z) = \mathcal{E}_0 e^{ik_0\overline{\Delta n}z}\left(1 + \epsilon_+(x, y, z) + \epsilon_-(x, y, z)\right), \tag{4.2.5}$$

where ϵ_+ and ϵ_- are small perturbation fields. Note that to first order

$$|\mathcal{E}|^2 \approx |\mathcal{E}_0|^2 + |\mathcal{E}_0|^2(\epsilon_+ + \epsilon_- + c.c), \tag{4.2.6}$$

so to first order, we can approximate

$$\Delta n(|\mathcal{E}|^2) \approx \Delta n(|\mathcal{E}_0|^2) + |\mathcal{E}_0|^2(\epsilon_+ + \epsilon_- + c.c)\frac{\partial \Delta n}{\partial|\mathcal{E}|^2}. \tag{4.2.7}$$

Insert the expression for $\mathcal{E}$ into Equation (4.2.1) for the propagation. After collecting terms, we obtain equations for the evolution of the perturbations:

$$\begin{aligned}
\frac{\partial \epsilon_+}{\partial z} &= \frac{i}{2k}\nabla_\perp^2 \epsilon_+ + ik_0\frac{\partial \Delta n}{\partial|\mathcal{E}|^2}|\mathcal{E}_0|^2(\epsilon_+ + \epsilon_-^*) \\
\frac{\partial \epsilon_-^*}{\partial z} &= -\frac{i}{2k}\nabla_\perp^2 \epsilon_+ - ik_0\frac{\partial \Delta n}{\partial|\mathcal{E}|^2}|\mathcal{E}_0|^2(\epsilon_+ + \epsilon_-^*).
\end{aligned} \tag{4.2.8}$$

Assume that the perturbation fields are plane waves such that

$$\begin{aligned}
\epsilon_+(x,y,z) &= u_+\exp(\lambda z + i\mathbf{k}_\perp \cdot \mathbf{r}) \\
\epsilon_-(x,y,z) &= u_-\exp(\lambda^* z - i\mathbf{k}_\perp \cdot \mathbf{r}).
\end{aligned} \tag{4.2.9}$$

This ansatz for the form of the fields, when inserted into the coupled evolution equations above, gives a matrix equation:

$$i\begin{bmatrix} -T+V & V \\ -V & T-V \end{bmatrix}\begin{bmatrix} u_+ \\ u_-^* \end{bmatrix} = \lambda \begin{bmatrix} u_+ \\ u_-^* \end{bmatrix}, \tag{4.2.10}$$

where

$$T = k_\perp^2/2k, \qquad V = k_0 \frac{\partial \Delta n}{\partial |\mathcal{E}|^2} |\mathcal{E}_0|^2. \tag{4.2.11}$$

The eigenvalues λ satisfy

$$\lambda^2 = 2TV - T^2 = T(2V - T). \tag{4.2.12}$$

Note that T and V are both real, and $T \geq 0$. If $V < 0$, then $\lambda^2 < 0$, so λ is imaginary, and the system is stable. But if $V > 0$, $\lambda^2 > 0$, so it is unstable for $T < 2V$. T corresponds to the transverse wave vector of the instability, and V corresponds to the relative strength of the self-focusing versus defocusing. Figure 4.1 shows this for the case of positive V. For our UV problem

$$V = k_0 \frac{\partial \Delta n}{\partial |\mathcal{E}|^2} |\mathcal{E}_0|^2 = k_0 n_2 |\mathcal{E}_0|^2 + \frac{3}{2} k_0 n_3 |\mathcal{E}_0|^3, \tag{4.2.13}$$

so if $n_2 + 1.5 \, n_3 |\mathcal{E}_0| > 0$, there is an instability for certain values of $k_\perp$. For the n_2 and n_3 that describe UV propagation in air, this cutoff value corresponds to a peak intensity of 2.4×10^{16} W/m^2. The form of this result is similar to that of Cerda [45], but with our nonlinear response containing both n_2 and n_3 terms. The combination of the two terms allows the possibility that the system is stable for $\Omega = 0$, unlike the result for n_2 only. In the next section, we will examine the stability for nonzero Ω, and we will obtain the above results as a limiting case.
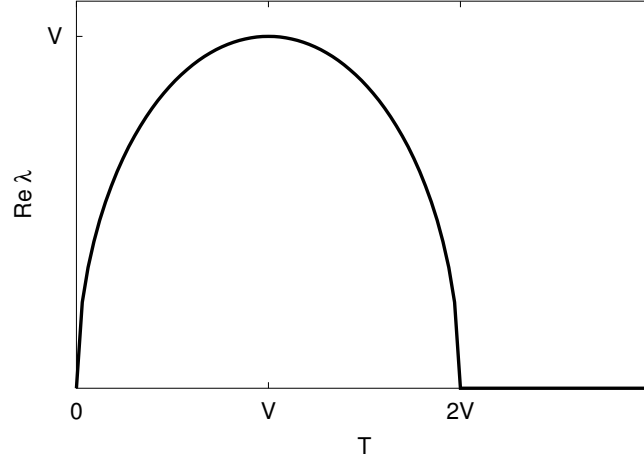
Figure 4.1: Growth rate Re λ for spatial perturbations. The growth rate is plotted as a function of the spatial frequency parameter T, for the case of positive V. For spatial frequencies that correspond to $T < 2V$, the plane wave solution is unstable.

4.3 Linear Stability Analysis

To model the stability of long filaments with respect to fluctuations in time and space, we abandon the approximation that the plasma density depends only on a power of the electric field, and return to using a time dependent evolution equation for the plasma. Consider the propagation equation, neglecting losses, combined with a simple model for the plasma:

$$\frac{\partial \mathcal{E}}{\partial z} = \frac{i}{2k}\nabla_\perp^2 \mathcal{E} + ik_0 n_2 |\mathcal{E}|^2 \mathcal{E} - i\frac{\sigma \omega \tau}{2}\rho \mathcal{E}, \qquad (4.3.1)$$

$$\frac{\partial \rho}{\partial t} = b|\mathcal{E}|^{2K} - a\rho^2. \qquad (4.3.2)$$

Assume that a steady state solution can be found with $\mathcal{E}_0(r, z) = u(r)e^{i\bar{k}z}$. The steady state value for the plasma density will be

$$\rho_0(r) = \sqrt{\frac{b}{a}}|u(r)|^K. \tag{4.3.3}$$

Let us investigate a time-perturbed solution consisting of

$$\mathcal{E}(r, z, t) = \mathcal{E}_0(r, z) + \mathcal{E}_+(r, z)e^{-i\Omega t} + \mathcal{E}_-(r, z)e^{i\Omega t}, \tag{4.3.4}$$

$$\rho(r, z, t) = \rho_0(r) + \rho_+(r, z)e^{-i\Omega t} + \rho_+^*(r, z)e^{i\Omega t}, \tag{4.3.5}$$

where $\mathcal{E}_+$, $\mathcal{E}_-$, and ρ_+ are small compared to $\mathcal{E}$ and ρ respectively. Since the plasma density ρ is real, we must use ρ_+ and ρ_+^* as the perturbation coefficients for the plasma.

First, we solve the plasma equation to find $\rho_+(r, z)$, by inserting the perturbed solution for ρ, and keeping only terms linear in the perturbations. We find that

$$\begin{aligned}
\frac{\partial \rho}{\partial t} &= -i\Omega\rho_+e^{-i\Omega t} + i\Omega\rho_+^*e^{i\Omega t} \\
&= b|\mathcal{E}_0|^{2k} + bK|\mathcal{E}_0|^{2K-2}\left[\left(\mathcal{E}_0^*\mathcal{E}_+ + \mathcal{E}_0\mathcal{E}_-^*\right)e^{-i\Omega t} + c.c.\right] \\
&\quad - a\rho_0^2 - 2a\rho_0\left(\rho_+e^{-i\Omega t} + c.c.\right).
\end{aligned} \tag{4.3.6}$$

The zero order terms cancel, by the definition of ρ_0. Equating terms that oscillate as $e^{-i\Omega t}$ gives

$$-i\Omega\rho_+ = -2a\rho_0\rho_+ + Kb|\mathcal{E}_0|^{2K-2}\left(\mathcal{E}_0^*\mathcal{E}_+ + \mathcal{E}_0\mathcal{E}_-^*\right), \tag{4.3.7}$$

and we find

$$\rho_+ = \frac{Kb|\mathcal{E}_0|^{2K-2}\left(\mathcal{E}_0^*\mathcal{E}_+ + \mathcal{E}_0\mathcal{E}_-^*\right)}{2a\rho_0 - i\Omega}. \tag{4.3.8}$$

With the terms oscillating as $e^{i\Omega t}$, we obtain the complex conjugate of this equation. Next, we take this solution for ρ_+ and the full form for $\mathcal{E}$, insert them into the propagation equation (4.3.1), and expand terms, keeping only linear perturbation terms. For the zero order terms we obtain

$$\frac{\partial \mathcal{E}_0}{\partial z} = \nabla_\perp^2 \mathcal{E}_0 + ik_0 n_2 |\mathcal{E}_0|^2 \mathcal{E}_0 - i\frac{\sigma\omega\tau}{2}\rho_0\mathcal{E}_0, \tag{4.3.9}$$

where we assume by construction that $\mathcal{E}_0$ and ρ_0 satisfy this equation. For the terms oscillating as $e^{-i\Omega t}$ we obtain

$$\begin{aligned}
\frac{\partial \mathcal{E}_+}{\partial z} = \frac{i}{2k}\nabla_\perp^2 \mathcal{E}_+ + ik_0 n_2 \left[2|\mathcal{E}_0|^2\mathcal{E}_+ + \mathcal{E}_0^2\mathcal{E}_-^*\right] \\
- i\frac{\sigma\omega\tau}{2}\left(\rho_0\mathcal{E}_+ + \frac{Kb|\mathcal{E}_0|^{2K-2}}{2a\rho_0 - i\Omega}\left[|\mathcal{E}_0|^2\mathcal{E}_+ + \mathcal{E}_0^2\mathcal{E}_-^*\right]\right),
\end{aligned} \tag{4.3.10}$$

and for the terms oscillating as $e^{i\Omega t}$ we obtain

$$\begin{aligned}
\frac{\partial \mathcal{E}_-}{\partial z} = \frac{i}{2k}\nabla_\perp^2 \mathcal{E}_- + ik_0 n_2 \left[2|\mathcal{E}_0|^2\mathcal{E}_- + \mathcal{E}_0^2\mathcal{E}_+^*\right] \\
- i\frac{\sigma\omega\tau}{2}\left(\rho_0\mathcal{E}_- + \frac{Kb|\mathcal{E}_0|^{2K-2}}{2a\rho_0 + i\Omega}\left[|\mathcal{E}_0|^2\mathcal{E}_- + \mathcal{E}_0^2\mathcal{E}_+^*\right]\right).
\end{aligned} \tag{4.3.11}$$

These two equations give the evolution of the coupled perturbation fields $\mathcal{E}_+$ and $\mathcal{E}_-$.

4.4 Plane Wave Perturbations

Let us first solve these equations by using an ansatz for the form of $\mathcal{E}_+$ and $\mathcal{E}_-$ that separates the dependence in z from the dependence in the transverse spatial coordinate. Recall that $\mathcal{E}_0(r, z)$ has the form $u(r)e^{i\bar{k}z}$. If we use the ansatz

$$\mathcal{E}_+(r, z) = u_+(r)e^{\lambda z} \qquad \mathcal{E}_-(r, z) = u_-(r)e^{\lambda^* z}, \qquad (4.4.1)$$

the $\exp(2i\bar{k}z)$ dependence of the $\mathcal{E}_0^2$ terms will not be cancelled. However, if we modify the ansatz so that the z dependence of $\mathcal{E}_0^2\mathcal{E}_-^*$ matches that of $\mathcal{E}_+$, we will get cancellation. To do this, we first make the simplifying assumption that $\mathcal{E}_0$, u_+, and u_- are independent of transverse coordinate. We thus treat the case for which the steady state solution is a plane wave, as in the previous section. Let the perturbation fields also be plane waves, with the same propagation constant as the $\mathcal{E}_0$ solution:

$$\mathcal{E}_+(r, z) = u_+ \exp(\lambda\, z + i\bar{k}z + i\mathbf{k}_\perp \cdot \mathbf{r})$$
$$\mathcal{E}_-(r, z) = u_- \exp(\lambda^* z + i\bar{k}z - i\mathbf{k}_\perp \cdot \mathbf{r}), \qquad (4.4.2)$$

where $\mathbf{k}_\perp$ is the transverse wave vector $k_x\hat{x} + k_y\hat{y}$ and $\mathbf{r}$ is the transverse coordinate $x\hat{x} + y\hat{y}$. When we insert these forms into the above equations for $\mathcal{E}_+$ and $\mathcal{E}_-$ and cancel the exponential dependence, we find

$$(i\bar{k} + i\bar{k}_\perp + \lambda)u_+ = iB\left[2u_+ + u_-^*\right] - iC\left(\rho_0 u_+ + A(\Omega)\left[u_+ + u_-^*\right]\right), \qquad (4.4.3)$$

$$(i\bar{k} + i\bar{k}_\perp + \lambda^*)u_- = iB\left[2u_- + u_+^*\right] - iC\left(\rho_0 u_- + A^*(\Omega)\left[u_- + u_+^*\right]\right), \qquad (4.4.4)$$

where

$$A(\Omega) \equiv \frac{Kb|\mathcal{E}_0|^{2K}}{2a\rho_0 - i\Omega} \qquad B \equiv k_0 n_2 |\mathcal{E}_0|^2 \qquad C \equiv \frac{\sigma\omega\tau}{2}, \tag{4.4.5}$$

and the quantity $\bar{k}_\perp$, from the contribution from the $\nabla_\perp^2$ term, is defined by

$$\frac{i}{2k}\nabla_\perp^2 \mathcal{E}_+ = \frac{i}{2k}\nabla_\perp^2 \mathcal{E}_- = -i\frac{k_\perp^2}{2k} \equiv -i\bar{k}_\perp, \tag{4.4.6}$$

Equation (4.4.3), combined with the complex conjugate of Equation (4.4.4), gives

a matrix equation

$$M \begin{bmatrix} u_+ \\ u_-^* \end{bmatrix} = \begin{bmatrix} i\bar{k} + i\bar{k}_\perp + \lambda & \\ & -i\bar{k} - i\bar{k}_\perp + \lambda \end{bmatrix} \begin{bmatrix} u_+ \\ u_-^* \end{bmatrix}, \tag{4.4.7}$$

where

$$M = i \begin{bmatrix} 2B - C(\rho_0 + A) & B - AC \\ AC - B & C(\rho_0 + A) - 2B \end{bmatrix} \equiv i \begin{bmatrix} X & Y \\ -Y & -X \end{bmatrix}. \tag{4.4.8}$$

A nontrivial solution to this is only possible if

$$\lambda^2 = Y^2 - (X - \bar{k} - \bar{k}_\perp)^2. \tag{4.4.9}$$

Since $\bar{k}$ and $k_\perp^2$ are both positive, they cannot cancel. As long as $\lambda \neq 0$, there will be

both positive and negative solutions for Re λ. The above result for λ^2 factors as

$$\lambda^2 = -(B - C\rho_0 - \bar{k} - \bar{k}_\perp)(3B - C(\rho_0 + 2A) - \bar{k} - \bar{k}_\perp). \tag{4.4.10}$$

Recall that in the previous section, the propagation constant $\bar{k}$ for the plane wave solution was $k_0\overline{\Delta n} = k_0 n_2 |\mathcal{E}_0|^2 + k_0 n_3 |\mathcal{E}_0|^3$. Observe from the definitions of B and C, combined with the steady state result for the value of n_3, that this is also equal to $B - C\rho_0$ for a plane wave solution. Thus we can simplify the result, and present the equation for the eigenvalues in terms of $\bar{k}_\perp$ and Ω. Now we can rewrite

$$\lambda^2 = \bar{k}_\perp[2(B - AC) - \bar{k}_\perp]$$
$$= \bar{k}_\perp(2Y - \bar{k}_\perp) \qquad (4.4.11)$$
$$= 2\,Y(\Omega)\,\bar{k}_\perp - \bar{k}_\perp^2.$$

Note that the quantity T from Section 4.2 is equal to $\bar{k}_\perp$, and $Y(0)$ is equal to V. The form of the growth rate is identical to that in Section 4.2, but with V, which was a real number, replaced by Y, which is in general a complex function of Ω. This implies positive and negative roots, and thus unstable growth, for all frequencies Ω, except where $\lambda = 0$.

Figure 4.2 shows an example of the growth rate $Re(\lambda)$ plotted against $\bar{k}_\perp$ and Ω. Note that the growth rate is everywhere positive, except for $\bar{k}_\perp = 0$ or $\Omega = 0$, since we must choose the positive root of λ^2. We expect zero growth for $\bar{k}_\perp = 0$, since this corresponds to a uniform plane wave intensity correction. Additionally, we have chosen an intensity large enough such that the plane wave solution is stable for $\Omega = 0$. The form of this growth rate is similar to that obtained by Bian et al. [57] for a comparable propagation equation.

To investigate the behavior for large values of $\bar{k}_\perp$, let $Y = Y' + iY''$, and make the
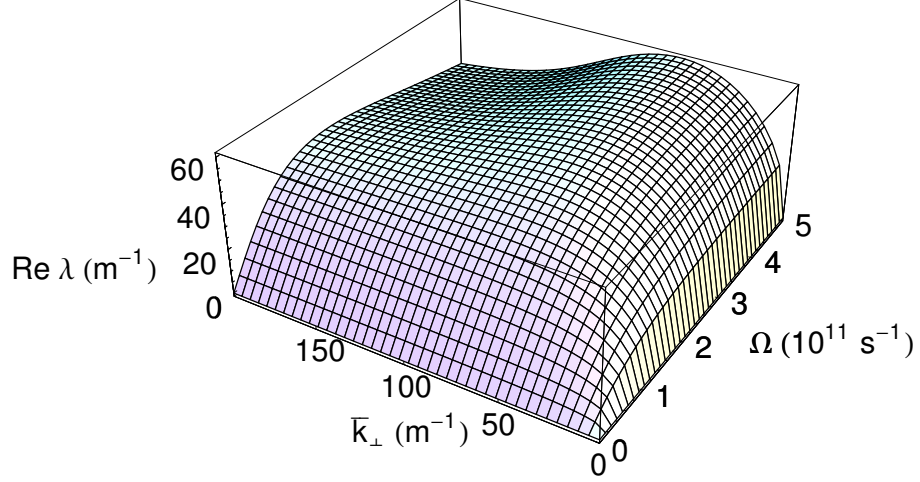
Figure 4.2: Growth rate vs. $\bar{k}_\perp$ and Ω, for intensity 3.2×10^{16} W/m^2.

following approximation:

$$\lambda^2 = \bar{k}_\perp(2Y - \bar{k}_\perp) = \bar{k}_\perp^2 \left(\frac{2Y' + 2iY''}{\bar{k}_\perp} - 1 \right)$$

$$\lambda = \pm i\bar{k}_\perp \left(1 - \frac{2Y'}{\bar{k}_\perp} - \frac{2iY''}{\bar{k}_\perp} \right)^{1/2}$$

$$\approx \pm i\bar{k}_\perp \left(1 - \frac{Y'}{\bar{k}_\perp} - \frac{iY''}{\bar{k}_\perp} \right)$$

$$Re(\lambda) \approx \pm Y'' = \pm Im(Y). \tag{4.4.12}$$

From this, observe that the value of $Re(\lambda)$ approaches $Im(Y)$ as $\bar{k}_\perp \to \infty$. For larger values of Ω, there will be a $\bar{k}_\perp$ corresponding to peak growth rate. However, for small values of Ω, the peak growth rate is at $\bar{k} \to \infty$. The value of $\bar{k}_\perp$ is effectively limited

by its relationship to $k_\perp$, the transverse wave vector, which is assumed to be small compared to k_z in the paraxial approximation. For a grid with $\Delta x = 0.8$ μm, the maximum value of $\bar{k}_\perp$ is approximately 3000 m^{-1}.

4.5   Response for Infinite Temporal Frequency

As $\Omega \to \infty$, the instability growth rate does not die off, nor is there an upper cutoff, as in some cases for modulational instability that only consider self-focusing and GVD [35, 53]. As $\Omega \to \infty$, $Y(\Omega) \to B$, so $\lambda^2 \to \bar{k}_\perp(2B - \bar{k}_\perp)$. This limit is shown in Figure 4.3. For values of $\bar{k}_\perp$ within the unstable range $0 < \bar{k}_\perp < 2B$, the solutions are unstable even as $\Omega \to \infty$. For the 3.2×10^{16} W/m^2 solution used to generate the previous figure for the eigenvalues, the value of $2B$ is 126 m^{-1}.

This result is at first puzzling, but it can be explained by examining what happens to the equations in the stability analysis. If we take $\Omega \to \infty$, we remove all the effects of the stabilizing n_3 or plasma term from the coupled equations, and we are left with the stability of the Kerr medium, which is known to be spatially unstable [54, 34, 45].

We also expect difficulty for any numerical analysis of this instability, since the frequency response to the instability is unbounded. This means that all frequencies present in the numerical model will experience growth, and the growing field will not be bandwidth limited, as is desired for a spectral code. However, we will see in Chapters 5 and 6 that we can still observe the initial behavior of the instability by using a bandwidth-limited noise seed.
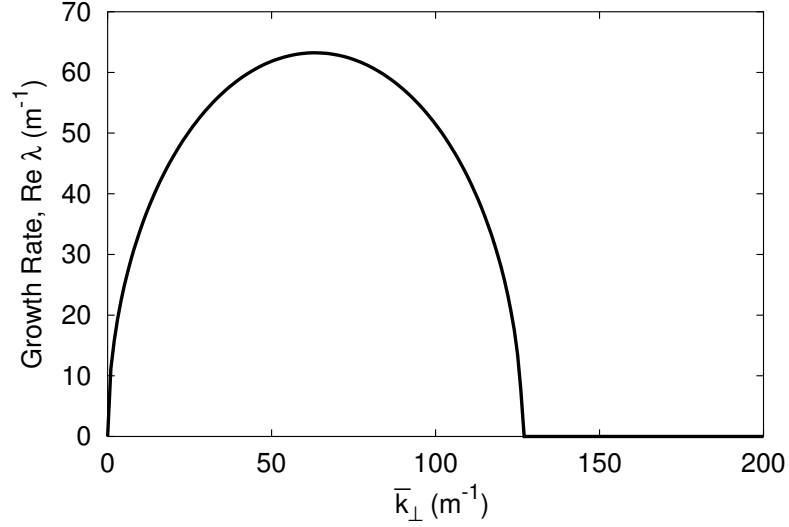
Figure 4.3: Growth rate in the limit of $\Omega \to \infty$, for the $\mathcal{E}_0$ solution with peak intensity 3.2×10^{16} W/m^2.

4.6 Analyzing the Stability of UV Filaments

The analysis so far suggests three ways to approach the stability problem for UV filaments. We have done a plane wave stability analysis, which predicts the growth rate as a function of a single transverse wave vector $\mathbf{k}_\perp$ and temporal perturbation frequency Ω. This analysis predicts unstable growth for all frequencies Ω.

Next, we can solve the equations for the coupled perturbation fields in the linear stability analysis, given by Equations (4.3.10) and (4.3.11). Section 5.3 describes the numerical propagation approach to solve these coupled equations. In this case, we will obtain results for all transverse wave vectors $\mathbf{k}_\perp$ that are represented by the numerical grid, instead of a single transverse wave vector. However, we are still limited to a single temporal frequency Ω. The coupled equations can be solved for an arbitrary

steady state solution $\mathcal{E}_0$. If we use a plane wave solution for $\mathcal{E}_0$, we obtain a way to verify this propagation scheme against the plane wave analysis.

Finally, we can model the full three dimensional propagation, by including the time dimension of a pulse as the third transverse dimension in the split-operator propagation, which will be described in Section 5.4. This will allow observation of unstable growth for all frequencies Ω and $\mathbf{k}_\perp$ that we can numerically represent.

Chapter 5 presents details of the numerical approach taken to propagating the wave equation for the single and uncoupled 2D field case, as well as the full 3D case. Chapter 6 presents the results of these computations. For consistency, throughout the stability results, we will use the steady state solution $\mathcal{E}_0$ that corresponds to a peak intensity of 3.2×10^{16} W/m^2. This solution has roughly 470 MW of power.

We choose this solution because, as discussed above, in the plane wave analysis, its intensity is above the cutoff described in Section 4.2, and thus it is theoretically stable for all $\mathbf{k}_\perp$ at $\Omega = 0$, unlike the 200 MW solution. We will find, however, that the general conclusion—that the long pulses suffer from modulational instability, does not depend on the specific power chosen.

CHAPTER 5

NUMERICAL MODEL

5.1   Introduction

In Chapter 3, we discussed 2D propagation results that verify the form of the predicted oscillatory beam solutions for the case of time-independent beam propagation. To study the stability results from Chapter 4, we need to run the coupled 2D and full 3D propagations described in Section 4.6. This chapter discusses how these numerical propagations are prepared and performed in each case, and some of the pertinent numerical issues.

The propagation code is written in Fortran 90, and uses the OpenGL graphics library to provide real time 3D graphics feedback as the propagation runs. There are three different choices for the form of the field to be propagated. All three choices use the split-operator method of propagation, which is detailed in Appendix B. The first choice uses a single 2D spatial field, on a grid with two space dimensions, which we call an XY grid. This models a CW beam with an arbitrary spatial profile, and is used to produce the results in Chapter 3. The second option propagates two coupled 2D fields with the same XY grid, and is used to evolve the two perturbation fields in the stability analysis. The third option defines a 3D field over a grid with two space dimensions and one time dimension (labeled XYT). Full 3D simulations are run using either the case of periodic boundary conditions in time, or a pulse of finite length. The temporal periodic boundary condition case is intended to model a section of a

long pulse or CW beam. In this scenario, we are interested in the initial growth of the modulational instability over a section of the pulse. In the finite duration pulse case, we examine the combined effects of everything in the model, including the instability, losses, and pulse edge effects.

5.2 Propagating a Single 2D Field

The single 2D field code solves the problem of CW propagation of the equation

$$\frac{\partial \mathcal{E}}{\partial z} = \frac{i}{2k}\nabla_\perp^2 \mathcal{E} + ik_0 n_2 |\mathcal{E}|^2 \mathcal{E} + ik_0 n_3 |\mathcal{E}|^3 \mathcal{E} + ik_0 n_4 |\mathcal{E}|^4 \mathcal{E}$$
$$- \frac{\beta^{(K)}}{2}|\mathcal{E}|^{2K-2}\mathcal{E} - \frac{\sigma}{2}(1 + i\omega\tau)\rho\mathcal{E}. \quad (5.2.1)$$

The n_3 and n_4 terms are present for testing and generality. By using the n_3 term the plasma density ρ can be set to zero, and that term ignored, resulting in a simpler calculation, if we are working under the approximation that the plasma acts as an effective n_3 term. Alternatively, if we wish to use a different plasma model we can use the plasma term and set n_3 to zero. The plasma evolution equation is

$$\frac{\partial \rho}{\partial t} = b|\mathcal{E}|^{2K} - a\rho^2 + c\rho|\mathcal{E}|^2, \quad (5.2.2)$$

where $b \equiv \beta^{(K)}/K\hbar\omega$. The third term, which describes avalanche ionization, did not significantly affect the results when included. This agrees with the Schwarz-Diels prediction that its importance is small for sufficiently short pulses.

The initial condition for the single 2D field case is a Gaussian beam. This field

$\mathcal{E}_{in}$ is defined on a rectangular grid. The user specifies the grid spacings Δx and Δy and the number of points in each direction N_x and N_y. In practice, we always use a square grid ($N_x = N_y$, $\Delta x = \Delta y$). The initial beam is characterized by its width, and either the maximum intensity or total beam power. The equation for the beam is

$$\mathcal{E}_{in}(x, y) = \mathcal{E}_0 \exp(-(x^2 + y^2)/w_0^2). \tag{5.2.3}$$

The beam is initially defined with no curvature, so it is at a waist. From the definition in Schwarz and Diels [17], for a Gaussian beam profile $I = I_0 \exp(-2r^2/w^2)$, the beam power is $P = \pi w^2 I_0 / 2$. Thus if we choose to characterize the beam by its power, the initial value of $\mathcal{E}_0$ is chosen by setting

$$\mathcal{E}_0 = \sqrt{I_0} = \sqrt{\frac{2P}{\pi w_0^2}}. \tag{5.2.4}$$

By defining $\mathcal{E}_0$ in this manner, we use intensity units, which is consistent with the treatment in Chapter 2 and Appendix A. The code stores the field amplitude $\mathcal{E}$ as a quantity relative to the initial peak value of $\mathcal{E}_0$. The initial peak intensity is then used as a normalization factor to compute the field intensity $|\mathcal{E}|^2$ when needed.

The details of the split-operator method, which is used to propagate the field, can be found in Appendix B. In addition, we use absorbing boundary conditions (ABC) for the edges of the numerical grid. This helps prevent spurious contributions from field energy "wrapping around" the edges of the grid, due to the periodic nature of the Fourier transform. The absorbing boundary conditions take the form of a loss term in the potential, described by a Gaussian centered at the edges of the grid, so

that the absorption is smooth. However, the conditions are not perfect, and there is always a small amount of energy that reflects from them, which can crop up in long distance propagations.

5.3 Evolving Coupled Perturbation Fields

For the case of the linear perturbation analysis, we need to solve the coupled equations from Section 4.3:

$$\frac{\partial \mathcal{E}_+}{\partial z} = \frac{i}{2k}\nabla_\perp^2 \mathcal{E}_+ + ik_0 n_2 \left[2|\mathcal{E}_0|^2 \mathcal{E}_+ + \mathcal{E}_0^2 \mathcal{E}_-^*\right]$$
$$- i\frac{\sigma\omega\tau}{2}\left(\rho_0 \mathcal{E}_+ + \frac{Kb|\mathcal{E}_0|^{2K-2}}{2a\rho_0 - i\Omega}\left[|\mathcal{E}_0|^2 \mathcal{E}_+ + \mathcal{E}_0^2 \mathcal{E}_-^*\right]\right), \quad (5.3.1)$$

$$\frac{\partial \mathcal{E}_-^*}{\partial z} = -\frac{i}{2k}\nabla_\perp^2 \mathcal{E}_-^* - ik_0 n_2 \left[2|\mathcal{E}_0|^2 \mathcal{E}_-^* + \mathcal{E}_0^2 \mathcal{E}_+\right]$$
$$+ i\frac{\sigma\omega\tau}{2}\left(\rho_0 \mathcal{E}_-^* + \frac{Kb|\mathcal{E}_0|^{2K-2}}{2a\rho_0 - i\Omega}\left[|\mathcal{E}_0|^2 \mathcal{E}_-^* + \mathcal{E}_0^2 \mathcal{E}_+\right]\right). \quad (5.3.2)$$

for $\mathcal{E}_+(x, y, z)$ and $\mathcal{E}_-^*(x, y, z)$. These two fields represent perturbation amplitudes for a possible modulational instability of the "steady state" field $\mathcal{E}_0$, at temporal frequency Ω. The plane wave analysis gives an idea of the growth rate as a function of Ω and the transverse wave vector $k_\perp$, but with these equations we hope to observe the spatial dependence of the perturbation, for one particular frequency Ω.

The same basic split-operator approach from Appendix B is used for the coupled equations. We will define $\hat{T}$ and $\hat{V}$ to be matrix operators obtained from the coupled

equations. However, we make one simplification first. Note that the value $\mathcal{E}_0^2$ is present in the growth equations for the perturbation fields. We know that $\mathcal{E}_0$ has the form $u(r)\exp(i\bar{k}z)$, where $\bar{k}$ is the eigenvalue of the steady state problem. In the terms with $|\mathcal{E}_0|^2$, the phase factor is no longer present, but it still appears in the $\mathcal{E}_0^2$ terms. As we did in the linear perturbation analysis, we modify the form of the fields to include the $\bar{k}$ dependence: Let

$$\mathcal{E}_+(r,z) = u_+(r,z)e^{i\bar{k}z} \qquad \mathcal{E}_-(r,z) = u_-(r,z)e^{i\bar{k}z}. \qquad (5.3.3)$$

When we substitute the new fields into the growth equations, the phase from $\mathcal{E}_0^2$ is cancelled by the phase from $\mathcal{E}_-^*$, and we cancel an overall phase $\exp(i\bar{k}z)$. We are only left with terms involving $|\mathcal{E}_0|^2$, which will simplify the numerical evaluation. There is also a new term $i\bar{k}u_+$, which comes from the z derivative.

$$\frac{\partial u_+}{\partial z} = -i\bar{k}u_+ + \frac{i}{2k}\nabla_\perp^2 u_+ + iB\left[2u_+ + u_-^*\right] - iC\left(\rho_0 u_+ + A\left[u_+ + u_-^*\right]\right), \qquad (5.3.4)$$

$$\frac{\partial u_-^*}{\partial z} = i\bar{k}u_-^* - \frac{i}{2k}\nabla_\perp^2 u_-^* - iB\left[u_+ + 2u_-^*\right] + iC\left(\rho_0 u_-^* + A\left[u_+ + u_-^*\right]\right). \qquad (5.3.5)$$

where A, B, and C are defined as in Equation (4.4.8). Thus the evolution of

$$U \equiv \begin{bmatrix} u_+ \\ u_-^* \end{bmatrix} \qquad (5.3.6)$$

is given by

$$\frac{\partial U}{\partial z} = i\hat{T}U + i\hat{V}U, \qquad (5.3.7)$$

where

$$\hat{T} = \begin{bmatrix} \nabla_\perp^2/2k & \\ & -\nabla_\perp^2/2k \end{bmatrix}, \tag{5.3.8}$$

and

$$\hat{V} = \begin{bmatrix} 2B - C(\rho_0 + A) - \bar{k} & B - AC \\ -(B - AC) & -(2B - C(\rho_0 + A) - \bar{k}) \end{bmatrix} \equiv \begin{bmatrix} X & Y \\ -Y & -X \end{bmatrix}. \tag{5.3.9}$$

Here we have modified the definition of X to be $2B - C(\rho_0 + A) - \bar{k}$. In the code, the fields u_+ and u_- are stored in a 3D array with size 2 along the third dimension. To apply the $\exp(i\hat{T}\Delta z/2)$ term, we transform to the spectral representation, multiply the u_+ component by the precomputed linear propagator array, and multiply $u_{-}*$ by the complex conjugate of the linear propagator array. The linear propagator array is the same as that for the case of the single 2D field in Appendix B. This is possible because the $\hat{T}$ term is diagonal in the spectral representation of the $\{u_+, u_-^*\}$ space that we defined.

However, the $\exp(i\hat{V}\Delta z)$ term is not diagonal with respect to $\{u_+, u_-^*\}$. The matrix $\hat{V}$ is not Hermitian, so we cannot use a unitary basis transformation approach. Instead, we directly compute the matrix exponential, using the spatial representation for the fields. This is done for every point in the (x, y) grid; note that X and Y depend on the coordinates x and y through $\mathcal{E}_0$. Additionally, X depends on Ω, the temporal frequency of the perturbation. Fortunately, we only need to compute this matrix exponential once, before the propagation begins, since it does not change; this

is another advantage of factoring the $\bar{k}$ dependence out of the perturbation fields.

To compute the matrix exponentials, we use a result derived with *Mathematica*. The special form of the matrix makes the result simpler than the general case of a 2×2 matrix exponential. If

$$m = \begin{bmatrix} a & b \\ -b & -a \end{bmatrix}, \tag{5.3.10}$$

then

$$\exp(m) = \begin{bmatrix} \frac{1}{2s}[(a+s)e^s - (a-s)e^{-s}] & \frac{b}{2s}(e^s - e^{-s}) \\ -\frac{b}{2s}(e^s - e^{-s}) & \frac{1}{2s}[(a+s)e^{-s} - (a-s)e^s] \end{bmatrix}. \tag{5.3.11}$$

Here $s \equiv \sqrt{a^2 - b^2}$. To obtain the result we need, we let $a \equiv iX\Delta z$, $b \equiv iY\Delta z$. We then store this 2×2 matrix exponential at every spatial grid point. During the split-operator propagation, the action of $\exp(i\hat{V}\Delta z)$ is obtained by matrix multiplication for every point on the spatial grid.

To perform the propagation, we need to know the value of the the propagation constant $\bar{k}$ for a given solution $\mathcal{E}_0$. We can use the definition of the steady state field to get a numerical value for $\bar{k}$. We know that

$$\frac{\partial \mathcal{E}_0}{\partial z} = i\bar{k}\mathcal{E}_0 = \mathcal{G}\mathcal{E}_0, \tag{5.3.12}$$

where $\mathcal{G}$ is the evolution operator $\mathcal{G} = i\nabla_\perp^2/2k + ik_0 n_2 |\mathcal{E}|^2 + \cdots$. Multiply both sides

of the equation by $\mathcal{E}_0^*$ and integrate to find

$$i\bar{k} \int |\mathcal{E}_0|^2 = \int (\mathcal{G}\mathcal{E}_0)\mathcal{E}_0^*. \tag{5.3.13}$$

We can evaluate both integrals numerically, and thus find the value of $\bar{k}$ from the field itself. This provides a numerical check for the value of $\bar{k}$, since it can be compared to the value that was used to numerically generate the solution for $\mathcal{E}_0$ in Section 3.4.

The initial condition for the 2D coupled case is to set $\mathcal{E}_+$ and $\mathcal{E}_-^*$ to fields of random noise. The spatial noise field is defined as

$$\mathcal{E}_+ = N_0(1 + R\mathcal{A}), \tag{5.3.14}$$

where $\mathcal{A}$ is a uniform complex random value with real and imaginary parts between $+1$ and -1, and N_0 and R are amplitudes. The same process is used to generate $\mathcal{E}_-$. We apply a hyperbolic tangent window to the spatial noise field, then Fourier transform the noise to apply a similar spectral window. The spectral window should be relatively smooth, so that sharp edges do not contribute to any sharp structures in the field, thereby inducing numerical instability.

When the program is run, we watch for a shape to grow out of the noise. The program keeps track of the maximum amplitude of the perturbation field, and plots it on a log scale plot. Once the shape has settled down, this log plot approaches a

line, and the code estimates the slope of the line, which is the growth rate $Re(\lambda)$:

$$|\mathcal{E}_+| \propto \exp(Re(\lambda)z) \tag{5.3.15}$$

$$\log|\mathcal{E}_+| = \text{const} + Re(\lambda)z. \tag{5.3.16}$$

To test the validity of the coupled perturbation code, we try solving the coupled equations for the case of a plane wave $\mathcal{E}_0$ as well as a plane wave seed. Using a plane wave $\mathcal{E}_0$ means that $|\mathcal{E}_0|^2$ is effectively a constant over the field. The plane wave seed confines the initial perturbation to one value of $\bar{k}_\perp$. The growth rate obtained numerically in the code matched the growth rate $Re[\lambda(\Omega, \bar{k}_\perp)]$ predicted by the plane wave analysis in Section 4.3 to within a few percent, for several test values of Ω and $\bar{k}_\perp$. We included the case of $\Omega = 0$ for intensities both above and below the stability cutoff in Section 4.2. This confirmed that the coupled field code correctly modeled the plane wave limit.

5.4   Propagating the Full 3D Field

For the case of the 3D XYT field, we need to solve the equations

$$\frac{\partial\mathcal{E}}{\partial z} = \frac{i}{2k}\nabla_\perp^2\mathcal{E} + ik_0n_2|\mathcal{E}|^2\mathcal{E} - \frac{\beta^{(K)}}{2}|\mathcal{E}|^{2K-2}\mathcal{E} - \frac{\sigma}{2}(1 + i\omega\tau)\rho\mathcal{E}. \tag{5.4.1}$$

$$\frac{\partial\rho}{\partial t} = b|\mathcal{E}|^{2K} - a\rho^2, \tag{5.4.2}$$

where $\mathcal{E} = \mathcal{E}(x, y, z, t)$ and $\rho = \rho(x, y, z, t)$. We proceed in the same manner as for the 2D XY case, except that now we need to calculate the plasma density by solving

the differential equation, instead of using an effective n_3 or the quadratic solution for the steady state plasma.

We use the split-operator approach with

$$\hat{T} = \frac{\nabla_\perp^2}{2k_0}, \tag{5.4.3}$$

$$\hat{V} = k_0 n_2 |\mathcal{E}|^2 - \frac{\beta^{(K)}}{2} |\mathcal{E}|^{2K-2} - \frac{\sigma}{2}(1 + i\omega\tau)\rho. \tag{5.4.4}$$

The field $\mathcal{E}$ is Fourier transformed to spectral space, where half of the $\hat{T}$ operator is applied, then Fourier transformed back to real space, where the $\hat{V}$ nonlinear index change and loss terms, as well as any spatial absorbing boundary conditions, are applied. Finally, we transform to spectral space for the second half of the linear propagator. The $\hat{T}$ operator contains no time dependence, so it is independent of time slice in the full grid, and it is applied in parallel to the different time slices.

To compute the plasma density at a given z position, we numerically integrate the plasma equation. One approach is to use a modified Euler method:

$$\rho'_{n+1} = \rho_n + \Delta t\, b|\mathcal{E}|^{2K} \tag{5.4.5}$$

$$\rho_{n+1} = \frac{\rho'_{n+1}}{1 + a\Delta t\rho'_{n+1}}. \tag{5.4.6}$$

However, this sequence does not converge to the steady state value

$$\rho = \sqrt{b/a}|\mathcal{E}|^K, \tag{5.4.7}$$

unless the product $ab\,|\mathcal{E}|^{2K}\Delta t^2 << 1$. This effect was observed when we started with the numerically constructed $\mathcal{E}_0$ solution from Section 3.4. The plasma generated by this method was roughly one-third of what it should have been, for $\Delta t = 3 \times 10^{-11}$ seconds. To obtain an accurate value for the generated plasma within a few percent requires $\Delta t = 3 \times 10^{-13}$ seconds. Alternatively, one could try the sequence

$$\rho_{n+1} = \frac{\rho_n + \Delta t\, b|\mathcal{E}|^{2K}}{1 + a\Delta t \rho_n}. \tag{5.4.8}$$

This converges to the correct value. This may also be generalized to include the case of avalanche ionization, though in the computations presented here, we neglect avalanche ionization. It remains to be tested whether larger time steps can be used with this method. One might also consider higher order, but explicit, numerical methods.

The code uses a third method, based on the exact solution to the differential equation describing the plasma. This exact solution applies to the case where the source term is constant in time, that is, $|\mathcal{E}|^2$ is constant in time. The exact solution is then combined with a piecewise constant approximation for the field. For each step let the source term be constant over the duration of the step. Here we will change notation, and temporarily redefine $b \equiv b|\mathcal{E}|^{2K}$ for simplicity. The equation

$$\frac{\partial \rho}{\partial t} = b - a\rho^2 \tag{5.4.9}$$

has the exact solution

$$\rho(t) = \sqrt{\frac{b}{a}} \tanh[\sqrt{ab}(t - t_0)], \tag{5.4.10}$$

where t_0 is a constant of integration. Define $\rho_0 \equiv \sqrt{b/a}$; this is the steady state plasma density. If we impose the condition that $\rho(t_n) = \rho_n$, we find that

$$\rho(t_{n+1}) = \rho_0 \tanh\left[\sqrt{ab}\,(t_{n+1} - t_n) + \tanh^{-1}\left(\frac{\rho_n}{\rho_0}\right)\right]. \tag{5.4.11}$$

This scheme presents difficulty if $\rho_n > \rho_0$ for some n during the iterated solution, since the $\tanh^{-1}$ function then becomes complex. However, we can use an identity to expand this expression:

$$\tanh(\tanh^{-1} x + \tanh^{-1} y) = \frac{x + y}{1 + xy}. \tag{5.4.12}$$

Then define $\Delta t = t_{n+1} - t_n$. We have

$$\rho(t_{n+1}) = \rho_0 \tanh\left[\tanh^{-1}\left(\tanh\sqrt{ab}\,\Delta t\right) + \tanh^{-1}\left(\frac{\rho_n}{\rho_0}\right)\right], \tag{5.4.13}$$

$$= \rho_{n+1} = \rho_0 \frac{\tanh\left(\sqrt{ab}\,\Delta t\right) + \rho_n/\rho_0}{1 + \tanh\left(\sqrt{ab}\,\Delta t\right)\rho_n/\rho_0}. \tag{5.4.14}$$

This approach removes the need to use any inverse hyperbolic tangents, and allows the perturbed ρ_n to be larger than ρ_0.

Given the above scheme to compute the plasma density, we then solve it for

each value of x and y over time. For this reason this portion of the code is easily made parallel, since there is no interaction, such as diffusion, between the plasma for different values of x and y. If the pulse is confined in time, so that the field is zero at the boundaries, then we solve the equation from the low boundary of the time grid to the high boundary. However, if we are running the temporal periodic boundary conditions case, we iterate the solution, wrapping back around the time boundary several times, to ensure that the plasma is continuous over the boundary. In practice, three or four iterations are sufficient to verify this.

For the case of periodic boundary conditions in time, the initial condition is constructed by first loading in the numerically generated $\mathcal{E}_0$ spatial profile described earlier. Each time slice in the full XYT array is initialized with this profile. Random multiplicative amplitude noise is then added to this full field. Finally the noise is filtered in the frequency domain, both spatially and temporally. The upper limit for the temporal noise frequency is given as an input parameter. It is important to ensure that this upper limit is an absolute value and does not depend on the grid spacing, or frequency grid size. Otherwise, the observed growth will depend on these grid parameters. This is due to the presence of unstable growth for all frequencies Ω.

5.5 Numerical Considerations and Diagnostics

For the case of XY propagation, one quantity that is measured for each step is an estimate of the beam width. This can be done with a second moment technique as follows: Take a 1D slice of the beam through the origin. Define the width of the

Gaussian by w in the expression $g(x) = \exp(-x^2/w^2)$. For this form of $g(x)$,

$$\frac{\int_{-\infty}^{\infty} x^2 g(x)^2}{\int_{-\infty}^{\infty} g(x)^2} = \frac{w^2}{4} \tag{5.5.1}$$

$$w = 2\sqrt{\frac{\int x^2 g(x)^2}{\int g(x)^2}} \ . \tag{5.5.2}$$

Both of these integrals are easily performed as numerical summations, and the width estimate w is updated for each step of the propagation. The code also updates the user with the peak field intensity, and an update of the what the width would be for a Gaussian beam propagation under diffraction only.

Diagnostic tests for the 3D propagation case included initializing the spatial field with the numerically constructed eigensolution of the propagation, and starting with a perfectly flat temporal profile. For this we imposed periodic boundary conditions in time. When this is run, we observe that its amplitude remains stationary, at least for the initial few meters, before tiny numerical errors begin to seed unstable growth.

Another general test for the 3D code involves using only n_2 and n_3 nonlinearities rather than modeling the plasma. This results in the beam or pulse being uncoupled in time, since all the time slices act independently, but gives a test that can be compared to the 2D code.

The grid spacings are chosen to minimize computational effort while best representing the numerical fields. During the testing and generation of results for 2D and 3D propagation, the results were verified for different values of Δx, Δt, and Δz to check the convergence. Section B.2 in Appendix B discusses the relationship between the grid spacings and propagation step when using a split-operator method. Table 5.1

provides the parameters for the numerical grids used in most of the simulations in

this work.

Table 5.1: Typical numerical grid parameters. Those used to generate the results in this dissertation are given in bold.

Parameter	Name	Value	Units
Number of X or Y points	N_x, N_y	**128** or 256	—
Number of T points	N_t	128 - 1024	—
X or Y spacing	$\Delta x, \Delta y$	5.0, **8.0** ,10.0	μm
Z step	Δz	**0.5**, 1.0	mm
Time spacing	Δt	0.5, **1**, 2	10^{-12} s

CHAPTER 6

NUMERICAL RESULTS

6.1   Coupled Perturbation Fields

This chapter presents the numerical results of the latter two methods outlined in Section 4.6: the coupled field propagation, and the full 3D propagations. We first examine the results for the propagation of the coupled perturbation fields $\mathcal{E}_+$ and $\mathcal{E}_-$ described in the linear analysis in Section 4.3. The coupled field propagation requires less computational effort than full 3D propagation, since it involves 2D fields. The results tell us about the shape and growth rate of the perturbation fields. However, the trade-off is that these results are linear approximations, and we must choose one particular temporal frequency Ω for which we investigate the instability. We seed the perturbation fields with random noise, and propagate them using the method described in Section 5.3.

We must choose the steady state field $\mathcal{E}_0$ as an input for the computation. This is done by using the computed exact steady state solution from Section 3.4 corresponding to the given peak intensity or beam power of interest. Alternatively, we can choose $\mathcal{E}_0$ to be a plane wave with a specific intensity, for a verification of the coupled field propagation code, discussed in Chapter 5. In this case, the perturbation field is initialized with a single value of $\mathbf{k}_\perp$.

For the case of using a steady state beam solution $\mathcal{E}_0$, the results indicate a growing instability for all frequencies $\Omega > 0$, as predicted. The growth rates do

not exactly correspond to the plane wave prediction, because the $\mathcal{E}_0$ beam solution

contains a combination of plane waves with differing $\bar{k}_\perp$ values. The intensities of these

plane wave components are lower than the peak intensity of the beam solution; lower

intensities tend to correspond to lower growth rates. Depending on the frequency

Ω that is considered, as well as the power of the steady state solution, the growing

instability fields take different shapes. We discuss the results here for $\Omega = 0, 10^{11}$,

and 10^{12} s^{-1}. We use the steady state solution $\mathcal{E}_0$ computed in Section 3.4 with a

peak intensity of 3.2×10^{16} W/m^2, corresponding to a power of roughly 470 MW.

For $\Omega = 0$, one might not expect any instability growth, since we chose the peak

intensity of the steady state solution to be above the stability cutoff in Section 4.2.

However, an unstable mode still grows for $\Omega = 0$, no matter how carefully we choose

the steady state solution or adjust the grid sizes or spacings. The unstable mode was

circularly symmetric, with a growth rate λ on the order of 10^{-2} m^{-1}. The explanation

for this unstable growth is that the solution for $\mathcal{E}_0$ is composed of plane waves that

can have a lower intensity than the cutoff. Thus a small portion of the field seeds

growth at $\Omega = 0$.

Since the original stability analysis is linear, there is no dependence on amplitude,

and the mode will grow without bound as the coupled fields evolve. This is true for

all frequencies Ω; the perturbation fields grow to magnitudes well beyond the validity

of the small perturbation approximation. However, this approach provides a tool to

discern the shape of the most unstable mode, as this mode will grow fastest, and

eventually dominate, as the fields propagate.

Figure 6.1 shows the form of the perturbation fields for $\Omega = 10^{11}$ s^{-1}, and the exact

steady state $\mathcal{E}_0$ field with peak intensity 3.2×10^{16} W/m^2, which is our standard solution. Figures 6.1(a) and 6.1(b) show the absolute value and real part of the growing perturbation field $\mathcal{E}_+$. The field $\mathcal{E}_-$ has a nearly identical shape and is not shown. The fields take the form of two lobes; When they initially develop, the two lobes may not have the same height, depending on the initial noise seed. However, as this strongest mode grows, the two lobes become symmetrical. The early asymmetry is due to the presence of other, slower growing modes, from the initial noise seed. However, the shape of the fastest growing mode eventually dominates. Since there is azimuthal symmetry in the propagation equations, the choice of orientation of the two lobes is determined by the initial conditions. The rough textured background in these figures is the initial noise seed. These figures show the growing solution at $z = 0.78$ m.

Figure 6.1(c) shows the combination $\mathcal{E}_0 + \mathcal{E}_+ + \mathcal{E}_-$. At this distance, $\mathcal{E}_+$ still has a somewhat smaller magnitude than $\mathcal{E}_0$. As mentioned, the perturbation will grow without bound, but we can perform this example summation while the magnitudes are comparable. Note that we have arbitrarily chosen a time origin $t = 0$ such that the full equation for the field plus perturbation, Equation (4.3.4), gives just the sum of the fields. As the perturbation evolves, the absolute value approaches a fixed shape, but the real and imaginary parts continuously change phase. This makes the beam become lopsided, and oscillate in the manner of a "snake" instability. After the initial growth of the strongest unstable mode from the noise, the growth rate of the perturbation fields is exponential. The growth rate for this nontrivial $\mathcal{E}_0$ at $\Omega = 10^{11}$ s^{-1} is approximately 13 m^{-1}, which, as discussed and seen from Figure 4.2

is lower than the general neighborhood of linear growth rates, given this value of Ω. The peak plane wave growth rate for $\Omega = 10^{11}$ s^{-1} is roughly 35 m^{-1}.

Figure 6.2 shows the form of the perturbation fields for the case of $\Omega = 10^{12}$ s^{-1}. For this frequency, the growing field initially appeared to have the two-lobe structure that was observed for $\Omega = 10^{11}$ s^{-1}. However, as the field is propagated, the structure changes into the symmetrical form shown in the figures. Thus for $\Omega = 10^{12}$ s^{-1}, the growth rate for the symmetric mode is faster than the rate for the asymmetric mode. This growth rate is approximately 40 m^{-1}, while the peak plane wave growth rate for this frequency is roughly 60 m^{-1},

For lower frequencies, the shape of the perturbation appears to be a two-lobed structure, while for higher frequencies, the shape of the perturbation begins as a two-lobed structure, but then evolves into a circularly symmetric form. In both cases the initial form shows some asymmetry, as a combination of modes of varying growth rates develops. The asymmetric structure at low Ω leads to a "snake" instability, while the symmetric structure at higher Ω causes a "neck" instability. The cutoff value where the mode shape changes from two lobes to azimuthally symmetric is not known exactly, but will depend on the peak intensity that defines the zero order solution.
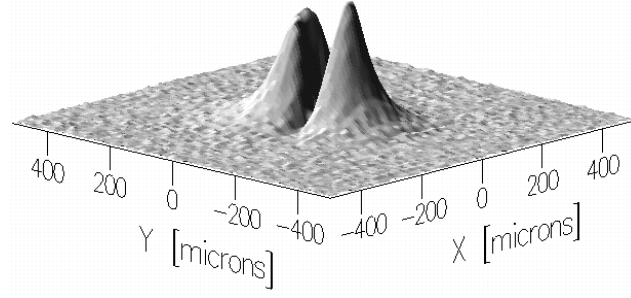
(a) Absolute value of $\mathcal{E}_+$
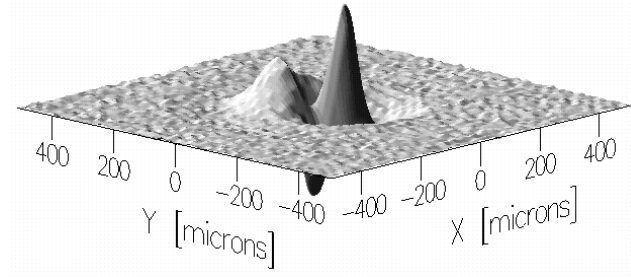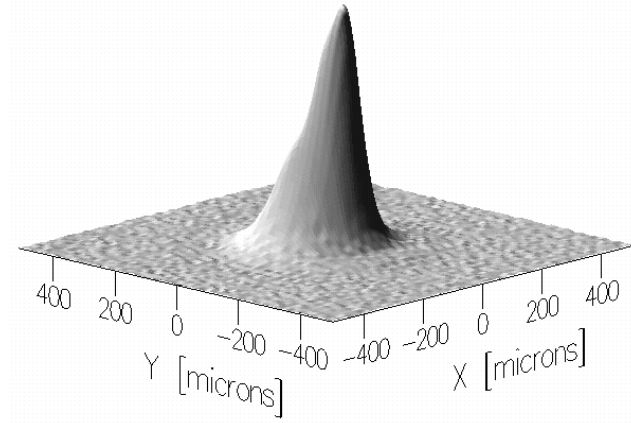
(b) Real part of $\mathcal{E}_+$

(c) Absolute value of $\mathcal{E}_0 + \mathcal{E}_+ + \mathcal{E}_-$

Figure 6.1: Coupled perturbation fields for $\Omega = 10^{11}$ s^{-1}. In (a) and (b) the absolute value and real part of $\mathcal{E}_+$ are shown. Part (c) shows an example of combining $\mathcal{E}_+ + \mathcal{E}_-$ with $\mathcal{E}_0$, which results in a lopsided beam. Here the noise seed is visible as the rough texture of the background in the figures.
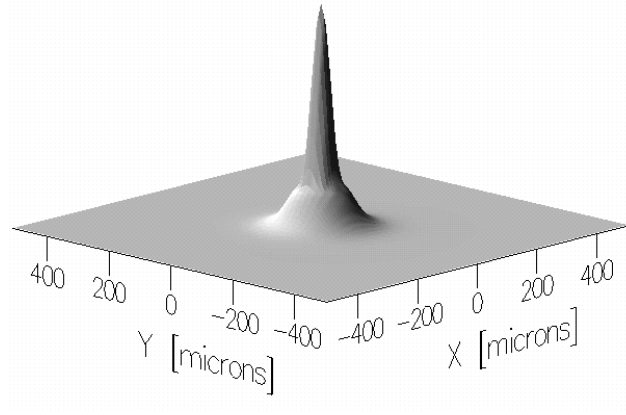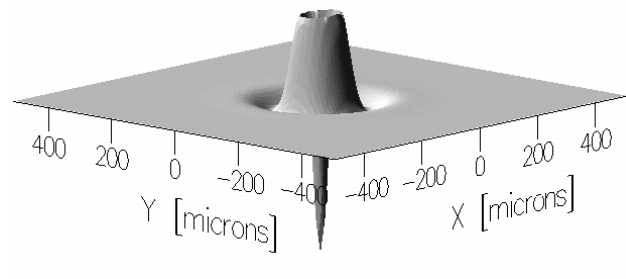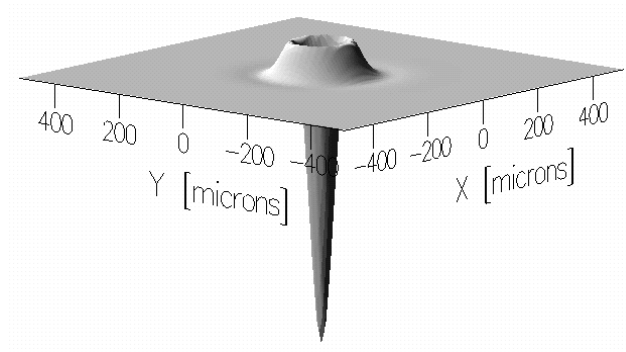
(a) Absolute value of $\mathcal{E}_+$

(b) Real part of $\mathcal{E}_+$

(c) Imaginary part of $\mathcal{E}_+$

Figure 6.2: Coupled perturbation field for $\Omega = 10^{12}$ s^{-1}. At this frequency, the fields are circularly symmetric. Here the fields have been evolved for several meters and have grown far beyond the noise seed.

6.2   Periodic Boundary Conditions in Time

We now turn to the case in which the time domain is fully resolved, and we use the three dimensional propagator. For the first study of full three dimensional results, we propagate using periodic boundary conditions in time, using the method described in Section 5.4. This allows investigation of the stability of the central region of a hypothetical long pulse, without needing to resolve or consider any transient effects based on the pulse edges. We initialize the temporal profile as flat, but possibly with some small modulation or random noise. We can initialize the spatial profile to a steady state solution or a Gaussian beam. Additionally, we can introduce random noise over the full 3D spatiotemporal grid.

The effect of noise depends on the bandwidth of the noise seed. Recall that the stability analysis in Chapter 4 indicates that unstable modes are expected to grow for all temporal frequencies. Thus, if the noise seed contains all available frequency components, the noise will grow for all frequencies allowable on the grid. If the noise is spectrally limited to lower frequency components, the spectrum of the growing noise will be approximately cut off at this limit; however, higher frequency components eventually appear, due to the coupling between space and time in the plasma response.

As an example, we initialize the field with the steady state solution for $\mathcal{E}_0$ shown in Figure 3.6, with peak intensity 3.2×10^{16} W/m^2. The noise is set to be random noise with 1 percent amplitude, bandwidth limited to $|\Omega| < 10^{12}$ s^{-1} and $k_\perp < 2 \times 10^5$ m^{-1}. The results of the propagation for three different distances are shown in Figure 6.3. The subfigures show plots of the absolute value of the field amplitude taken in cross

section, for the central ($y = 0$) two dimensional slice of the full three dimensional field. The initial condition and early evolution are not shown, as the amplitude of the noise is initially too small to see. Figure 6.4 shows the spectral representation of the state reached in Figure 6.3(b). The central peak of the spectral representation, which is the zero frequency component, has been cropped in the figure, to show the spectrum of the growing perturbations. The spectrum grows strongly within the region bounded by $|\Omega| < 2 \times 10^{12}$ s^{-1}. This value was the upper limit for the temporal frequencies present in the noise seed. Both symmetric and antisymmetric (neck and snake) modulations are observed.

As mentioned, a problem with simulating the growth of unstable modes on the full 3D grid is that we can never represent all the temporal frequencies involved, since, as seen in Section 4.5, the growth rate is positive for all frequencies. We can only demonstrate the growth for a limited range of frequencies. Additionally, as the field evolves, the noise grows until it becomes so strong that it exceeds the numerical capabilities of a grid; the time or length scales of the features of the noise peaks can approach the grid spacing in space or time. However, this analysis provides a useful look at the initial growth of a modulational instability. For the UV filaments studied here, it is apparent from these results that the fundamental steady state solution suffers from the instability and will fragment in time. Thus, for a pulse with finite duration, we expect that the transient leading edge of the pulse will not be able to converge to the steady state solution that represents the central flat temporal region of the pulse in the Schwarz-Diels model. We model such a pulse in the next section.
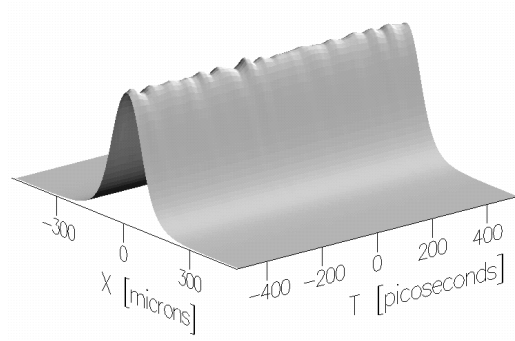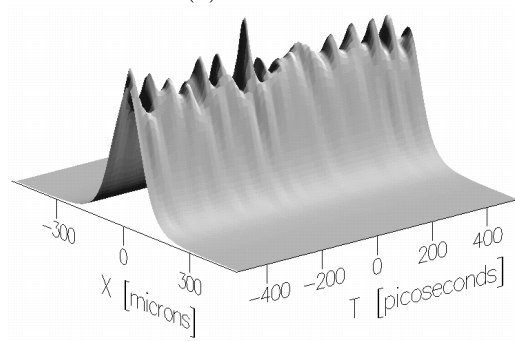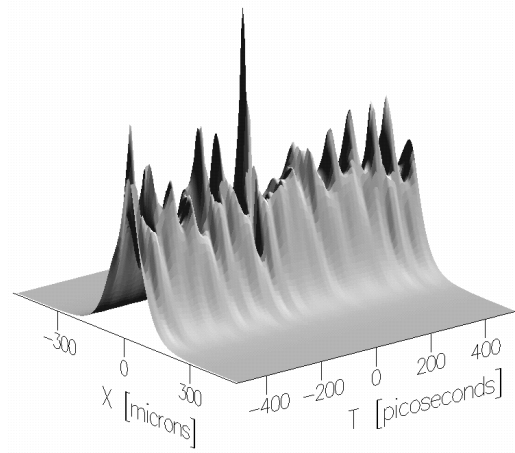
(a) z = 10 cm

(b) z = 15 cm

(c) z = 17.5 cm

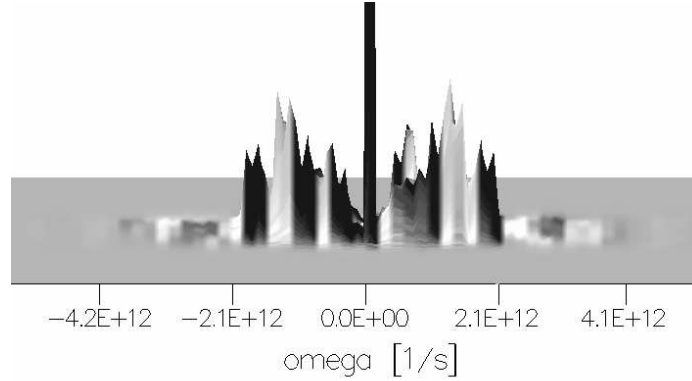Figure 6.3:   Growth of instability for periodic boundary conditions in time.

Figure 6.4: Growth of instability for periodic boundary conditions in time, in the spectral domain, at z = 15 cm. The central zero frequency component has been cropped for clarity. The growing noise stays largely confined to the area bounded by the noise seed cutoff.

6.3 Full 3D Model

To simulate a finite duration pulse, we must prepare the field with a temporal pulse profile that resolves the edges of the pulse. We remove the explicit periodic boundary conditions in time, by only using one iteration to compute the plasma density. In many of the runs, the initial temporal profile is chosen as a supergaussian, defined as follows:

$$\mathcal{E}(t) \propto \exp\left(-\left[\frac{(t - t_0)^2}{t_p^2}\right]^M\right), \qquad (6.3.1)$$

where M is the supergaussian order. This allows examination of a pulse that contains both transient effects at the edges and a central flat region. Such "flat-top" temporal profiles have been used in experiments [59] and numerical simulations [33]

to study both the edges and the center of a pulse. However, UV pulses of hundreds of picoseconds in length, such as those we consider, have not yet been produced. We can initialize the spatial profile to match the exact computed stationary solution, for diagnostics, or to a Gaussian beam profile, to represent what might be experimentally generated. We can also set the temporal profile to a Gaussian, by setting the supergaussian order M to unity.

As a first example, consider the evolution of the pulse shown in Figures 6.5–6.6. The figures show an XT cross section of the full 3D XYT field. It was initialized with the exact steady state spatial solution, as constructed in Section 3.4, with peak intensity 3.2×10^{16} W/m^2. The temporal supergaussian was of order $M = 10$, with $t_p = 200$ ps, giving a pulse of roughly 400 ps in length. As the pulse propagates, it develops a series of collapse events on the leading edge. These collapses are seeded by the transient shape of the edge, which does not match a steady solution. During each collapse, the intense plasma causes the field to dip in amplitude and temporarily form a ring, which then seeds the next collapse. The trailing edge independently breaks apart into a ring, but does not cause any collapse events. These self-focusing collapse events appear to consume the pulse at a roughly linear rate; for the power in the example, this rate is roughly 200 ps/m.

If we initialize the spatial profile of the pulse to a Gaussian profile, which makes it differ from the exact spatial solution, the beam sheds a small ring in the central region, as observed in the 2D results. The overall structure of the collapses, however, is not significantly different from the previous case. Figure 6.7 shows an intermediate step in such a propagation, and the ring is visible as a bump along the side of the
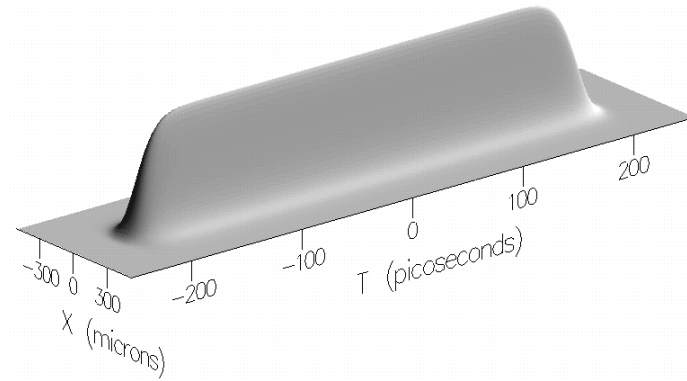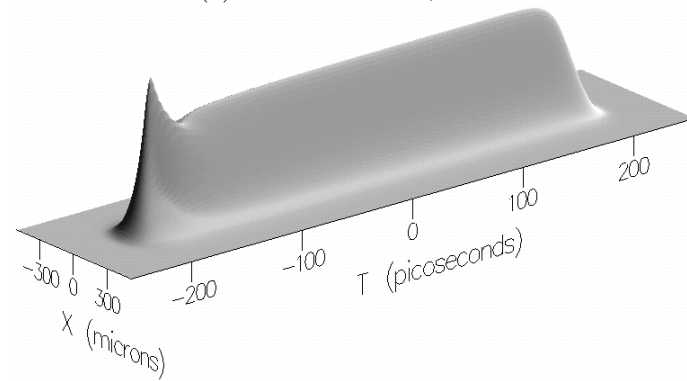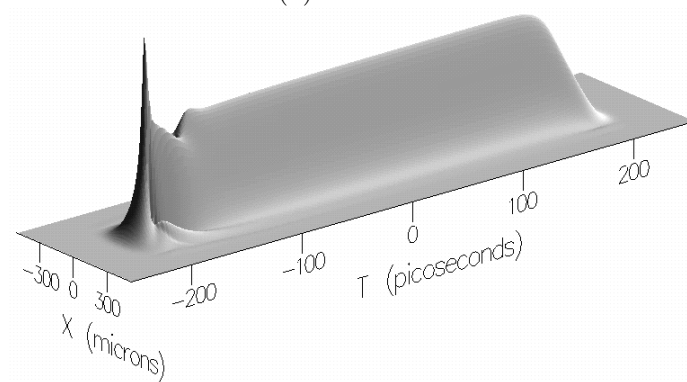
(a) Initial condition, z = 0

(b) z = 5 cm

(c) z = 10 cm

Figure 6.5: Propagation of a finite duration pulse with no noise seed. Note the beginning of the collapse of the leading edge of the pulse.
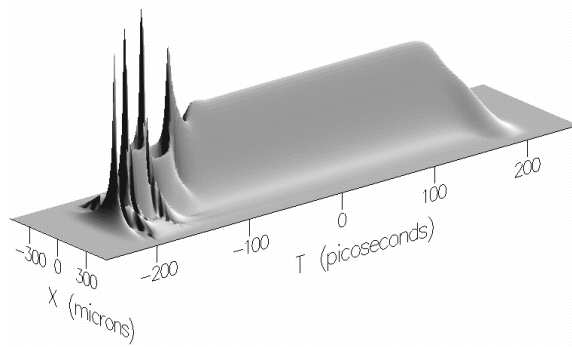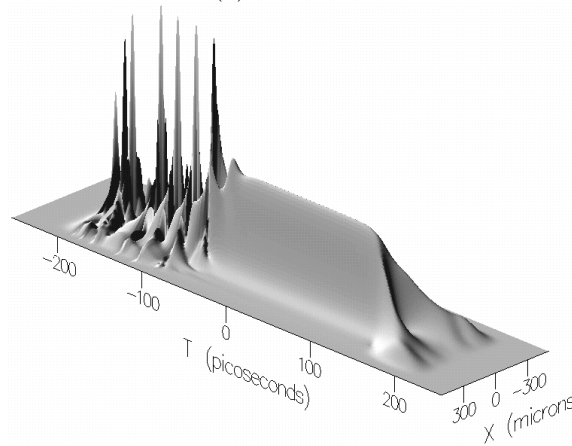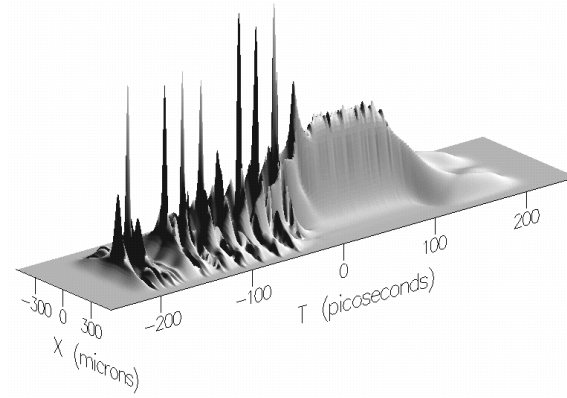
(a) z = 25 cm

(b) z = 50 cm (rotated to show trailing edge)

(c) z = 75 cm

Figure 6.6: Propagation of a finite duration pulse, continued. Note the series of collapse events that consumes the pulse.

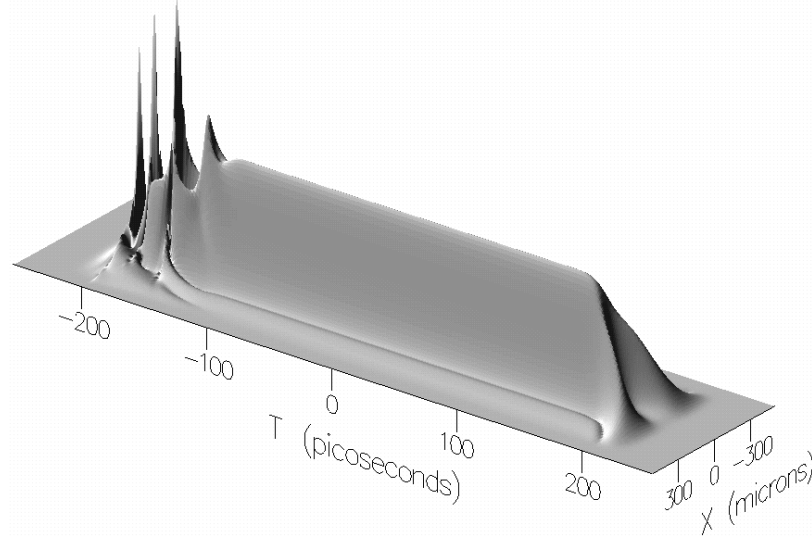pulse. The initial condition was a spatial Gaussian with width 120 μm.

Figure 6.7: Propagation of a spatially Gaussian pulse, at $z = 25$ cm. Note the small ring that is generated, as the field sheds power to move toward an equilibrium solution of the 2D propagation equation.

This consumption of the pulse by collapse, while it arises from the transient be-havior at the beginning of the pulse, does not appear to be itself a transient effect. That is, it does not decay—it maintains a steady rate of consumption of the pulse.

It is unclear exactly what shape the collapsed peaks take. They tend to collapse to dimensions comparable to the grid spacing in time. With no loss, there are only numerical dispersion effects induced by the finite spectral bandwidth of the grid that act to limit the collapse [34]. The simulation has been done with multiple values of Δt to check the convergence, and in all cases the overall result is consistent with respect to the spacing of the pulses and the consumption rate. An example of this comparison is shown for the on-axis amplitude at $z = 25$ cm in Figure 6.8. Losses or other physical

effects such as GVD will stop the temporal collapse; however, numerically resolving these effects requires shorter (femtosecond) time grid intervals, making it impractical to model a long pulse. Our result is not the precise shape of the collapse events, but their presence, which confirms the unstable nature of the leading edge of a pulse.
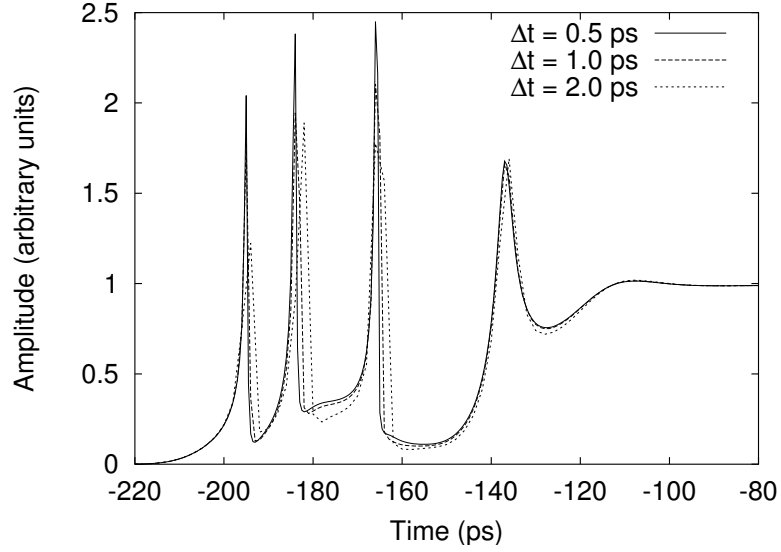

Figure 6.8: Comparison of collapse events for multiple values of Δt. The plot shows the on-axis amplitude of the field at $z = 25$ cm during the initial portion of the pulse, for three different values of Δt.

At the farthest propagation distance shown, in Figure 6.6(c), there is noise growing on the trailing edge of the pulse. This is evidence of the growth of the modulational instability predicted in Chapter 4 and observed in Section 6.2. The instability has grown from numerical noise to a magnitude large enough to be visible in the figure. In the next section, we further examine the instability by seeding the initial pulse with controlled noise.

6.4   Full 3D Pulses with Noise Seed

Figure 6.9 shows the propagation of a pulse with the same initial characteristics of that in the previous section, but now with a noise seed added to the initial condition. The initial condition is not shown, since the initial noise amplitude is small enough that one cannot see it initially. The initial noise amplitude was 0.01 percent, limited to $|\Omega| < 10^{12}$ s^{-1}. The edge-induced collapse events proceed identically at first, but after a few centimeters the noise growth appears, and around $z = 35$ cm, it overwhelms the pulse. The noise growth destroys the pulse in a global fashion, as opposed to the collapse events, which consume the pulse from start to finish.

One might ask if the impact of the modulational instability depends on the temporal shape of the pulse. Does it require a flat, steady-state region? To answer this, Figure 6.10 shows one step in the propagation a pulse with Gaussian initial temporal profile. Here the width was $t_p = 160$ ps, and the initial noise amplitude 0.04 percent. The spatial profile was initialized to a Gaussian with peak power 500 MW and width 120 μm. This example demonstrates that the Gaussian pulse still suffers from front-edge collapse, as well as the growth of the modulational instability. The particular shape of the input pulse does not appear to have a significant effect on the collapse or instability.
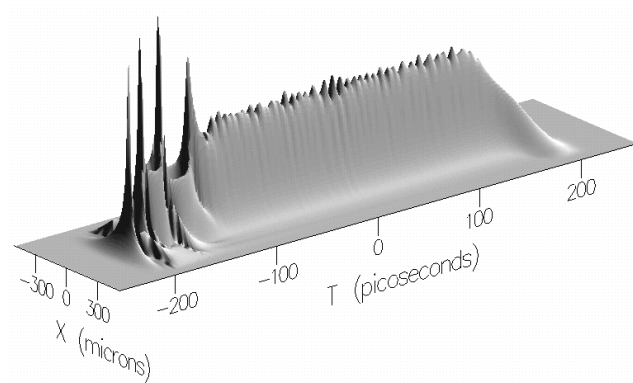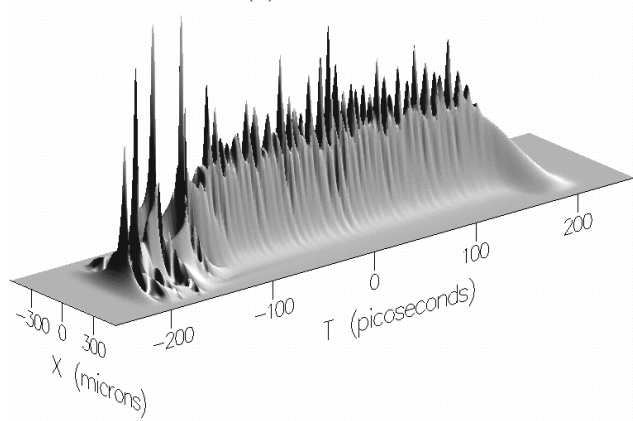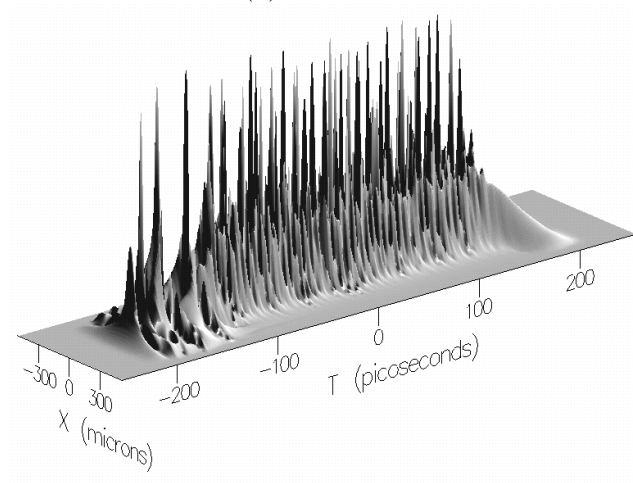
(a) z = 25 cm

(b) z = 30 cm

(c) z = 35 cm

Figure 6.9: Propagation of a finite duration pulse with a noise seed. The beginning of the collapse of the leading edge of the pulse is overwhelmed by the exponential growth of the noise.
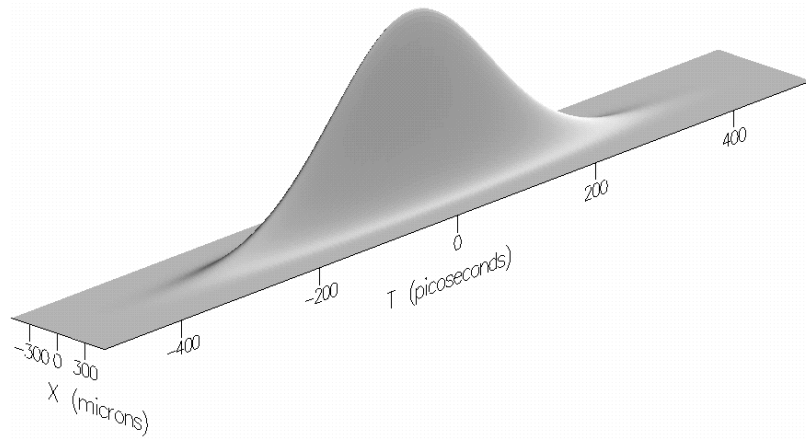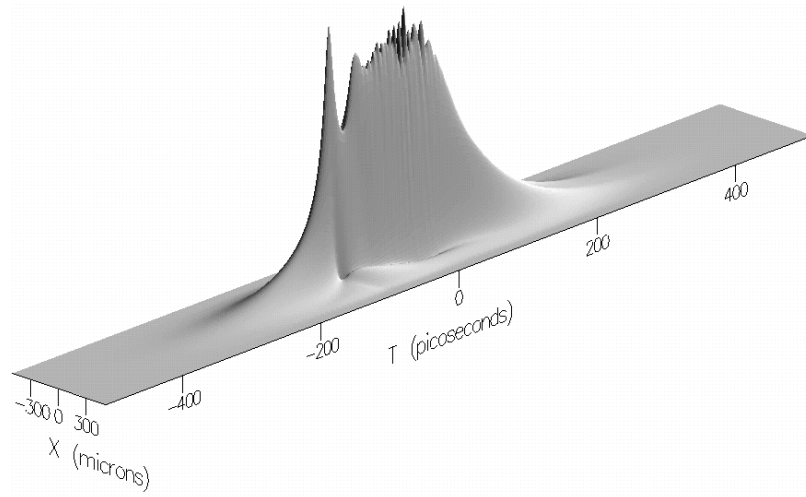
(a) z = 0 cm

(b) z = 25 cm

Figure 6.10: Propagation of a temporally Gaussian pulse. The collapse events and noise growth take place in the same fashion as for a flat-top pulse.

6.5   Complete Pulse with Noise and Loss

The previous sections considered the propagation of pulses under simplified conditions, to isolate the different effects. Let us now prepare a pulse with Gaussian initial spatial shape, a noise seed included, and absorption losses included in the model. We will retain the flat-top supergaussian shape in time. These conditions are intended to be a better representation of what one might be able to generate in the laboratory.

The initial condition was a spatial Gaussian defined with peak power exactly 500 MW, with width 120 μm, and a temporal supergaussian of order 10 and width $t_p = 200$ ps. This corresponds to roughly a 400 ps pulse. The noise seed was 0.01 percent, bandwidth limited to $|\Omega| < 10^{12}$ s^{-1}. Figures 6.11–6.12 show the propagation of the pulse. Additionally, Figure 6.13 shows the induced plasma density at certain propagation distances. The characteristic decay time of the plasma can be seen on the trailing edge. The plasma density does not need to decay to zero at the time grid boundary, because it is an input to the nonlinear response, and is multiplied by the field, which is zero at the boundary.

In all the simulations presented in this dissertation, we use the same base steady state solution with power of 470 MW, or a Gaussian beam cross section with power 500 MW, both of which give a peak intensity of 3.2×10^{16} W/m^2. As discussed earlier, these powers were chosen so that this peak intensity is greater than the plane wave cutoff for stability in the $\Omega = 0$ analysis in Section 4.2. The specific power, however, is arbitrary. The instability and pulse consumption shown here are examples of the effects which occur for any power level that supports a self-trapped beam.
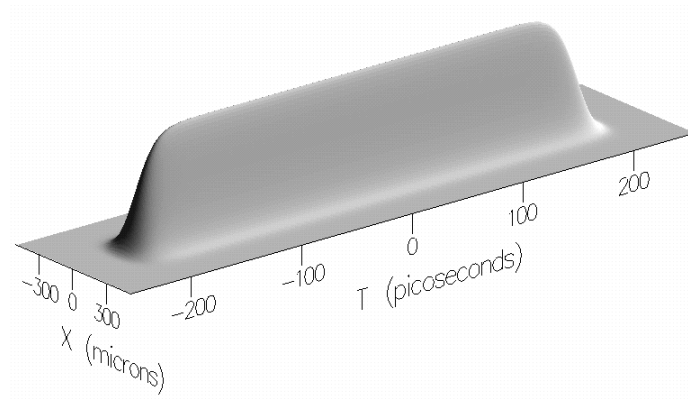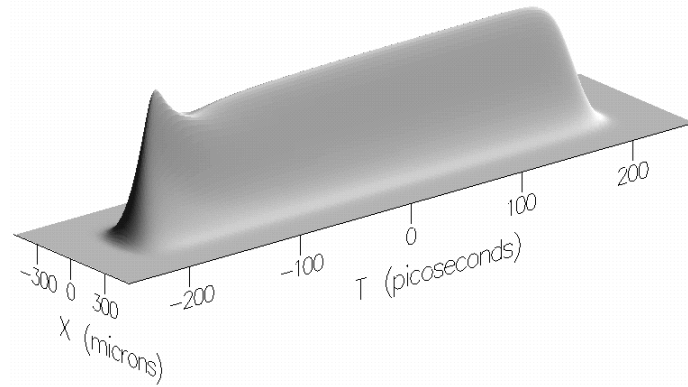
(a) Initial condition, z = 0

(b) z = 5 cm

(c) z = 10 cm

Figure 6.11: Propagation of a finite duration pulse with noise seed and absorption.
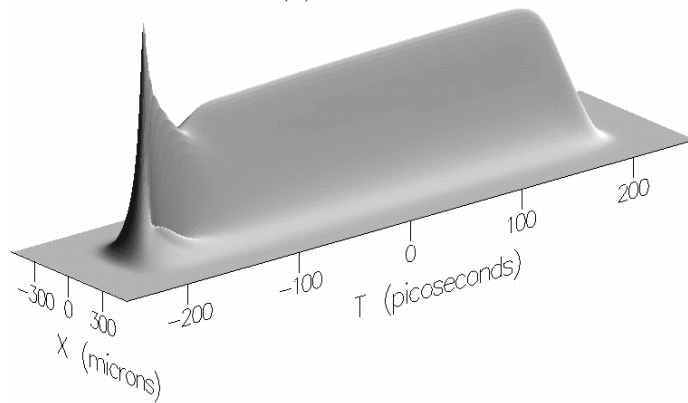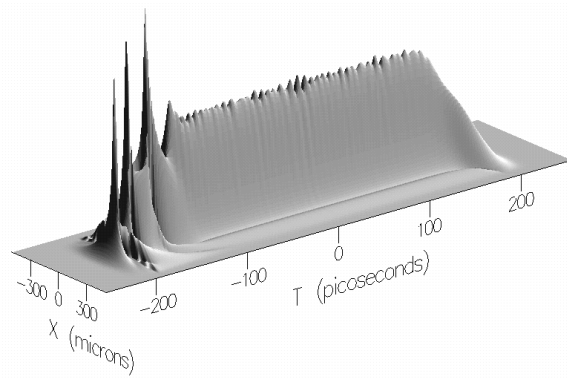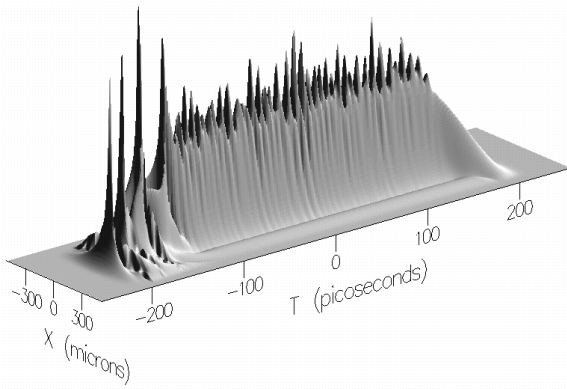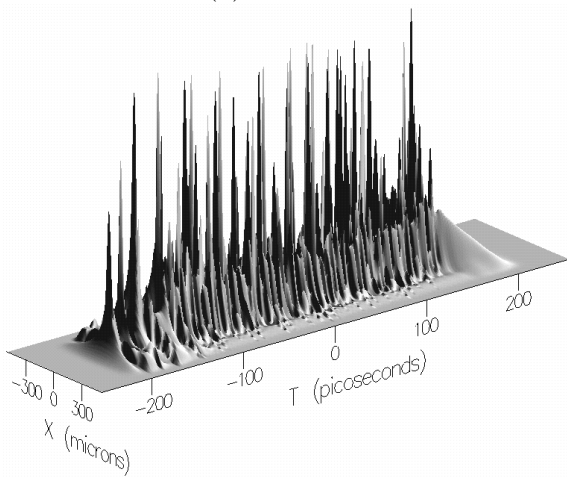
(a) z = 25 cm

(b) z = 30 cm

(c) z = 40 cm

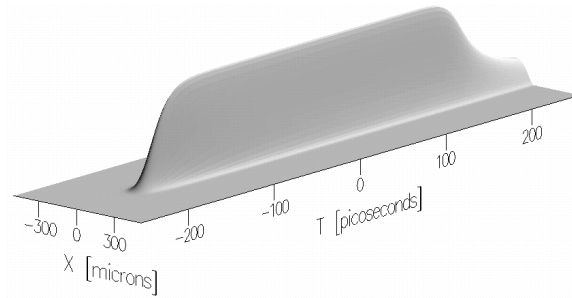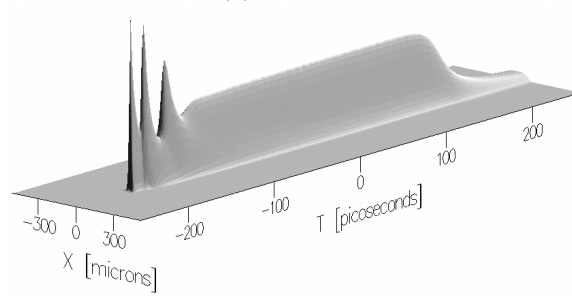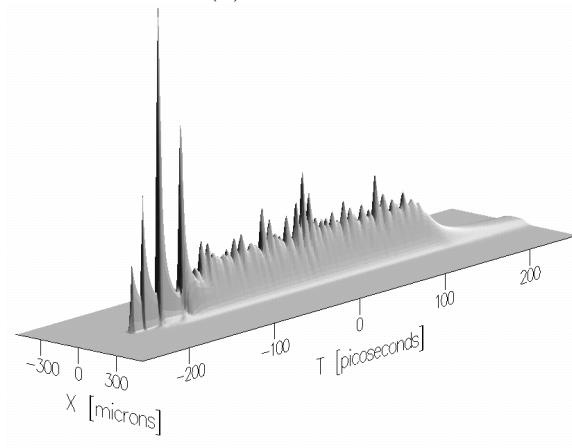Figure 6.12: Propagation of a finite duration pulse with noise seed and absorption, continued.

(a) z = 0 cm

(b) z = 20 cm

(c) z = 30 cm

Figure 6.13: Generated plasma density for the realistic pulse. Plot scales are different due to creation of sharp peaks.

6.6   Fluence

In experiments it is difficult to resolve the temporal profile of a fast, high intensity pulse. Instead, often the fluence is estimated, for example by measuring the profile of a laser burn spot [4] or with a CCD camera [19]. For a given propagation distance z, the fluence is:

$$F(x, y, z) = \int_{-\infty}^{\infty} |\mathcal{E}(x, y, z, t)|^2 \, dt \,, \qquad (6.6.1)$$

where $|\mathcal{E}|^2$ is in units of intensity. The units of fluence are J/m^2, and it corresponds to the energy density delivered by the pulse. By calculating the fluence for a simulated pulse, we can obtain a quantity than can be experimentally observed. We can also compute the width of the fluence profile, using the second moment method, and use it as a measure of how confined the beam remains as it propagates. To determine the combined effect of the linear consumption and the exponential growth of the instability, we examine the plots of the fluence, and the width of the fluence.

Figure 6.14 shows the fluence profiles corresponding to the propagation in the previous section of the 470 MW peak power pulse propagated with noise and loss. The impact of the pulse collapse on the fluence depends on the fraction of the pulse's temporal width that has collapsed. For this example, at roughly 30 cm, the noise has begun to dominate, which begins to significantly affect the fluence profile. Up to that point, the fluence profile is not significantly affected by the collapsing front edge.

Figure 6.15 shows the width of the fluence profile as a function of propagation
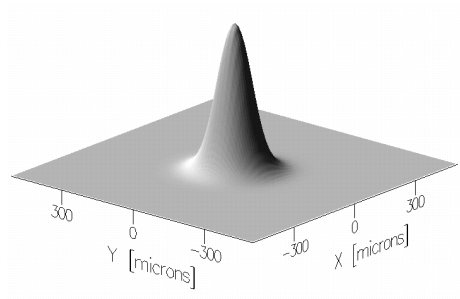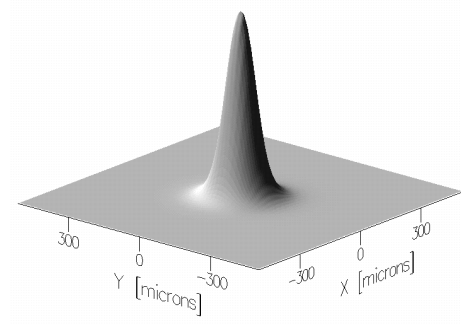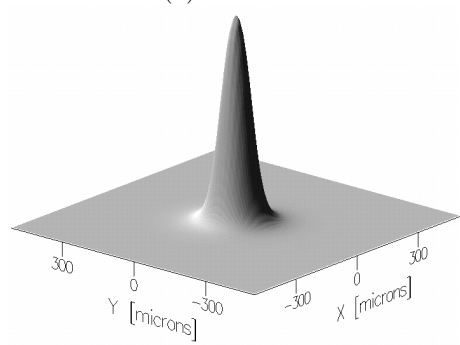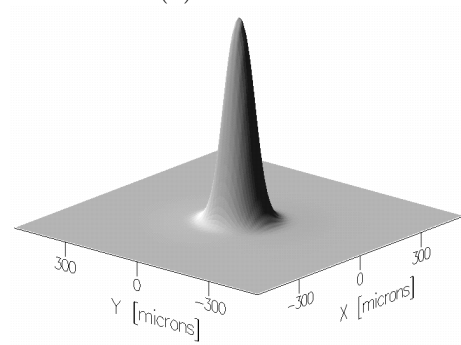
(a) z = 5 cm

(b) z = 10 cm

(c) z = 15 cm

(d) z = 20 cm
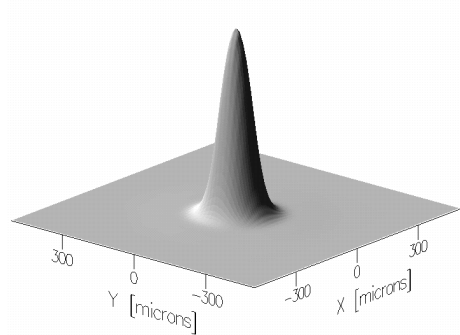
(e) z = 25 cm
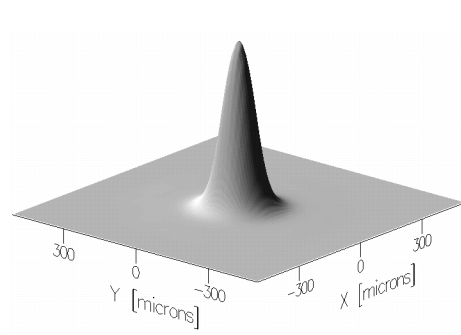
(f) z = 30 cm
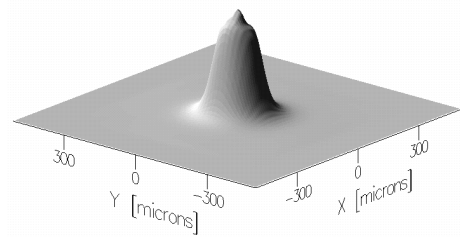
(g) z = 35 cm
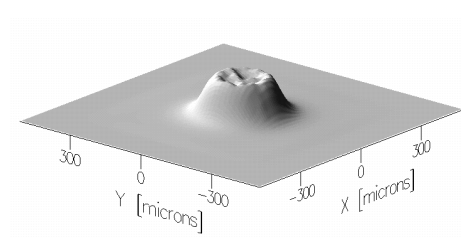
(h) z = 40 cm

Figure 6.14:   Fluence profiles for the realistic pulse, at several propagation distances.

distance for the same case. The fluence width initially decreases, since the initial condition was chosen to have a spatial width larger than the corresponding stationary solution. This is in agreement with the oscillations predicted by the Schwarz-Diels model in Chapter 3. Then the pulse stays confined as the width is maintained, until about 30 cm. During this phase, the leading edge of the pulse is consumed by transient collapse. The effect that this has on the width of the total fluence is dependent on the length of the pulse; for a longer initial pulse, a given consumption rate in ps/m affects a smaller fraction of the pulse, and has less of an impact on the fluence profile. However, once the exponentially growing instability becomes significant, in this case around 30 cm, it quickly spreads the beam width. The noise is seeded uniformly along the pulse, and thus acts as a global effect, and its exponential growth quickly dominates. After 60 cm, the fluence width stops increasing because it is numerically confined by the absorbing boundary conditions.

If one is only interested in the fluence at the target, the claim could be made that the pulse propagates successfully up to the point where the noise growth dominates. This point is determined by the initial amplitude of the noise and the growth rate of the noise, which is is roughly 10-20 cm^{-1}, corresponding to a growth length of 5-10 cm. For this example, the fluence width stays confined until about 40 cm, somewhat more than the Rayleigh range on the order of 10 cm. A pulse could be prepared to propagate farther in a confined fashion if the intensities were lower and the initial noise was controlled, but not for distances on the order of kilometers, as was desired.
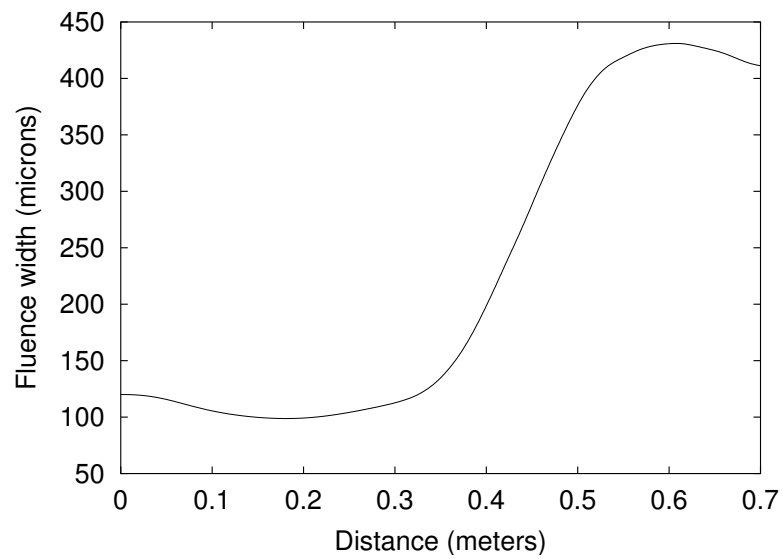
Figure 6.15: Width of fluence profile for the realistic pulse. The initial decrease in width is characteristic of the oscillations predicted by the Schwarz-Diels model. This pulse travels roughly four Rayleigh ranges before being destroyed by the modulational instability.

CHAPTER 7

IMPLICATIONS FOR UV PROPAGATION

7.1 Length Scales

To best understand the impact of the various effects, it will help to consider the dominant length scales, and determine which are the most significant. The fundamental length scale for a Gaussian beam is the Rayleigh range, defined as $\pi w_0^2/\lambda$, where w_0 is the beam waist radius. 'Long distance propagation' is relative to this scale; if a beam does not diffract over many Rayleigh ranges, then it can be considered to have propagated a long distance. For most of the example beams that we have considered, the waist size w_0 is on the order of 100 μm. Combined with working in the ultraviolet at 248 nm, this gives a Rayleigh range on the order of 10 cm.

The length scale for linear (Rayleigh scattering) loss is given by

$$\frac{1}{\alpha_l} = \frac{1}{5 \times 10^{-4}} \text{ m} = 2 \text{ km} \tag{7.1.1}$$

in the ultraviolet at 248 nm [26]. This length is the power $1/e$ length for linear loss. There are also length scales for nonlinear absorption, which depend on the field intensity. This can be seen from the results of propagating the 2D beams in Section 3.3, where the power in the beam drops roughly exponentially down to below 200 MW, but the loss rate then slows, because the absorption is nonlinear. This scale therefore depends on the power in the beam. Given the power loss shown in

Figure 3.5(b), a rough estimate for the nonlinear absorption $1/e$ length for power is 20 meters.

We have both predicted and observed the length scale for instability growth. The growth rate λ is an exponential growth rate, and so $1/\lambda$ gives a length scale for e^1 growth. Typical values for this growth rate are between 10 and 20 m^{-1}, making the growth length scale roughly 5-10 cm. These growth rates become smaller as beam power decreases.

The transient collapse of the beam observed in Section 6.3 takes place on a roughly linear scale. For the power in the example, this consumption rate was 200 ps/m. This means that, neglecting instabilities, for a pulse on the order of 1 ns, the propagation distance before complete consumption and collapse is roughly 5 m. Section 6.6 examined the impact these effects had on the fluence profiles.

Table 7.1 summarizes some of the pertinent length scales for ultraviolet propagation. Note that, not counting the large uncertainty in the Raman growth, the instability growth occurs over the shortest distances. The instability growth scale is comparable to the Rayleigh range. The absorption, both linear and nonlinear, is not strong enough to counter this instability before it fragments the pulse.

7.2 Experimental Implications

Given the numerical results from Chapter 6, we expect that this instability and transient consumption of the pulse will have a significant effect on the propagation of ultraviolet filaments.

Table 7.1: Typical length scales for 470 MW peak power UV filaments

Name	Value	Units
Rayleigh range	10	cm
Linear loss length	2000	m
Nonlinear absorption length	≈ 20	m
Instability growth length	$\approx 5-10$	cm
Pulse consumption distance	$t_p/(200 \text{ ps/m})$	m
Raman scattering	0.01-10	m
Upper limit (Avalanche ionization)	$\approx$ 4-60	ns
Lower limit (Plasma rise time)	$\approx$ 30-200	ps

For our example case, a UV filament of length on the order of a nanosecond may propagate for distances on the order of a meter before it is consumed by collapse events. As discussed in the previous section, this still may be described as long distance propagation, as it is many Rayleigh ranges, given the spatial width of the filament. However, the results do not support hopes that kilometer scale atmospheric propagation of a stable pulse in the ultraviolet will be feasible; the proposal that simple UV pulse results can scale to longer durations is not supported. For the purposes of energy delivery, one may not be concerned with fragmentation of the pulse in the time direction, as long as the fluence profile is confined; these results do not rule out the propagation of some complicated dynamic mode over longer distances. However, as we have seen in Section 6.6, the modulational instability also affects the fluence profile by spreading it. The rate at which the modulational instability fragments the main body of the pulse is faster than the transient consumption. The point at which this fragmentation occurs depends on how much noise is initially present, but due to the exponential growth rate, it cannot be realistically suppressed

for long distances.

As mentioned in the Introduction, experimental generation of ultraviolet pulses of sufficient length to compare with these results has not yet taken place. However, if such pulses were to be generated in laboratory conditions and measured, we would expect to be able to compare the qualitative behavior of the width of the observed fluence profile with our predictions.

7.3   Theoretical Implications

A steady state or long pulse model may simplify theoretical predictions, but if the physics of the problem admit the effects of modulational instability combined with other transient effects, it is dangerous to apply such a model. The presence of such modulational instabilities or transient effects, which we have demonstrated for the case of UV filament propagation, violate the basic steady state beam assumption that is used in the long pulse model.

We have shown that UV filaments should suffer from these effects, limiting their effective propagation range to meters. This will prevent the steady state theory from scaling to longer UV pulses as desired [17, 16]. One might ask if there are other regimes for which we may be able to reduce the impact of these problems. However, an initial advantage of choosing the UV was that the effect of avalanche ionization was greatly reduced, and thus could be ignored, up to certain pulse lengths. Moving to longer wavelengths drastically shortens this upper limit [17].

Section 2.3 mentioned that there are many applications of variational methods to

nonlinear optical propagation problems. The method of Schwarz and Diels [17], when modified, was found to give the same results as the variational method of Anderson and Bonnedal [28]. The drawback of a variational method is that it mathematically confines the solution to fit the variational ansatz. If this ansatz does not capture a mode of a physical instability that is present, the variational method will not be able to model the instability. In the case of UV filaments, the current method is unfortunately an oversimplification of the dynamics of long pulse propagation.

In general, caution must be used when describing soliton solutions of reduced 2D time-independent versions of full 3D equations. For example, the treatment by Skarka et al. of vortex solitons [30] relies on considering the evolution of a single time slice of a pulse, which simplifies the propagation to a time-independent form [15]. This allows the use of a variational technique to describe the spatial form of the vortices. They emphasize the spatial stability of the vortex solutions, but do not consider the full temporal dynamics or stability of the pulse. This time-independent method limits the applicability of the claim that such solitons will be able to propagate for appreciable distances in air, until a full temporal analysis is performed.

Similarly, the time-integrated approach of Bergé et al. to multiple filamentation [31] cannot describe effects such as dynamic replenishment [5, 40] and the collapses in both space and time. The complicated dynamic nature of the problem may mean that "long-range" filaments qualitatively describe the results, but the most convincing theory must account for the time dependent characteristics.

7.4 Raman Scattering

The application of a long pulse model to realistic ultraviolet filaments raises the question of the impact of Raman scattering. The Raman effect is observed when a material scatters light to frequencies different from that of the source, through virtual energy level transitions [1]. The new lower shifted frequencies are labeled Stokes lines, while the higher shifted frequency components are anti-Stokes lines. Spontaneous Raman scattering is usually weak, but stimulated Raman scattering, which can occur for intense laser beams, can convert a large fraction of the incident energy to the Stokes frequency, in a conical emission pattern [1]. In air, the dominant process is stimulated rotational Raman scattering (SRRS) in nitrogen [33, 59], for which the particular rotational transition gives a shift of roughly 1.4×10^{13} s^{-1} [33].

The total nonlinear index n_2 in the Kerr effect for a CW beam includes contributions from bound electrons as well as vibrational and rotational terms. Each of these contributions is due to the response of a material mode (electronic, vibrational, or rotational) to a driving electric field. This response is proportional to the field intensity. For long pulses, the time scale of the material responses is fast, so their time dependence averages out, and the total contribution can be included in a single effective instantaneous value for n_2. For shorter pulses, the time scale may be comparable to the rotational response, so the time dependence, or memory, of this portion of n_2 must be considered.

To include SRRS in a propagation model, the n_2 term is split into time dependent

and time independent parts [16, 40, 2]:

$$ik_0 n_2 |\mathcal{E}|^2 \mathcal{E} \;\rightarrow\; ik_0(1-f)n_2|\mathcal{E}|^2\mathcal{E} + ik_0 f n_2 \left[\int_{-\infty}^{\infty} dt' R(t-t') |\mathcal{E}(t')|^2 \right] \mathcal{E}. \qquad (7.4.1)$$

Here f is the fraction of the nonlinear response that comes from the time-dependent component, in this case SRRS. The function $R(t)$ is the impulse response of the rotational mode.

This impulse response is often modeled as a sinusoidal oscillation multiplied by a decaying exponential [16, 33, 40]. The decay models the dephasing due to the fact that the true response is due to multiple states in a rotational manifold, each with a slightly different frequency. However, this simplified model does not take into account the recurrences which occur over longer time periods, on the picosecond scale [60]. For femtosecond pulses, these recurrences might be neglected, by using the simple exponential decay. However, for picosecond-nanosecond scale pulses, they may need to be included.

Peñano et al. modeled SRRS in air for long laser pulses. Their model considers propagation of pulses under the instantaneous (Kerr) term and the delayed (Raman) term. They performed a linear stability analysis to find the growth rates for Stokes and anti-Stokes fields. Their result is that the Raman gain coefficient for a CW pump is [33]

$$g_0 = \frac{n_R \Omega_0 \omega_0}{2\Gamma_2 c}. \qquad (7.4.2)$$

Here n_R is equivalent to fn_2, the rotational contribution to the total value of n_2 in the CW limit. $\Omega_0 = \omega_R^2 + \Gamma_2^2$, where ω_R is the Raman transition frequency; ω_0 is

the pump optical frequency. Γ_2 is the damping rate of the exponential in the model described above, and is labeled the dipole dephasing rate in Peñano et al. [33]

The experimental value of this gain coefficient, for long pulses at 1 μm wavelength, is 2.5 cm/TW [59]. This value is multiplied by the intensity to obtain a growth rate. From the dependence on ω_0, we expect roughly a factor of four increase when working in the UV, or 10 cm/TW. Given the intensities in this dissertation, on the order of 10^{16} W/m^2, this predicts a growth rate on the order of 10 cm^{-1}. This corresponds to e^{1000} growth over one meter, which contradicts experimental results [4]. For the current picosecond scale UV pulse experiments, the Raman contribution to n_2 was not found to be significant; there was little growth, due to the lack of significant spectral broadening before the pulses ionized [16, 4].

This basic result is modified by the coupling between Stokes and anti-Stokes waves which occurs for small values of the phase mismatch between the two waves. For perfect phase matching, there is zero growth; for small values of the mismatch, the growth rate is reduced [33]. The phase mismatch depends on the propagation angle, or equivalently the value of $k_\perp$. For $k_\perp = 0$, Peñano et al. find the peak growth rate to be roughly one-third of the full g_0 value; it decreases to zero for a particular angle, and then rises to approach g_0 for large angles. Thus in general, for a beam constructed of a continuum of propagation angles, their analysis predicts unstable growth on the order of g_0.

The central question is whether or not the simplified model of the Raman impulse response is useful when considering long pulses. The recurrences may be too important to ignore; they affect any characterization of the response by a time scale. The

fast oscillations in the SRRS for N_2 take place at $\omega_R \approx 1.4 \times 10^{13}$ s^{-1}. This implies that temporal grid resolution roughly ten times finer than we have used may be adequate to numerically model the Raman scattering. However, we need to understand how to treat the Raman response before performing this calculation.

CHAPTER 8

CONCLUSION

8.1 Summary

We have considered the propagation of long filaments in air, primarily in the ultraviolet. It had been speculated that previous successful demonstrations of ultraviolet filaments would scale to longer pulse durations [17, 16], allowing the propagation of long filaments and delivery of higher energies over long distances through the atmosphere. However, the existing theoretical model for long ultraviolet filaments did not address their stability, or how they are created [17].

To address these issues, we have considered and extended a long pulse model for ultraviolet filaments [17]. We have numerically shown that while it is mathematically valid for the domain of pulse lengths that it claims, the pulse instability and transient effects cannot be neglected. We investigated the question of stability using three levels of approximation: the plane wave stability results, the evolution of the linearized coupled perturbation fields, and the simulation of full 3D pulses using a time-dependent plasma model. The results were consistent on all three levels, and showed that the modulational instability ultimately results in the fragmentation of the pulse. We also demonstrated that the transient shape of the front edge of the pulse induces a series of collapse events, which also tend to consume a long pulse. Since the long pulse model can no longer be used for a pulse that is fragmented in time, a new model will be needed.

In the case of ultraviolet filaments, we still predict that propagation over several Rayleigh ranges can be achieved, depending on conditions. The transient collapse consumes on the order of hundreds of picoseconds of the pulse per meter of propagation, but keeps the fluence profile relatively confined. The modulational instability, however, destroys the entire pulse as it grows, with a gain length on the order of tens of centimeters, depending on how it is seeded. The values of these consumption rates depend on the model parameters in Table 3.1, which are not accurately known, but the above detrimental effects will still be present even for alternate values. The the propagation of long stable pulses described by a steady state model over kilometer-scale distances does not appear feasible, given the effects that we have considered.

As discussed in Section 7.3, the long pulse model and other methods that eliminate the time dimension have limited prediction power when temporal stability effects are not considered. A steady state model is not suitable for the description of a highly fragmented pulse. However, there are still open questions as to other effects that may be relevant to the propagation of UV filaments.

8.2   Future Work

The stability results point to unstable growth for all temporal frequencies, independent of the physical parameters such as the wavelength and plasma generation rates. We have applied the results to the UV filament regime, but the specific numerical results are only as accurate as the input parameters. The MPI rate needs significantly more study before a more certain value can be obtained; this value affects

the effective n_3 as well as the time scales of the upper and lower limits in the original model [17]. The wavelength dependence also invites more detailed study; one would like to know how if there is a laser wavelength for which the pulse consumption rate, as well as the growth rates of modulational and Raman instability, can be reduced, but a long pulse model still applied.

More sophisticated models of the plasma may be incorporated, including such effects as plasma diffusion, or variable MPI rates depending on intensity, or pulse length. More study on the impact of stimulated Raman scattering for long pulses is needed, including how to describe the Raman response for long times. When this is understood, the Raman effect could be added to the numerical model, given an order of magnitude increase in computation time or power to accommodate a finer temporal grid.

If one wishes to work with long pulses that will fragment as described, is there a way to model the collapse events with an approximate theory or suitable variational method? The specific structure of the instability modes may also be investigated. Is there some way to prepare a pulse so that the transient collapse effects at the pulse front are avoided? Alternatively, is there an acceptable level of fragmentation of pulses? Could a collection of multiple filaments, interacting in space and time, propagate by replenishing the pulse in time after breakup, as has been seen for spatial filaments [41]?

Study could be done on the impact of temporal instabilities to other cases; for example, optical vortex solitons [30]. One may examine directed energy beam applications, which may not use such small waists and such high intensity fields, following

the example of the case of Raman instability [33]. For such atmospheric applications, the seeding of modulational instability from scattering or turbulence may be important. Finally, a comparison with experiment is needed for the 3D stability results; long UV pulses in the hundreds of picoseconds need to be generated in the laboratory. Then a comparison between prediction and experiment can be made for the fluence profiles, and propagation distances.

APPENDIX A

COMMENT ON UNITS

The problem of multiple systems of units must be addressed. In this dissertation, we use MKS units; a thorough discussion of how quantities in nonlinear optics relate in MKS and CGS (Gaussian) units can be found in Boyd [1, 34]. The convention for the nonlinear index terms can be bewildering; Marburger [34] lists twelve different conventions for the index change term $n_2|\mathcal{E}|^2$. To avoid unnecessary confusion, this Appendix provides some additional clarifications to the units used in this dissertation and how they relate to those used in the paper by Schwarz and Diels [17]. We use many of the parameters from their paper in our numerical simulations.

In section IV.B of Schwarz and Diels [17], the authors convert the evolution equation for the beam width from using amplitude units to intensity and then power units, to write the results conveniently in terms of the critical power. To do this, they convert $\chi^{(4)}$ to $\bar{n}_3$ and finally the plasma absorption coefficient β_4. The equations they obtain are correct, but there is an error in the assertion below equation (10) in their paper, which states that $n_{m-1} = \epsilon_0 c n_0 \bar{n}_{m-1}/2$ is the relationship between the amplitude and intensity refractive indices. The correct relation can be derived from the following: The index of refraction of air is expanded in terms of intensity as

$$n = n_0 + \bar{n}_2 I + \bar{n}_3 I^{1.5}. \tag{A.1}$$

Keeping this form in mind, expand the susceptibility in terms of amplitude:

$$n^2 = 1 + \chi \tag{A.2a}$$

$$= 1 + \chi^{(1)} + \chi^{(3)}|\mathcal{E}|^2 + \chi^{(4)}|\mathcal{E}|^3 \tag{A.2b}$$

$$= n_0^2 + \chi^{(3)}|\mathcal{E}|^2 + \chi^{(4)}|\mathcal{E}|^3 \tag{A.2c}$$

$$= n_0^2 \left(1 + \frac{\chi^{(3)}|\mathcal{E}|^2}{n_0^2} + \frac{\chi^{(4)}|\mathcal{E}|^3}{n_0^2} \right). \tag{A.2d}$$

Thus, for small nonlinearities,

$$n \approx n_0 \left(1 + \frac{\chi^{(3)}|\mathcal{E}|^2}{2n_0^2} + \frac{\chi^{(4)}|\mathcal{E}|^3}{2n_0^2} \right) \tag{A.3a}$$

$$= n_0 + \frac{\chi^{(3)}|\mathcal{E}|^2}{2n_0} + \frac{\chi^{(4)}|\mathcal{E}|^3}{2n_0} \tag{A.3b}$$

$$= n_0 + n_2|\mathcal{E}|^2 + n_3|\mathcal{E}|^3. \tag{A.3c}$$

where, by equation (10) of Schwarz and Diels [17], $\chi^{(m)} = 2n_0 n_{(m-1)}$ defines n_{m-1}.

Next use the relationship between intensity and field amplitude:

$$I = \frac{n_0 \epsilon_0 c}{2}|\mathcal{E}|^2 \tag{A.4}$$

to write

$$n \approx n_0 + \frac{2}{\epsilon_0 c n_0} n_2 I + \left(\frac{2}{\epsilon_0 c n_0} \right)^{1.5} n_3 I^{1.5}. \tag{A.5}$$

By comparing this with Equation (A.1), we find

$$n_2 = \frac{\epsilon_0 c n_0}{2} \bar{n}_2, \tag{A.6}$$

$$n_3 = \left(\frac{\epsilon_0 c n_0}{2}\right)^{1.5} \bar{n}_3, \tag{A.7}$$

$$n_m = \left(\frac{\epsilon_0 c n_0}{2}\right)^{m/2} \bar{n}_m. \tag{A.8}$$

This differs from the assertion below Equation (10) in Schwarz and Diels [17] by the addition of the exponent on the prefactor, which depends on the order of the nonlinearity.

To simplify computations, one can use either intensity or field units for the quantities $\mathcal{E}$, $n_2, n_3, \ldots$, and $\chi^{(3)}, \chi^{(4)}, \ldots$, as long as the units are consistent. Intensity units for $\mathcal{E}$ are defined such that $|\mathcal{E}|^2$ is the intensity. Thus $n_2|\mathcal{E}|^2$ represents the same unitless quantity as long as both factors are measured consistently in intensity or field units.

Note that under strict radiometric convention, the quantity with the units W/m^2 is denoted *irradiance*, while *intensity* is reserved for the quantity measured in W/sr. However, many authors in this field use *intensity* for W/m^2, so we will do the same.

Schwarz and Diels [17] use the notation $\bar{n}_2$ for the nonlinear self-focusing index in intensity units, and n_2 for the same quantity in field units. For simplicity, in the body of this dissertation, we use only intensity units, and use $n_2, n_3, \ldots$ to denote the self-focusing index and higher order indices in these units.

Next consider the equation for the nonlinear attenuation of the beam. Equa-

tion (17) in the Schwarz-Diels paper [17] gives this as

$$\frac{dI}{dz} = -3\hbar\omega N_0\sigma^{(3)}I^3 + \frac{1}{l}\bar{n}_3 I^{1.5} - 2I_0\frac{w_0^2}{w(z)^4}\frac{d(w^2)}{dz}. \tag{A.9}$$

Here I is the on-axis intensity, $\hbar\omega$ is the energy per photon, N_0 is the density of oxygen, $\sigma^{(3)}$ is the three-photon absorption cross section, $\bar{n}_3$ is the plasma nonlinear index in intensity units, l is the mean free path length of the electrons in the plasma, I_0 is the initial intensity, and w_0 and w are the initial and evolving beam width.

There are a few corrections that need to made to this equation. In the first term, which describes MPI loss, the units of $\sigma^{(3)}$ are listed incorrectly in Table I of their paper; the correct units are m^6s^2/J^3. These correct units are used in section II.B of the paper.

The second term describes plasma absorption, but the intensity I should be raised to the power 2.5. This makes it agree with equation (16) of the paper, which states that the coefficient for plasma absorption scales as $I^{1.5}$. The units of $\bar{n}_3$ are also listed incorrectly in the table; they are $m^3/W^{3/2}$.

The third term represents the change in intensity due to the change in beam width. It is apparently obtained by differentiating $I(z) = (w_0^2/w^2)I_0$, but there is a factor of two present in the equation in the paper that should not be there. Thus the correct equation should read

$$\frac{dI}{dz} = -3\hbar\omega N_0\sigma^{(3)}I^3 + \frac{1}{l}\bar{n}_3 I^{2.5} - I_0\frac{w_0^2}{w(z)^4}\frac{d(w^2)}{dz}. \tag{A.10}$$

Next, they convert the equation for the on-axis intensity to an equation for the attenuation of the beam power, using the relation that for a Gaussian beam with $I(r, z) = I(z) \exp(-2r^2/w^2)$ the power is $P = \pi w^2 I_0/2$. The result is

$$\frac{1}{P}\frac{dP}{dz} = -\beta_3 \frac{1}{w^4}P^2 - \beta_4 \frac{1}{w^3}P^{3/2}, \tag{A.11}$$

where

$$\beta_3 = \left(\frac{2}{\pi}\right)^2 3\hbar\omega N_0 \sigma^{(3)} = \left(\frac{2}{\pi}\right)^2 \beta_{MPI} \qquad \text{and} \qquad \beta_4 = -\left(\frac{2}{\pi}\right)^{3/2}\frac{\bar{n}_3}{l} \tag{A.12}$$

are respectively called the three-photon power attenuation coefficient and the non-linear plasma absorption coefficient [17]. This result can be derived from Equation (A.10), so the errors in Equation (A.9) do not affect the results in the remainder of their paper, other than requiring some corrections to the units in Table I of their paper. Table A.1 summarizes these corrections to the units.

Table A.1: Corrections to units in Schwarz-Diels paper

Description	Name	Corrected Units
Plasma nonlinear index (intensity)	$\bar{n}_3$	$m^3/W^{3/2}$
Three-photon absorption cross section	$\sigma^{(3)}$	$m^6 s^2/J^3$
Plasma nonlinear absorption (intensity)	β_{MPI}	m^3/W^2
Plasma nonlinear absorption (power)	β_4	$m^2/W^{3/2}$
Three-photon absorption (power)	β_3	m^3/W^2

APPENDIX B

SPLIT-OPERATOR METHOD

B.1   Split-Operator Propagation

For all three grid types that are considered in this dissertation, we use the split-operator method to propagate the fields. In the split-operator propagation scheme, we define the propagator as a combination of a linear diffraction piece $\hat{T}$, and a nonlinear index change piece $\hat{V}$. Let

$$\frac{\partial \mathcal{E}}{\partial z} = i\hat{T}\mathcal{E} + i\hat{V}\mathcal{E}, \tag{B.1}$$

where for the example of single 2D field propagation,

$$\hat{T} = \frac{\nabla_\perp^2}{2k_0} \tag{B.2}$$

$$\hat{V} = k_0 n_2 |\mathcal{E}|^2 + k_0 n_3 |\mathcal{E}|^3 + k_0 n_4 |\mathcal{E}|^4 - \frac{\beta^{(K)}}{2}|\mathcal{E}|^{2K-2} - \frac{\sigma}{2}(1 + i\omega\tau)\rho. \tag{B.3}$$

Note that $\hat{T}$ will be diagonal in the spectral (k) representation, while $\hat{V}$ is diagonal in the spatial (x) representation for $\mathcal{E}$, and $\hat{V}$ acts as a changing potential. The split-operator method represents the incremental step propagator $\exp[i(\hat{T}+\hat{V})\Delta z]$ as

$$\exp\left(i\frac{\hat{T}\Delta z}{2}\right)\exp\left(i\hat{V}\Delta z\right)\exp\left(i\frac{\hat{T}\Delta z}{2}\right) + \mathcal{O}(\Delta z^3). \tag{B.4}$$

For the $\hat{T}$ piece, we use the spectral representation:

$$\exp(i\frac{\hat{T}\Delta z}{2})\mathcal{E}(k_x, k_y) = \exp(i(-k_\perp^2/4k_0)\Delta z)\mathcal{E}(k_x, k_y). \qquad \text{(B.5)}$$

Fourier transform $\mathcal{E}$ to the k representation before multiplying it by the exponential $\exp(-ik_\perp^2\Delta z/4k_0)$. This exponential factor can be precomputed for each point on the k grid, that is, each value of $k_\perp$. Thus the application of the two linear diffraction half-steps is reduced to applying an FFT to get to the spectral representation, multiplying the array by the precomputed linear propagator array, and inverse FFT to return to the spatial representation.

The exponential with $\hat{V}$, the nonlinear response, is applied in the spatial representation:

$$\exp(i\hat{V}\Delta z)\mathcal{E}(x, y) = \exp(iV(|\mathcal{E}|^2)\Delta z)\mathcal{E}(x, y). \qquad \text{(B.6)}$$

First we compute the value of $V(|\mathcal{E}|^2)$, using the value of $\mathcal{E}$ at the previous z step, then compute the exponential factor, and multiply the field in real space by this piece of the propagator. The computation of V can be simple if it only involves n_2 and n_3, or complicated if a more complete model is used where the plasma density ρ is needed.

In the code, the field is initially defined in the spatial representation. An initial FFT step is performed to transform to the spectral representation before entering the main loop. The main loop consists of applying half the linear propagator, transforming back to x space, applying the nonlinear response, transforming to k space, and applying the second half of the linear propagator. The two halves of the linear

propagation step can be combined in a practical code, but for rigorous accuracy one must keep track of where one is in the propagation and make sure for the final step that the full propagator is completed.

The initial field is defined over a space grid of N_x by N_y points with uniform grid spacing Δx and Δy. The space grid is defined so that the point with space coordinates $(x = 0, y = 0)$ is stored at location $(N_x/2, N_y/2)$ in memory. For optimal FFT speed N_x and N_y are chosen as powers of 2. This spatial grid defines a spectral (k-space) grid where $\Delta k_x = 2\pi/(N_x \Delta x)$ and similarly for Δk_y. The maximum value of k_x is given roughly by $\pi/\Delta x$. Recall that the common convention for FFT storage is to locate the point $(k_x = 0, k_y = 0)$ as the first element in the FFT array, and that the array wraps around near the Nyquist frequency [61].

B.2 Numerical Issues

When using the split-operator spectral method, one must choose the numerical grid sizes wisely. Both the spatial and spectral grids must contain adequate resolution and extent to represent the full field. If the field begins to collapse to scales that are too small spatially, the spectral representation will flow off the spectral grid boundary. The interactive graphical implementation used in our code significantly aids the user in avoiding bad choices of grid parameters.

For split-operator propagation, there are approximate relationships between the propagation step size and the grid sizes to ensure accuracy in the method. This can be seen by considering the linear diffraction piece of the split-operator formula in

Equation (B.4). The individual portions of the split exponential should be small, and thus the arguments of the exponential phase factors should be smaller than unity, if the approximation is to be good. Except in the case of extreme self-focusing, the $\hat{T}$ term is usually larger than the $\hat{V}$ term. For our UV propagation example, take self-focusing only to get an upper limit; the value of $\hat{V}$ on axis is

$$\hat{V} = k_0 n_2 |\mathcal{E}|^2 \approx 60 \text{ m}^{-1}. \tag{B.1}$$

The maximum absolute value of $\hat{T}$ for a given grid is given, in the spectral representation, by

$$|\hat{T}| = \frac{k_{max}^2}{2k_0} = \frac{(\pi/\Delta x)^2}{2k_0}, \tag{B.2}$$

which gives roughly 3000 m^{-1} for 248 nm and $\Delta x = 8$ μm. The maximum argument in the exponential is then

$$\frac{|\hat{T}|\Delta z}{2} = \frac{\pi^2 \Delta z}{4k_0 \Delta x^2}. \tag{B.3}$$

Setting this to be less than unity gives

$$\Delta z \lesssim \frac{4k_0}{\pi^2} \Delta x^2 \tag{B.4}$$

as the condition for Δz. For $\Delta x = 8$ μm (see Table 5.1), we find that $\Delta z \lesssim 0.66$ mm is the condition, which is just satisfied by our choice of $\Delta z = 0.5$ mm. If this condition is not well satisfied, artificial numerical instabilities can arise. However, if in practice the spectral representation of the field does not sample the outer edges of the

spectral grid, one can effectively use a larger propagation step. But when studying stability, noise on the entire grid becomes important. This was observed in the case of propagating the coupled perturbation fields for $\Omega = 0$; if the value for Δz was too large, unstable artificial numerical growth occurred. A more sophisticated study of the split-operator beam propagation method for the case of a fixed potential term $\hat{V}$ was done by Thylén, who also found that the condition on the step size Δz could be relaxed in practice [62].

REFERENCES

[1] Robert W. Boyd. *Nonlinear Optics*. Academic Press, 1992.

[2] J.V. Moloney, M. Kolesik, M. Mlejnek, and E.M. Wright. Femtosecond self-guided atmospheric light strings. *Chaos*, 10:559–569, 2000.

[3] A. Couairon and L. Bergé. Light filaments in air for ultraviolet and infrared wavelengths. *Physical Review Letters*, 88:135003, 2002.

[4] S. Tzortzakis et al. Nonlinear propagation of subpicosecond ultraviolet laser pulses in air. *Optics Letters*, 25:1270–1272, 2000.

[5] M. Mlejnek, M. Kolesik, J.V. Moloney, and E.M. Wright. Optically turbulent femtosecond light guide in air. *Physical Review Letters*, 83:2938–2941, 1999.

[6] François Courvoisier et al. Ultraintense light filaments transmitted through clouds. *Applied Physics Letters*, 83:213–215, 2003.

[7] N. Aközbek, M. Scalora, C.M. Bowden, and S.L. Chin. White-light continuum generation and filamentation during the propagation of ultra-short laser pulses in air. *Optics Communications*, 191:353–362, 2001.

[8] J. Kasparian et al. Infrared extension of the supercontinuum generated by femtosecond terawatt laser pulses propagating in the atmosphere. *Optics Letters*, 25:1397–1399, 2000.

[9] J. Yu et al. Backward supercontinuum emission from a filament generated by ultrashort laser pulses in air. *Optics Letters*, 26:533–535, 2001.

[10] P. Rairoux et al. Remote sensing of the atmosphere using ultrashort laser pulses. *Applied Physics B*, 71:573–580, 2000.

[11] H. Wille et al. Teramobile: A mobile femtosecond-terawatt laser and detection system. *The European Physical Journal: Applied Physics*, 20:183–190, 2002.

[12] Jean-Claude Diels et al. Lightning control with lasers. *Scientific American*, August 1997.

[13] Xin Miao Zhao, Jean-Claude Diels, Cai Yi Wang, and Juan M. Elizondo. Femtosecond ultraviolet laser pulse induced lightning discharges in gases. *IEEE Journal of Quantum Electronics*, 31:599–612, 1995.

[14] Miguel Rodriguez et al. Kilometer-range nonlinear propagation of femtosecond laser pulses. *Physical Review E*, 69:36607, 2004.

REFERENCES - Continued

[15] B. La Fontaine et al. Filamentation of ultrashort pulse laser beams resulting from their propagation over long distances in air. *Physics of Plasmas*, 6:1615–1621, 1999.

[16] Jens Schwarz, Patrick Rambo, Jean-Claude Diels, Miroslav Kolesik, Ewan M. Wright, and Jerry V. Moloney. Ultraviolet filamentation in air. *Optics Communications*, 180:383–390, 2000.

[17] Jens Schwarz and Jean-Claude Diels. Analytical solution for uv filaments. *Physical Review A*, 65:013806, 2001.

[18] Y.R. Shen. Self-focusing: Experimental. *Progress in Quantum Electronics*, 4:1–35, 1975.

[19] S. Tzortzakis et al. Self-guided propagation of ultrashort IR laser pulses in fused silica. *Physical Review Letters*, 87:213902, 2001.

[20] A. Braun, G. Korn, X. Liu, D. Du, J. Squier, and G. Mourou. Self-channeling of high-peak-power femtosecond laser pulses in air. *Optics Letters*, 20:73–75, 1995.

[21] A.J. Campillo, S.L. Shapiro, and B.R. Suydam. Periodic breakup of optical beams due to self-focusing. *Applied Physics Letters*, 23:628–630, 1973.

[22] S. Petit, A. Talebpour, A. Proulx, and S.L. Chin. Polarization dependence of the propagation of intense laser pulses in air. *Optics Communications*, 175:323–327, 2000.

[23] O.G. Kosareva et al. Conical emission from laser-plasma interactions in the filamentation of powerful ultrashort laser pulses in air. *Optics Letters*, 22:1332–1334, 1997.

[24] E.T.J. Nibbering et al. Conical emission from self-guided femtosecond pulses in air. *Optics Letters*, 21:62–64, 1996.

[25] S.L. Chin, N. Aközbek, A. Proulx, S. Petit, and C.M. Bowden. Transverse ring formation of a focused femtosecond laser pulse propagating in air. *Optics Communications*, 188:181–186, 2001.

[26] Jens Schwarz. *High Intensity Laser Pulse Propagation through the Atmosphere, Lightning Protection and Filamentation.* PhD thesis, Friedrich-Schiller-Universität Jena, 2003.

[27] Ewan M. Wright, Brian L. Lawrence, William Torruellas, and George Stegeman. Stable self-trapping and ring formation in polydiacetylene para-toluene sulfonate. *Optics Letters*, 20:2481–2483, 1995.

REFERENCES - Continued

[28] D. Anderson and M. Bonnedal. Variational approach to nonlinear self-focusing of Gaussian laser beams. *Physics of Fluids*, 22:105–109, 1979.

[29] N. Aközbek, C.M. Bowden, A. Talebpour, and S.L. Chin. Femtosecond pulse propagation in air: Variational analysis. *Physical Review E*, 61:4540–4549, 2000.

[30] V. Skarka, N.B. Aleksić, and V.I. Berezhiani. Evolution of singular optical pulses towards vortex solitons and filamentation in air. *Physics Letters A*, 319:317–324, 2003.

[31] L. Bergé et al. Multiple filamentation of terawatt laser pulses in air. *Physical Review Letters*, 92:225002, 2004.

[32] V.P. Kandidov, O.G. Kosareva, and S.A. Shlenov. Spatiotemporal instability of an intense subpicosecond laser pulse in gases. *Quantum Electronics*, 27:441–444, 1997.

[33] J.R. Peñano et al. Stimulated Raman scattering of intense laser pulses in air. *Physical Review E*, 68:056502, 2003.

[34] J.H. Marburger. Self-focusing: Theory. *Progress in Quantum Electronics*, 4:35–110, 1975.

[35] Govind P. Agrawal. *Nonlinear Fiber Optics*. Academic Press, 1995.

[36] M.D. Feit and J.A. Fleck, Jr. Effect of refraction on spot-size dependence of laser-induced breakdown. *Applied Physics Letters*, 24:169–172, 1974.

[37] M. Hercher. Laser-induced damage in transparent media. *Journal of the Optical Society of America*, 54:563, 1964.

[38] R.Y. Chiao, E. Garmire, and C.H. Townes. Self-trapping of optical beams. *Physical Review Letters*, 13:479–482, 1964.

[39] P.L. Kelley. Self-focusing of optical beams. *Physical Review Letters*, 15:1005–1008, 1965.

[40] M. Mlejnek, E.M. Wright, and J.V. Moloney. Dynamic spatial replenishment of femtosecond pulses propagating in air. *Optics Letters*, 23:382–384, 1998.

[41] S. Tzortzakis et al. Breakup and fusion of self-guided femtosecond light pulses in air. *Physical Review Letters*, 86:5470–5474, 2001.

[42] H.R. Lange et al. Anomalous long-range propagation of femtosecond laser pulses through air: moving focus or pulse self-guiding? *Optics Letters*, 23:120–122, 1998.

REFERENCES - Continued

[43] A. Brodeur et al. Moving focus in the propagation of ultrashort laser pulses in air. *Optics Letters*, 22:304–306, 1997.

[44] Luc Bergé. Wave collapse in physics: principles and applications to light and plasma waves. *Physics Reports*, 303:259–370, 1998.

[45] Sabino Chávez Cerda. *Self-Confined Beam Propagation and Pattern Formation in Nonlinear Optics*. PhD thesis, Imperial College of Science, Technology and Medicine, University of London, November 1994.

[46] D. Anderson. Variational approach to nonlinear pulse propagation in optical fibers. *Physical Review A*, 27:3135–3145, 1983.

[47] Sabino Chávez Cerda, S.B. Cavalcanti, and J.M. Hickmann. A variational approach of nonlinear dissipative pulse propagation. *The European Physical Journal D*, 1:313–316, 1998.

[48] J. Schwarz, P. Rambo, and J.C. Diels. Measurements of multiphoton ionization coefficients with ultrashort ultraviolet laser pulses. *Applied Physics B*, 72:343–347, 2001.

[49] Vittorio Magni, Giulio Cerullo, and Sandro De Silvestri. ABCD matrix analysis of propagation of gaussian beams through Kerr media. *Optics Communications*, 96:348–355, 1993.

[50] G. Cerullo, A. Dienes, and V. Magni. Space-time coupling and collapse threshold for femtosecond pulses in dispersive nonlinear media. *Optics Letters*, 21:65–67, 1996.

[51] Gadi Fibich and Alexander L. Gaeta. Critical power for self-focusing in bulk media and in hollow waveguides. *Optics Letters*, 25:335–337, 2000.

[52] K.D. Moll, Alexander L. Gaeta, and Gadi Fibitch. Self-similar optical wave collapse: Observation of the Townes profile. *Physical Review Letters*, 20:203902, 2003.

[53] L.W. Liou et al. Spatiotemporal instabilities in dispersive nonlinear media. *Physical Review A*, 46:4202–4208, 1992.

[54] V.E. Zakharov and A.M. Rubenchik. Instability of waveguides and solitons in nonlinear media. *Sov. Phys.-JETP*, 38:494–500, 1974.

[55] Henry C. Yuen and Warren E. Ferguson, Jr. Relationship between Benjamin-Feir instability and recurrence in the nonlinear Schrödinger equation. *Physics of Fluids*, 21:1275–1278, 1978.

REFERENCES - Continued

[56] Thierry Lehner and Nicole Auby. Stabilization of the Kerr effect by self-induced ionization: Formation of optical light spatially localized structures. *Physical Review E*, 61:1996–2005, 2000.

[57] Zhigang Bian and Thomas M. Antonsen, Jr. Ionization instabilities of an electromagnetic wave propagating in a tenuous gas. *Physics of Plasmas*, 8:3183–3194, 2001.

[58] A.J. Campillo, S.L. Shapiro, and B.R. Suydam. Relationship of self-focusing to spatial instability modes. *Applied Physics Letters*, 24:178–179, 1974.

[59] M.A. Henesian, C.D. Swift, and J.R. Murray. Stimulated rotational Raman scattering in nitrogen in long air paths. *Optics Letters*, 10:565–567, 1985.

[60] Jean-Francois Ripoche et al. Determination of the time dependence of n_2 in air. *Optics Communications*, 135:310–314, 1997.

[61] William H. Press, Brian P. Flannery, Saul A. Teukolsky, and William T. Vetterling. *Numerical Recipes*. Cambridge University Press, 1986.

[62] Lars Thylén. The beam propagation method: an analysis of its applicability. *Optical and Quantum Electronics*, 15:433–439, 1983.